National Library of Canada
Acquisitions and Bibliographic Services Branch
395 Wellington Street
Ottawa, Ontario
K1A 0N4

Bibliothèque nationale du Canada
Direction des acquisitions et des services bibliographiques
395, rue Wellington
Ottawa (Ontario)
K1A 0N4

Your file Votre référence

Our file Notre référence

NOTICE

The quality of this microform is heavily dependent upon the quality of the original thesis submitted for microfilming. Every effort has been made to ensure the highest quality of reproduction possible.

If pages are missing, contact the university which granted the degree.

Some pages may have indistinct print especially if the original pages were typed with a poor typewriter ribbon or if the university sent us an inferior photocopy.

Reproduction in full or in part of this microform is governed by the Canadian Copyright Act, R.S.C. 1970, c. C-30, and subsequent amendments.

AVIS

La qualité de cette microforme dépend grandement de la qualité de la thèse soumise au microfilmage. Nous avons tout fait pour assurer une qualité supérieure de reproduction.

S'il manque des pages, veuillez communiquer avec l'université qui a conféré le grade.

La qualité d'impression de certaines pages peut laisser à désirer, surtout si les pages originales ont été dactylographiées à l'aide d'un ruban usé ou si l'université nous a fait parvenir une photocopie de qualité inférieure.

La reproduction, même partielle, de cette microforme est soumise à la Loi canadienne sur le droit d'auteur, SRC 1970, c. C-30, et ses amendements subséquents.

Canada

UNIVERSITY OF ALBERTA

THREE DIMENSIONAL FINITE ELEMENT STRESS-RELIEF MODEL APPLIED TO STRESS MEASUREMENT BY OPTICAL HOLOGRAPHY

by

Yongyi Li

A THESIS

SUBMITTED TO THE FACULTY OF GRADUATE STUDIES AND RESEARCH IN PARTIAL FULFILMENT OF THE REQUIREMENTS FOR THE DEGREE

OF

MASTER OF SCIENCE

IN

GEOPHYSICS

DEPARTMENT OF PHYSICS

EDMONTON, ALBERTA

FALL, 1992

National Library of Canada
Bibliothèque nationale du Canada

Canadian Theses Service
Service des thèses canadiennes

Ottawa, Canada
K1A 0N4

The author has granted an irrevocable non-exclusive licence allowing the National Library of Canada to reproduce, loan, distribute or sell copies of his/her thesis by any means and in any form or format, making this thesis available to interested persons.

The author retains ownership of the copyright in his/her thesis. Neither the thesis nor substantial extracts from it may be printed or otherwise reproduced without his/her permission.

L'auteur a accordé une licence irrévocable et non exclusive permettant à la Bibliothèque nationale du Canada de reproduire, prêter, distribuer ou vendre des copies de sa thèse de quelque manière et sous quelque forme que ce soit pour mettre des exemplaires de cette thèse à la disposition des personnes intéressées.

L'auteur conserve la propriété du droit d'auteur qui protège sa thèse. Ni la thèse ni des extraits substantiels de celle-ci ne doivent être imprimés ou autrement reproduits sans son autorisation.

ISBN 0-315-77096-1

Canada

UNIVERSITY OF ALBERTA

RELEASE FORM

NAME OF AUTHOR: Yongyi Li

TITLE OF THESIS: Three Dimensional Finite Element Stress-Relief Model Applied to Stress Measurement by Optical Holography

DEGREE: Master of Science

YEAR THIS DEGREE GRANTED: FALL 1992

Permission is hereby granted to THE UNIVERSITY OF ALBERTA LIBRARY to produce single copies of this thesis and to lend or sell such copies for private, scholarly or scientific research purpose only.

The author reserves other publication and other rights in association with the copyright in the thesis, and except as hereinbefore provided neither the thesis nor any substantial portion thereof may be printed or otherwise reproduced in any material form whatever without the author's prior written permission.

(SIGNED) Yongyi Li

PERMANENT ADDRESS:
Department of Physics
412 Avadh Bhatia Physics Laboratory
University of Alberta
Edmonton, Canada T6G 2J1

Date: August 26 19 92

THE UNIVERSITY OF ALBERTA

FACULTY OF GRADUATE STUDIES AND RESEARCH

The undersigned certify that they have read, and recommend to the Faculty of Graduate Studies and Research for acceptance, a thesis entitled **Three Dimensional Finite Element Stress-Relief Model Applied to Stress Measurement By Optical Holography** submitted by **Yongyi Li** in partial fulfilment of the requirements for the degree of **Master of Science** in **Geophysics**.

.....
Dr. D. R. Schmitt (Supervisor)
Department of Physics

.....
Dr. S. S. Sheinin
Department of Physics

.....
Dr. D. Ian Gough
Department of Physics

.....
Dr. D. H.-K. Chan
Department of Civil Engineering

Date: July 31 1992

ABSTRACT

Recent field work has demonstrated that recording stress relief displacements with double exposure optical holography shows promise for the quantitative determination of stresses from a borehole. A practical problem, however, is that the determination of the in situ stress requires knowledge of the stress-relief displacements on the surface of a body induced by drilling a small hole perpendicularly into the body. Two analytic displacement models have already been developed but may be in error due to the simplification in geometry and boundary conditions. Hence, the validity of these analytic models needs numerical and laboratory testing.

One part of this study consists of a three dimensional finite element analysis of the displacement induced by the drilling of a finite depth stress-relief hole into the surface of an infinite halfspace which is used to represent the borehole wall. Displacement fields are calculated for various stress-relief hole diameters, stress-relief hole depths, applied stresses and Poisson's ratios in order to determine the influence of these parameters. Comparison of the analytic to the finite element stress-relief models suggests that the analytic models may underestimate the stress magnitude by 50 to 75 percent.

A series of holographic experiments and corresponding finite element calculations were conducted on plexiglass blocks under uniaxial stress. In these experiments, both the hole depth and the applied stress magnitude were varied. The synthetic fringe patterns calculated on the basis of the finite element analysis are in agreement with the observed fringe patterns. This

agreement suggests that numerical solutions to the three dimensional stress relief displacement field may be preferable to the analytic models.

ACKNOWLEDGEMENTS

I am extremely grateful to my supervisor, Dr D. R. Schmitt for his enthusiasm, assistance and guidance which enabled me to complete this work. His constructive critiquing of my research and thesis kept me on a straight path. Sincere thanks to him for spending substantial time correcting this thesis. I also would like to thank him for his personal support which is beyond the responsibility of a supervisor.

I would like to thank Dr Norman Udey for his help in overcoming many of the computer problems and to Jay Haverstock for his help in the laboratory. I also would like to thank my officemates Ahmed Kebaili and Yanqun Wang who aided in constructing a harmonious atmosphere for my research and study.

I would like to thank Dr D. H.-K. Chan for his valuable suggestions to my research.

The great support from my family and friends abroad is also gratefully acknowledged. I would especially like to acknowledge the support and understanding from my wife, Ping, during the period of my graduate studies.

Finally, I wish to acknowledge the support of this research by Alberta Oil Sands Technology and Research Authority and the National Science and Engineering Research Council of Canada.

TABLE OF CONTENTS

LIST OF TABLES

LIST OF FIGURES

CHAPTER

1. INTRODUCTION 1

2. PRINCIPLE OF DOUBLE-EXPOSURE HOLOGRAPHY 5

   2.1 Formation of fringe patterns 5

   2.2 Relation of fringe pattern to displacement vector 10

   2.3 Forward modelling 15

3. STRESS-RELIEF DISPLACEMENT MODELS 18

   3.1 Method of stress-relief 18

   3.2 Plate model 20

   3.3 Infinite depth hole model 23

4. THREE-DIMENSIONAL FINITE ELEMENT MODELLING OF STRESS-RELIEF DISPLACEMENTS 28

   4.1 Introduction of finite element calculation 28

   4.2 Model geometry 30

   4.3 Stress-relief displacements 36

   4.4 Synthetic fringe patterns 46

   4.5 Comparison of displacement models 54

5. LABORATORY EXPERIMENT 67

5.1 Set-up and calibration 67

5.2 Finite element models 73

5.3 Experiments 79

5.4 Thermal error 90

6. CONCLUSIONS 96

REFERENCES 100

APPENDICES 105

A: Introduction of 3-D finite element method 105

B: Programs 113

LIST OF TABLES

Table

4-1 Parameters of the finite element calculations..... 39

4-2 Stress ratios between various displacement models..... 65

5-1 Coordinates in the double-exposure optical system..... 69

5-2 Holographic experiment parameters..... 80

LIST OF FIGURES

Figure

2-1 Schematic of a double-exposure holographic optical system..... 6

2-2 Reconstruction of a double-exposure hologram..... 9

2-3 Arrangement of double-exposure holographic interferometry..... 11

2-4 Forward modelling of interference fringe pattern..... 17

3-1 Stress field around a borehole..... 19

3-2 Borehole with a small, finite depth stress-relief hole 21

3-3 Simplified geometry of stress-relief model..... 22

3-4 Analytic plate and infinite depth hole models..... 25

4-1 Flow chart of finite element calculation..... 29

4-2 Computing portion of stress-relief model 31

4-3 Three dimensional finite element mesh..... 32

4-4 Stress-relief displacements for examining the effect of hole depth..... 35

4-5 An example of surface stress-relief displacements..... 37

4-6 Stress-relief displacements vs hole diameter to hole depth ratio..... 42

4-7 Stress-relief displacements vs hole depth to hole diameter ratio..... 43

4-8 Stress-relief displacements vs the applied stress to Young's modulus ratio 44

4-9 Stress-relief displacements vs Poisson's ratio 45

4-10 Variation of displacement vector with radial position 49

4-11 Synthetic fringe patterns for various stress-relief hole diameters 50

4-12 Synthetic fringe patterns for various stress-relief hole depths 51

4-13 Synthetic fringe patterns for various applied stress to Young's modulus ratios 52

4-14 Synthetic fringe patterns for various Poisson's ratios 53

4-15 Infinite plate with a circular hole in Cartesian and cylindrical coordinate system 56

4-16 Nodal stresses along the wall of a throughgoing hole of a finite element plate model 58

4-17 Comparison of stress-relief displacements for various models .... 60 - 62

4-18 Comparison of synthetic fringe patterns for various models 63

5-1 Configuration of double-exposure holographic optical system used in the laboratory 68

5-2 Schematic of the mechanical system applying an uniaxial stress to a sample 70

5-3 Output voltages of the Wheatstone bridges on frame and load cell ... 72

5-4 Stress-relief displacements of three FE models of a plexiglass sample 76

5-5 Synthetic fringe patterns of three FE models of a plexiglass sample ... 77

5-6 Synthetic fringe patterns of three displacement components of FE model 1 78

5-7 Synthetic and observed fringe patterns for plexiglass samples with varying hole depths ..... 82 - 84

5-8 Synthetic and observed fringe patterns for plexiglass samples with varying uniaxial stresses ..... 86 - 87

5-9 Synthetic fringe patterns of analytic plate model and infinite depth hole model for an example of plexiglass sample 89

5-10 Observed fringe pattern induced by thermal expansion 94

5-11 An example of the thermal effect on the fringe pattern 95

A-1 Rectangular brick element 108

Chapter 1 Introduction

The measurement of in situ rock stress is important both to constrain active tectonic processes and to support the design of subsurface engineering. Rock stresses are generally difficult to quantitatively measure due to the complexities inherent in a rock mass and the difficulties of access to measurement sites. To present, a few of the well-known quantitative measurement techniques (Hudson and Cooling, 1988) include the CSIR doorstopper cell, the USBM borehole deformation gage and the hydraulic fracturing technique. Of these, hydraulic fracturing is the only technique that has been successfully applied in a deep borehole. Since many of these techniques are often very expensive or difficult to implement, there remains much room for further development of stress measurement technology. The research presented here was motivated by the need for a relatively fast and inexpensive technique to acquire quantitatively the stress tensor from a borehole.

In the 1970's, Schmidt et al. (1974) proposed a technique to measure rock stress magnitudes from a borehole by using optical interferograms commonly referred to "double exposure holograms". The technique was further developed in series by Cohn (1983), Bass et al. (1986), Schmitt (1987) and Smither et al. (1988, 1992). In concept, double-exposure holograms are used to record stress-relief displacements induced by drilling a small hole into the wall of a borehole. The stress-relief displacements are manifested as a pattern of fringes in the resulting image. The stress tensor may then be determined

from the fringe pattern if the relationship of the displacements to the stress state at the borehole wall is known.

Consequently, in order to obtain the stresses in a stress-relief experiment, the displacement-stress model must be found. Given a combination of hole dimension, material properties, and stress magnitude level, a synthetic fringe pattern may then be calculated. If the synthetic fringe pattern is in agreement with the observed fringe pattern, then one may obtain the stresses.

Since the double exposure holograms are sensitive to all three components of the displacement field, an analytic solution to describe the displacement field induced by drilling a hole is difficult to obtain. To present, two analytic stress-relief displacement models have been proposed to describe these displacements.

The first and simplest is the plate model of Bass et al. (1986) and Schmitt, (1987), in which a small part of the wall of a borehole is approximated as an infinite, homogeneous, isotropic elastic plate with a thickness of twice the depth of a stress-relief hole. The plate is assumed to be subject to a state of plane stress. Stress-relief displacements resulting from a modelled stress-relief hole which goes through the plate are considered to model the stress-relief displacements caused by drilling on the wall of the borehole. The second analytic model consists of an infinite homogeneous, isotropic half-space with a throughgoing hole and with a plane state of stress loaded at infinity (Smither and Ahrens, 1991). Due to the lack of the laboratory calibrations and due to some differences between the synthetic fringe patterns and the observed interferograms which cannot be accommodated by the analytic models, their validity remains in question. A few queries are: Is the plane

stress assumption of the plate model sufficient to explain stress-relief displacements on the surface of a borehole due to drilling a hole? May a sufficiently deep stress relief hole be modelled by the analytic formulations? And does the existence of the bottom of a stress-relief hole substantially affect the stress-relief displacements? Because it is difficult to derive a theoretical model which allows an unambiguous resolution of the three dimensional problem we face, the numerical method of finite element analysis (FEA) is used to test the validity of the analytic models.

An analysis of the stress-relief displacements with two dimensional finite element method (FEM) was conducted by Smither et. al (1988). In this work, some significant results were obtained. In particular the effect of changing the depth of the stress-relief hole on the displacements was noted. However, the application of the results are limited because it is impossible to produce a synthetic fringe pattern from the two dimensional results. Also, the errors in substituting the two dimensional results for a 3-dimensional problem are unknown.

Due to the uncertainties inherent in the earlier analytic and two dimensional finite element models, a three dimensional FEM is introduced in this thesis. The first objective of the present research is to set up a versatile tool to provide the stress-relief displacements whatever the possible boundary conditions are. The second objective is to explore errors in the analytic models in order to judge their reliability and applicability.

This thesis is organised as follows. First, the principle of double-exposure holography, which involves the formation of the fringe pattern of an interferogram, the reconstruction of a fringe pattern, the relation of the fringe

pattern to the displacement vector and the calculation of a synthetic fringe pattern of a known displacement field, is introduced in Chapter 2

Chapter 3 briefly discusses how stresses may be measured from a borehole by drilling a small hole (the stress-relief hole) perpendicular into the borehole wall, and reviews the existing analytic displacement models and the two-dimensional FEA in detail.

The deficiencies of these prior models provide the motivation for a 3-D finite element modelling of the stress-relief displacements in Chapter 4. The geometry of 3-D finite element model (FE model) and the characteristics of its stress-relief displacements are discussed. Then, the effects of various factors, including the size of the stress-relief hole, the parameters of elasticity, and the applied stress on the induced displacements are presented. In order to explore the errors of the analytic models, a comparison between the analytic models and the finite element model is made.

Finally, Chapter 5 describes the results of a series of laboratory holographic experiments and direct comparisons between observed and synthetic fringe patterns.

Chapter 6 concludes with a summary of the findings and future research directions on this topic.

Chapter 2 Principle of Double-Exposure Holography

2.1 Formation of Fringe Patterns

The double-exposure method (e.g., Smith, 1969) is most widely used to construct interferometric fringe patterns which provide information of the displacements on the surface of an object. The method simply entails taking two consecutive holographic exposures on a single piece of film. Interference of the wavefields of the original and the changed state produce a fringe pattern which is the record of the displacement field on the surface of an object. In this chapter, the theory behind the formation of the fringe patterns is briefly discussed.

In the present study, the holographic method is applied to measure stress-relief displacements from the "blind hole" drilling of a small hole into the surface of a stressed object. When the displacements are recorded by the double-exposure holographic method, we can use the relation between the displacements and fringe pattern to obtain in situ stresses.

To create a hologram, a coherent laser light is first separated or split into two beams. One is the object beam and the other is the reference beam. The object beam is expanded or diffused to illuminate the surface of an object; this light is nonspecularly reflected from the object and illuminates the holographic film. Simultaneously, the reference beam is expanded directly onto the holographic film (Figure 2-1).

Interference of the object and reference beams within the emulsion of the film produces, upon developing, a diffraction pattern of finely spaced lines

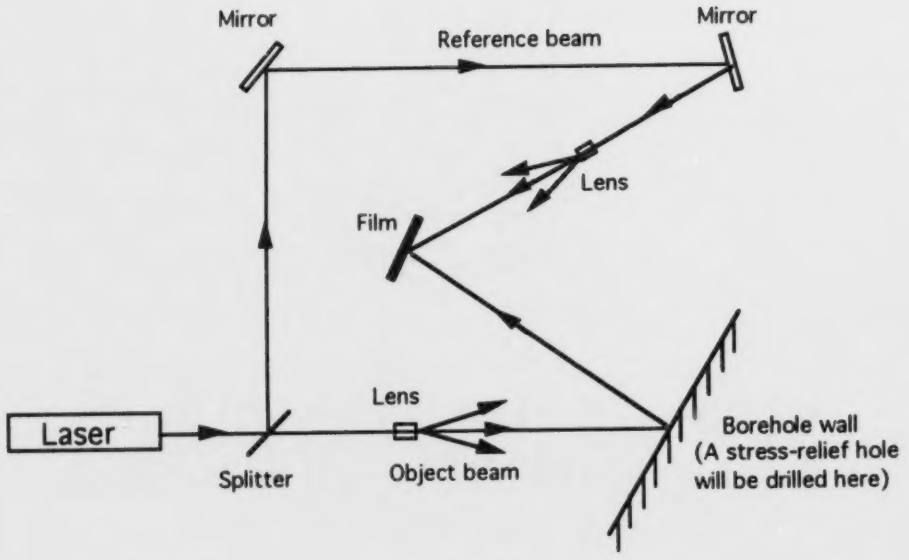

Figure 2-1 Schematic of optical holographic system used for producing a double exposure hologram.

which is called the hologram. When a replica of the reference beam is used to illuminate the hologram, this diffraction pattern "reconstructs" the original light wavefield scattered from the object; it is this wavefield which creates the three dimensional holographic image. In a double exposure hologram, two distinct wavefields are reconstructed and their interference results in the fringe pattern which provides the information on surface displacements.

In the laboratory, the holograms are reconstructed by an intense laser beam from a 30 mW He-Ne laser propagating through a point on the hologram. The resulting "real" two dimensional image appears on a plate below the hologram (Figure 2-2).

A detailed depiction of the formation of the fringe pattern of a double exposure is given by Ostrovsky et al. (1991) and briefly reviewed here. The amplitudes of light A_1 and A_2 reflected from the surface of an object in two different displacement states can be expressed as

$$A_1 = a_0 \exp(-i\phi) , \tag{2.1}$$

$$A_2 = a_0 \exp[-i(\phi+\delta)] , \tag{2.2}$$

where a_0 and ϕ are the amplitude and phase of the wave scattered by an object in its original state and δ is the strain-induced phase change of the object wave in the hologram plane. Similarly, the expression of the amplitude of the reference beam is

$$A_r = a_r \exp[(-i\psi)] , \tag{2.3}$$

where a_r and ψ are the amplitude and phase of the reference wave. The total exposure Ed after double-exposure on a film is

$$Ed = |A_1 + A_r|^2\tau_1 + |A_2 + A_r|^2\tau_2 , \tag{2.4}$$

where τ_1 and τ_2 are the time durations of the first and second exposures, respectively. Substituting equations 2.1, 2.2 and 2.3 into equation 2.4 and letting $\tau_1 = \tau_2 = \tau$, we obtain

$$\begin{aligned} Ed = {} & 2(a_0^2 + a_r^2)\,\tau + \tau a_0\, a_r \exp(i\psi)\{\exp(i\phi) + \exp[-i(\phi + \delta)]\} \\ & + \tau a_0\, a_r \exp(-i\phi)\{\exp(i\phi) + \exp[i(\phi + \delta)]\} \end{aligned} . \tag{2.5}$$

According to the curve of amplitude transmittance vs. exposure, the relation of the amplitude transmittance of a photographic layer T to the exposure may be expressed as (Smith, 1969; Francon, 1974)

$$T = b_0 + b_1 Ed , \tag{2.6}$$

where b_0 and b_1 are constants.

When reconstructing a double-exposed hologram with a reference wave (Figure 2-2), the wave at the back side of the hologram has the amplitude

$$A = T\, a_r \exp(-i\psi). \tag{2.7}$$

Substituting equations 2.5 and 2.6 into equation 2.7, we arrive at

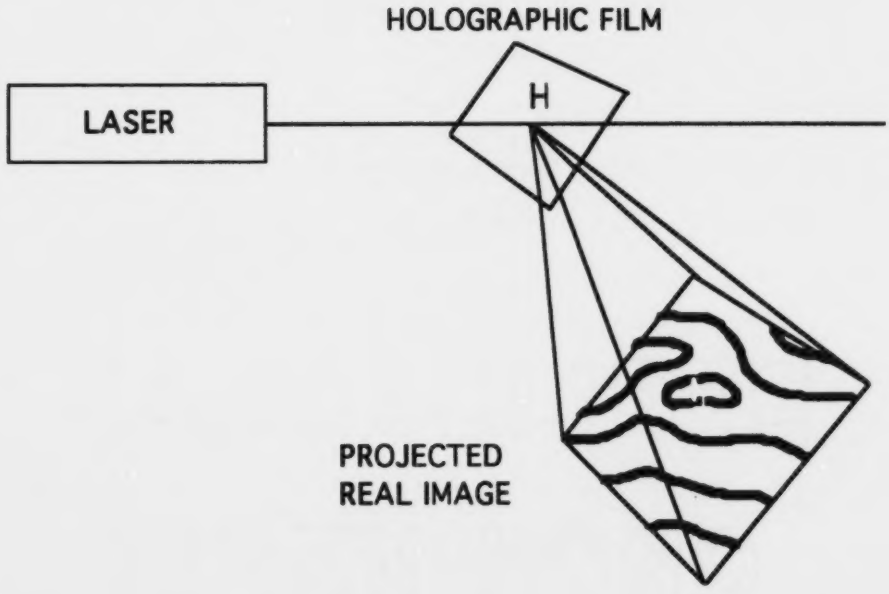

Figure 2-2 Reconstruction of a double-exposure hologram. A real image of fringe pattern is constructed by using a laser beam which illuminates a point on the hologram (after Schmitt, 1987).

$$A=\left[\, b_0 + 2b_1\tau\left(a_0^2 + a_r^2\right)\right]a_r \exp(-i\psi) + b_1\tau a_0 a_r^2\{\exp(-i\phi) + \exp[-i(\phi+\delta)]\}$$
$$+ b_1\tau a_0 a_r^2\{\exp(i\phi) + \exp[i(\phi+\delta)]\}\exp(-2i\psi), \qquad (2.8)$$

where the first term represents the zero-order wave, the second term represents the two object waves which will form a virtual image and the third term represents that a real image of the object will be formed if the hologram is illuminated by a wave which is conjugate to the reference wave. The real image then can be recorded by a film which is placed at the back of the hologram. If the distance from the hologram to the film in construction is the same as that from the object to holographic film in the experiment, an image with the same scale as the object may be obtained.

2.2 Relation of Fringe Pattern to Displacement Vector

Figure 2-3 is a ray diagram detailing the relationship between the surface displacements and the resulting change in phase for the double-exposure method. S is the source of object beam; $\mathbf{e}_s$, $\mathbf{e}_1$ and $\mathbf{e}_2$, $\mathbf{e}_3$ are the unit vectors describing the propagation directions of the illuminating and reflecting rays corresponding to the points Q and Q' on the surface of the object. The point H is the position of a point on the hologram. Q and Q' represent the original and displaced positions of a point on the surface of an object. **D** is the displacement vector from Q to Q'. $\mathbf{r}_1$, $\mathbf{r}_2$ and **R** are the radius vectors of points Q, Q' and H, respectively. The path difference between the rays from the light source through Q and Q' is

$$\Delta = SQ'H - SQH \ . \qquad (2.9)$$

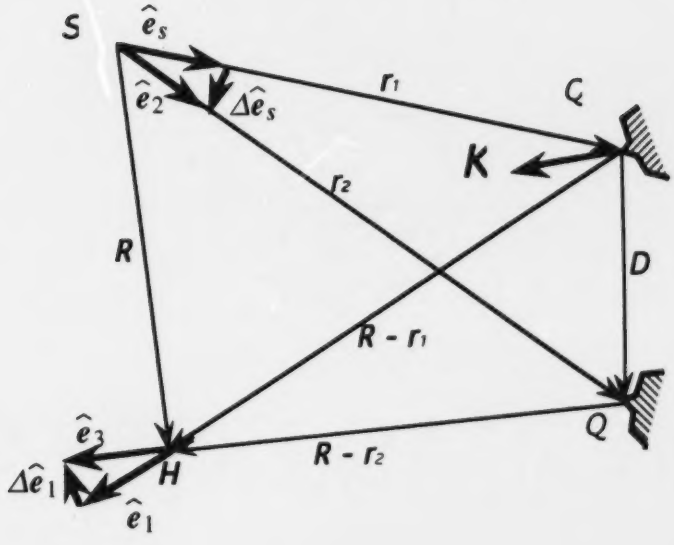

Figure 2-3 Arrangement of double-exposure holographic interferometry. S is the source of object beam, e_S, e_1, e_2 and e_3 are unit vectors of illumination and reflection corresponding to the points Q and Q'. H is the position of a point in the hologram film. Q is a point representing the original state on the surface of an object. $\mathbf{r}_1$, $\mathbf{r}_2$ and $\mathbf{R}$ are the radius vectors of points Q, Q' and H, respectively. The point Q displaces to Q' when the object is deformed. D is the displacement vector from Q to Q'.

In terms of Figure 2-3,

$$SQH = \hat{e}_s \cdot r_1 + \hat{e}_1 \cdot (R - r_1), \tag{2.10}$$

$$SQ'H = \hat{e}_2 \cdot r_2 + \hat{e}_3 \cdot (R - r_2). \tag{2.11}$$

Substituting equations 2.10 and 2.11 into 2.9, we obtain

$$\Delta = \hat{e}_2 \cdot r_2 + \hat{e}_3 \cdot (R - r_2) - \hat{e}_s \cdot r_1 - \hat{e}_1 \cdot (R - r_1). \tag{2.12}$$

The unit vectors have the relation

$$\hat{e}_2 = \hat{e}_s + \Delta\hat{e}_s, \qquad \hat{e}_3 = \hat{e}_1 + \Delta\hat{e}_1. \tag{2.13}$$

Substituting equation 2.13 into 2.12 and rearranging gives:

$$\Delta = (\hat{e}_s - \hat{e}_1) \cdot (r_2 - r_1) - \Delta\hat{e}_s \cdot r_2 - \Delta\hat{e}_1 \cdot (R - r_2). \tag{2.14}$$

Note that $|D|$ is in the order of a few microns whereas $|r_1|$, $|r_2|$ and $|R|$ are in the order of centimetres, therefore, $|r_2| > |D|$ and $|R - r_2| > |D|$ indicating that Δe_s and Δe_1 are essentially perpendicular to r_1 and $R - r_1$, whereupon the second and the third terms in equation 2.14 vanish. Then equation 2.14 simplifies to:

$$\Delta = (\hat{e}_s - \hat{e}_1) \cdot (r_2 - r_1) \tag{2.15a}$$

which is the same as

$$\Delta = (\hat{e}_s - \hat{e}_1) \cdot \mathbf{D} \quad . \tag{2.15b}$$

The phase difference δ due to the change in length of the ray paths, therefore, is

$$\delta = \left(\frac{2\pi}{\lambda}\right)(\hat{e}_s - \hat{e}_1) \cdot \mathbf{D} \quad , \tag{2.16}$$

where λ is the wave length of the coherent light. A bright fringe in the image exists under conditions of constructive interference and will appear if

$$\delta = 2\pi n \qquad (n = 0, \pm 1, \pm 2, \pm 3, \cdots) \quad . \tag{2.17}$$

Similarly, the destructive interference condition results in a dark fringe when

$$\delta = 2\pi\left(m + \frac{1}{2}\right) \qquad (m = 0, \pm 1, \pm 2, \pm 3, \cdots) \quad . \tag{2.18}$$

Here, n and m are the dark and bright integer fringe orders, respectively. Since

$$n = \frac{\delta}{2\pi} \tag{2.19}$$

and

$$m = \frac{1}{2}\left(\frac{\delta}{\pi} - 1\right) \quad , \tag{2.20}$$

then equation 2.16 can be rewritten as

$$n\lambda = \mathbf{K} \cdot \mathbf{D} \tag{2.21}$$

for bright fringe and

$$\left(m - \frac{1}{2}\right)\lambda = \mathbf{K} \cdot \mathbf{D} \tag{2.22}$$

for dark fringe. $\mathbf{K} = (\hat{e}_s - \hat{e}_1)$ is called the sensitivity vector and is a function of the geometry of the holographic apparatus, that is, the relative position of S, Q and H. **K** is called the sensitivity vector because it controls to some degree which component of the displacement vector **D** is best recorded in the fringe pattern. That is, the fringe order at a point H on the hologram results from the component of **D** in the direction of **K** as suggested by equations 2.21 or 2.22. Hence, the smaller the angle between the sensitivity vector **K** and the displacement vector **D**, the greater the representation of the displacement in the fringe pattern. Conversely, for example in equation 2.22, if **K** and **D** are perpendicular then the fringe order equals zero for a dark fringe and -0.5 for the a bright fringe. One must consider this fact in the design of the holographic recording system in order to maximize the effectiveness.

In theory, the displacement vector at a point on the surface of an object may be determined by equations 2.21 or 2.22 if the absolute fringe order is known (Ostrovsky et al., 1991). In terms of equation 2.21, to determine the three components of a displacement vector at a point requires three equations

$$\begin{aligned} \mathbf{K}_1 \cdot \mathbf{D} &= n_1\lambda \,, \\ \mathbf{K}_2 \cdot \mathbf{D} &= n_2\lambda \,, \\ \mathbf{K}_3 \cdot \mathbf{D} &= n_3\lambda \,, \end{aligned} \tag{2.23}$$

where $\mathbf{K}_1$, $\mathbf{K}_2$, and $\mathbf{K}_3$ are three different sensitivity vectors corresponding to three different illumination directions (i.e., source positions for a set of three double exposure holograms) and n_1, n_2 and n_3 are the fringe orders seen in each of the three different double exposure holograms at the same position on the surface of an object. This requires that three holograms must simultaneously be taken with three individual holographic plates at different positions. It is this rather cumbersome fact which has held up the quantitative application of double exposure holography. In our study, we do not attempt to invert the observed holographic fringe patterns for an actual displacement vector at a point on the surface of an object. Rather, we use a displacement model over an area of the object surface to construct calculated fringe patterns which may be compared on a quantitative basis to those observed.

2.3 Forward Modelling

It is experimentally difficult to record stress-relief displacements with three simultaneous holograms due to the size limitations of the borehole. Hence, we must attempt to solvė our problem with a single holographic plate by matching the observed hologram to a calculated fringe pattern deduced from a displacement field model.

A formula for constructing a synthetic fringe pattern may be derived by rewriting equations 2.16, 2.19 and 2.20 as

$$\delta_{xy} = \left(\frac{2\pi}{\lambda}\right) \mathbf{K} \cdot \mathbf{D} \quad , \qquad (2.24)$$

$$n_{xy} = \frac{\delta_{xy}}{2\pi}, \tag{2.25}$$

$$m_{xy} = \frac{1}{2}\left(\frac{\delta_{xy}}{\pi} - 1\right), \tag{2.26}$$

where δ_{xy}, n_{xy} and m_{xy} are the phase difference and the real fringe orders of bright and dark fringes, respectively, which correspond to the coordinates (x, y) on the surface of an object (Figure 2-4). Let N and M be the closest integers to the bright fringe order n_{xy} and dark fringe order m_{xy}, respectively. In our forward calculations, a bright fringe will be declared for the purpose of plotting when

$$|N - n_{xy}| \leq a \tag{2.27}$$

is satisfied. Similarly, a dark fringe will be declared if

$$|M - m_{xy}| \leq b, \tag{2.28}$$

where a and b are the ranges for the bright and dark fringes, respectively. Here, a and b are chosen equal to 0.25 to simulate the characteristics of a fringe which has a range of 0.5 from an integral dark fringe to its closest integral bright fringe. For example, if M equals zero the real numbers between -0.25 to 0.25 will form a dark fringe and 0.25 to 0.75 will form a bright fringe. The plotting of these synthetic fringe patterns will be discussed in a later section.

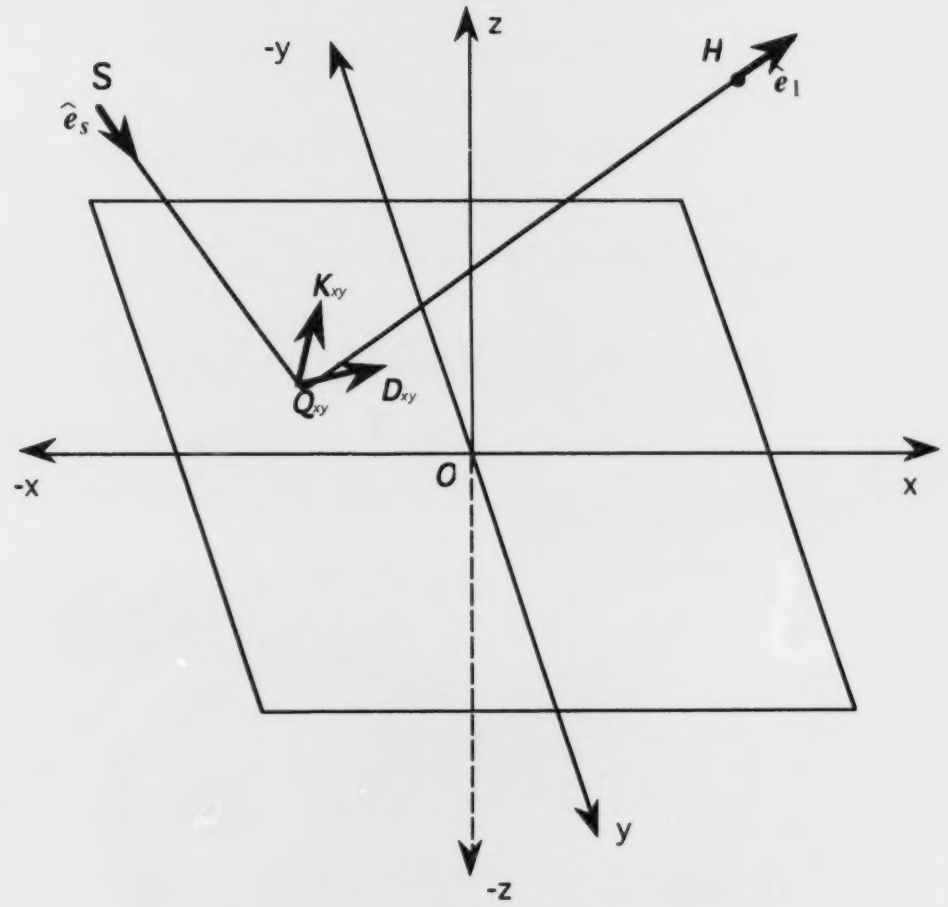

Figure 2-4 Forward modelling of fringe pattern. For a point Qxy on the surface of an object, the corresponding displacement vector is Dxy and sensitivity vector is Kxy. Fringe order at this point will be determined by equation 2.25 or 2.26. (revised from Schmitt, 1987).

Chapter 3 Stress-relief Displacement Models

In this chapter, the geometry and the stresses near a stress-relief hole drilled into the wall of a borehole will be discussed. The existing analytic displacement models: the plate model (Schmitt, 1987), the infinite depth hole model (Smither, 1991), as well as a two dimensional finite element model (Smither and Ahrens, 1988), will be reviewed. The results of analysis of these displacement models will be used for the basis in setting up the three dimensional finite element model.

3.1 Method of Stress-relief

In order to set the stage for the stress-relief displacement model we first consider a borehole drilled into a stressed medium as shown in Figure 3-1. If we only consider the stresses on the wall of the borehole, there are only three non-vanishing stresses which are $\sigma_{\theta\theta}$, the hoop stress; σ_{hh}, the stress along the axis of the borehole; and $\tau_{\theta h}$, the shear stress on the borehole wall. These stresses are related to the far-field stresses, σ_{xx}, σ_{yy}, σ_{zz}, τ_{xy}, τ_{xz}, τ_{yz}, and are expressed as (Hiramatsu and Oka, 1962; Leeman and Hayes, 1966)

$$\sigma_{\theta\theta}(\theta) = \sigma_{xx} + \sigma_{yy} - 2(\sigma_{xx} - \sigma_{yy})\cos 2\theta - 4\tau_{xy}\sin 2\theta,$$

$$\sigma_{hh}(\theta) = -\nu[2(\sigma_{xx} - \sigma_{yy})\cos 2\theta + 4\tau_{xy}\sin 2\theta] + \sigma_{zz}, \qquad (3.1)$$

$$\tau_{\theta h}(\theta) = 2(-\tau_{xz}\sin\theta + \tau_{yz}\cos\theta).$$

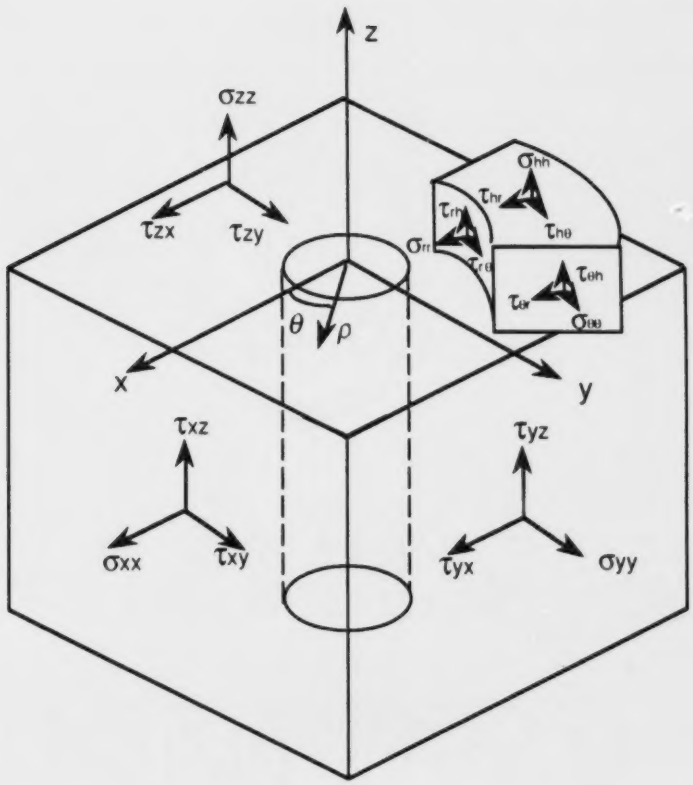

Figure 3-1 Stress field around a borehole. The far-field stresses with respect to Cartesian coordinate system and the stress components around the borehole with respect to cylindrical coordinate system. (after Leeman, 1966)

According to Leeman's method, if three sets of stress components around the periphery of a borehole are measured at different azimuths, the far-field stresses may be determined by equation 3.1. This is the theoretical basis upon which some stress measurement techniques, such as USBM borehole deformation gage technique, were developed. Quantitative determination of stress magnitudes by double-exposure holography may be used to determine the borehole wall stresses at three azimuths by optically recording the stress-relief displacements induced by drilling a small hole into the borehole wall. Figure 3-2 shows the geometry of a small, centimetre scale stress-relief hole on the wall of borehole. Since the stresses change rapidly in the radial direction from the wall of borehole, the stress-relief hole must be sufficiently shallow such that the stresses along the depth of the stress-relief hole may be approximated as uniform. Furthermore, we assume that a fringe pattern produced by micron order stress-relief displacements is constrained within a small area relative to the area of borehole wall such that the degree of curvature over this region is small in order that the area is approximately plane. The geometry of the problem is simplified as shown in Figure 3-3 where the stresses applied are assumed to be the stress components at the wall of a borehole and they are assumed uniform along the vertical direction.

3.2 Plate Model

The simplest analytic stress-relief displacement model is called the plate model (Schmitt, 1987). The model assumes the borehole wall as an infinite, isotropic, elastic plate with a throughgoing hole and with a thickness twice that of the stress-relief hole depth (Figure 3-4a). The stress-relief

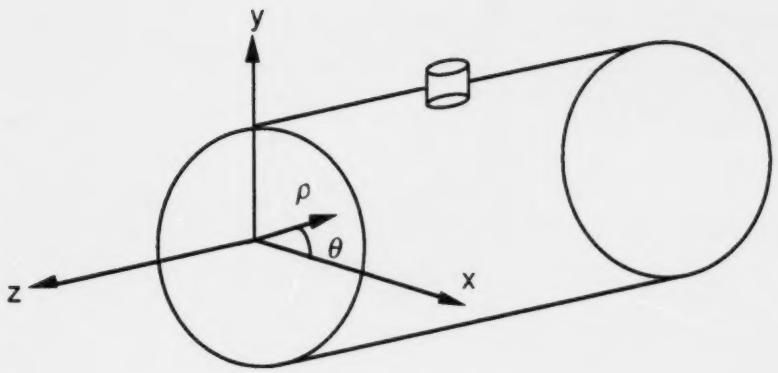

Figure 3-2 Borehole with a small, finite depth stress-relief hole.

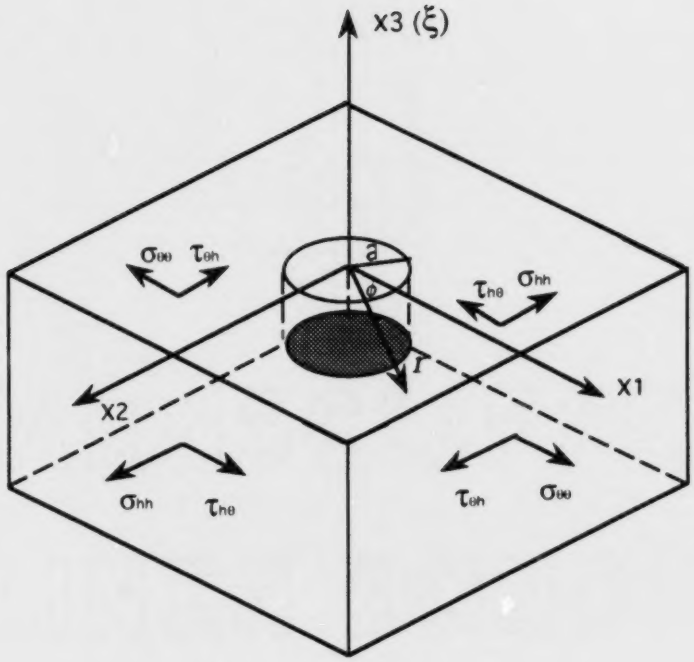

Figure 3-3 Simplified geometry for a small finite depth hole drilled into a borehole wall.

displacements on the surface which are obtained under the assumption of plane stress are

$$u_r = \frac{1}{2E}\left\{ (\sigma_{\theta\theta} + \sigma_{hh})(1+\nu)\frac{a^2}{r} + (\sigma_{\theta\theta} - \sigma_{hh})[\frac{4a^2}{r} - (1+\nu)\frac{a^4}{r^3}]\cos 2\phi + 2\tau_{\theta h}[\frac{4a^2}{r} - (1+\nu)\frac{a^4}{r^3}]\sin 2\phi \right\},$$

$$u_o = -\frac{1}{2E}\left\{ [(1-\nu)\frac{2a^2}{r} + (1+\nu)\frac{a^4}{r^3}][(\sigma_{\theta\theta} - \sigma_{hh})\sin 2\phi - 2\tau_{\theta h}\cos 2\phi] \right\}, \quad (3.2)$$

$$u_\xi = \frac{\nu a^2 t}{Er^2}[(\sigma_{\theta\theta} - \sigma_{hh})\cos 2\phi + 2\tau_{\theta h}\sin 2\phi],$$

where u_r, u_o and u_ξ are the radial, tangential and vertical displacements related a cylindrical co-ordinate system as shown in Figure 3-3, $\sigma_{\theta\theta}$, σ_{hh} and $\tau_{\theta h}$ are the stresses applied to the plate at infinity, and ϕ is the azimuth between $\sigma_{\theta\theta}$ and r. a is the radius of the stress-relief hole, t is the plate thickness, E is the elastic (Young's) modulus and υ is Poisson's ratio. Note that in this model the in-plane displacements u_r and u_o are independent of the depth of stress-relief hole, whereas the out of plane displacement u_ξ is linearly dependent on the depth.

3.3 Infinite Depth Hole Model

Smither et al. (1988, 1991) indicated that some field holograms appear to have smaller displacements near the stress-relief hole than were predicted on the basis of the simple plate model. There are two possible sources for this

error in the plate model. The first may be related to the stress-relief hole geometry (e. g., the neglect of the effect of the bottom of a stress-relief hole), and the second may be related to the plane stress assumption which is used in an elastic thin plate.

In addition, Smither et al. (1988) explored the error in the plate model by using a two dimensional finite element analysis. The results of the calculation shows that the plate model predicts larger vertical displacements and hence underestimates the in situ stresses. Calculations conducted in two dimensions, in the x_1 - x_3 plane or the x_2 - x_3 plane of Figure 3-3, does not give the stress-relief displacements on the entire surface of the model. Hence, a synthetic fringe pattern which needs stress-relief displacements on the entire surface can not be produced and the comparison with an observed fringe pattern can not be made.

In order to overcome these difficulties, Smither and Ahrens (1991) proposed a more sophisticated displacement model (the infinite depth hole model) consisting of an infinite isotopic elastic half-space with a throughgoing hole loaded at infinity under a plane state of stress (Figure 3-4b). This model was based on the plane stress relaxation approach of Youngdahl and Sternberg (1966). In the calculation of the stress-relief displacements, the principal stresses σ_1 and σ_2 at infinity are decomposed into a hydrostatic stress σ_H and a pure shear stress σ_s expressed as $\sigma_H = \frac{1}{2}(\sigma_1 + \sigma_2)$ and $\sigma_s = \frac{1}{2}(\sigma_1 - \sigma_2)$, respectively. The displacements on the surface of the model are:

$$u_r = \frac{(1+\nu)a}{E} \left\{ \frac{\sigma_H}{\rho} + \sigma_s \cos 2\theta \left[u_F^R + 4\frac{(1-\nu)}{\rho} - \frac{1}{\rho^3} \right] \right\},$$

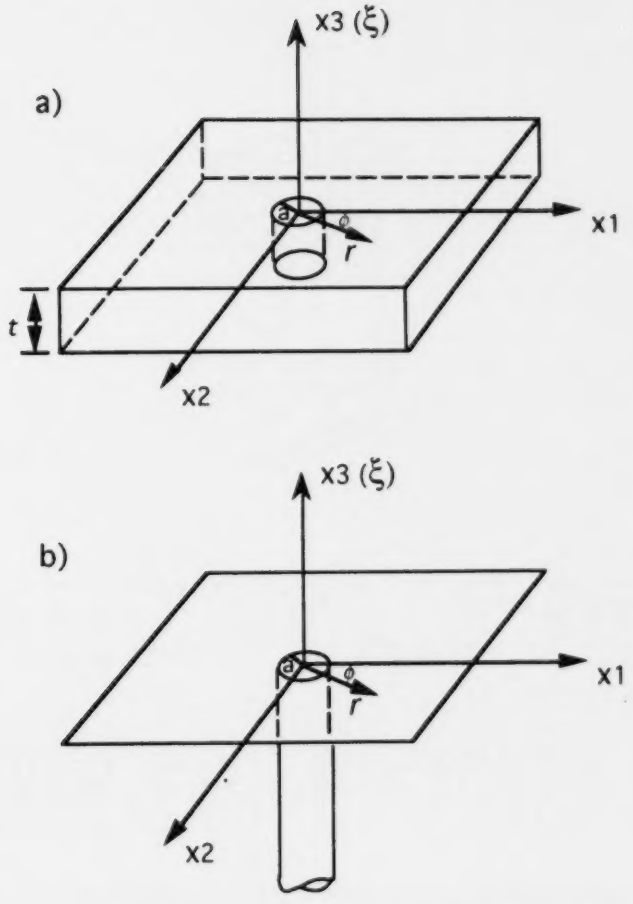

Figure 3-4 Analytic stress-relief displacement models with respect to Cartesian and cylindrical coordinate systems. (a) Plate model; (b) Infinite depth hole model.

$$u_\phi = -\frac{(1+\nu)a}{E}\left[-u_\theta^R + 2\frac{(1-2\nu)}{\rho} + \frac{1}{\rho^3}\right]\sin 2\theta\,\sigma_s$$

$$u_\xi = -\frac{(1+\nu)a}{E}\sigma_s\, u_\xi^R \cos 2\theta \qquad (3.3)$$

where u_r^R, u_ϕ^R and u_ξ^R are dimensionless quantities (Smither and Ahrens, 1991) referred to the residual displacement components of the solution to the pure shear problem, θ is measured from the σ_1 direction, and $\rho = r/a$ is dimensionless radial coordinate. Calculations demonstrate that the stress-relief displacements obtained from this model are greater than that of the plate model.

Does the infinite depth hole model more reliably predict the real displacement field due to the predicted displacements greater than that of the plate model? If so, why does the two dimensional finite element result in smaller stress-relief displacements than the plate model? The contradiction indicates that the analytic models and two dimensional FEM may in..ppropriately model the geometry and the boundary conditions related to the stress-relief problem at hand. This suggests that further work on this problem is necessary. Since it may be difficult or impossible to construct an appropriate analytic model due to the complexities of the boundary conditions, we decided to use the three dimensional finite element method (3-D FEM). The advantage of 3-D FEM is that it accounts for the complex geometry of the stress-relief hole and allows us to abandon possibly inappropriate assumptions regarding the stress state. As in the other models,

the calculated surface displacement field of the 3-D FE model shown in Figure 3-3 may be used to produce a synthetic fringe pattern. This synthetic fringe pattern may be compared to the observed fringe pattern. In the 3-D FE calculations, the model will be considered as an infinite halfspace with a small, finite depth stress-relief hole in terms of the boundary conditions in which the applied stresses are uniform in the direction of the stress-relief hole.

Chapter 4. 3-D Finite Element Modelling of Stress-relief Displacements

In this chapter, the results of three dimensional finite element modelling of the displacements induced by the drilling of a finite depth stress-relief hole into a stressed infinite halfspace are examined. In particular, the relationship of the surface stress-relief displacements to the size of the stress-relief hole, the material elastic properties, and the applied uniaxial stress will be explored. The differences between the existing analytic models and the three dimensional finite element modelling will be quantitatively compared in order to evaluate the utility of the analytic models.

4.1. Introduction of Finite Element Calculation

In the present study, 3-D FEA relies on a finite element package ANSYS. A description of the mathematical formulation for solving the nodal displacement vector {u} of a static elastic problem from the equation

$$[K]\{u\} = \{R\} \tag{4.1}$$

is reviewed in Appendix A, where [K] is the overall stiffness matrix and {R} is the nodal load vector. A flow chart of the finite element analysis is shown in Figure 4-1. There are three phases: preprocessing, solution and postprocessing, required to perform a finite element analysis by ANSYS. In the preprocessing, a model is formed by defining the coordinate systems, the element types, the nodal coordinates, the material properties and the load data. The solution phase goes through the following four steps:

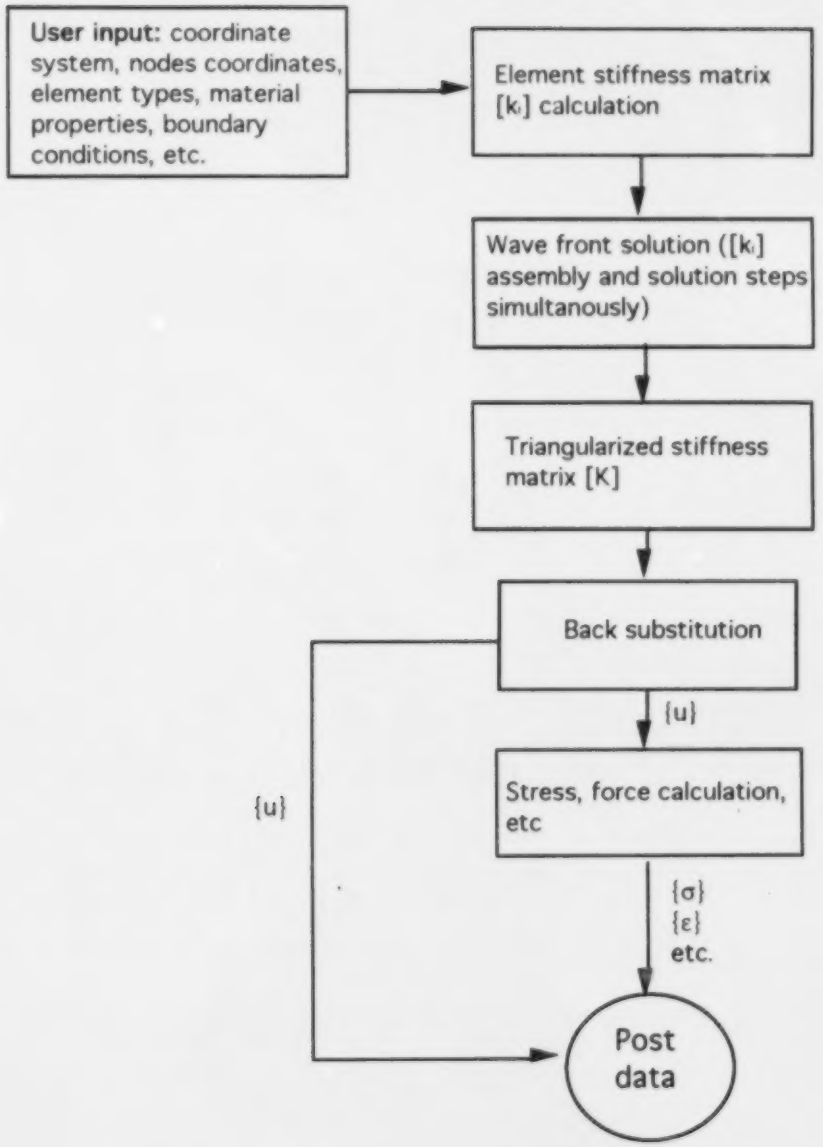

Figure 4-1 Flow chart of finite element calculation.

(1) Formulate the element stiffness matrix $[k_i]$.

(2) Assemble and triangularize the overall stiffness matrix [K].

(3) Calculate the displacement solution {u} by back substitution.

(4) Compute the strain vector $\{\varepsilon\}$, stress vector $\{\sigma\}$ and reaction forces.

The final postprocessing phase reviews the results of the analysis by producing graphics displays and tabular reports of the displacements, the stresses, and the reaction forces.

4.2. Model Geometry

Here, the problem geometry consists of an infinite halfspace with a small, finite depth stress-relief hole under a uniform applied stresses along the direction of the hole. Usually, there are errors caused by the finite element analysis which uses a limited space to model an infinite space. To reduce the error, one must limit the effect of the boundaries by making the model large relative to the range to be studied.

The finite element model is one quarter of Figure 3-3 (Figure 4-2) because of the symmetry of the problem. A mesh of the finite element model as shown in Figure 4-3 is adopted. The boundary conditions applied to the model are: (1) an uniaxial stress is applied in the y direction ($\phi = 0^0$); (2) the boundaries I, II and the bottom are constrained in the normal direction with zero displacements; and (3) the remaining boundaries, including the surface of the model, are free from constraints. Note that for convenience, the notation x_1, x_2, and x_3 of the coordinate system in Figure 3-3 is changed into x, y, and z.

Because of the existence of a stress-relief hole, stress concentration around

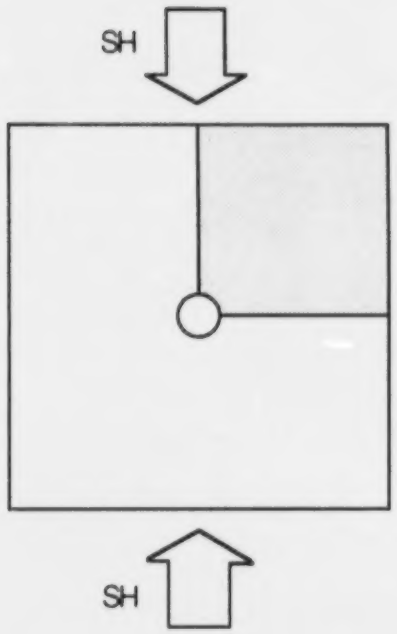

Figure 4-2 Shadow portion which is one quarter of the whole model as shown in Figure 3-3 is used in the finite element analysis. Here, SH is the applied uniaxial stress.

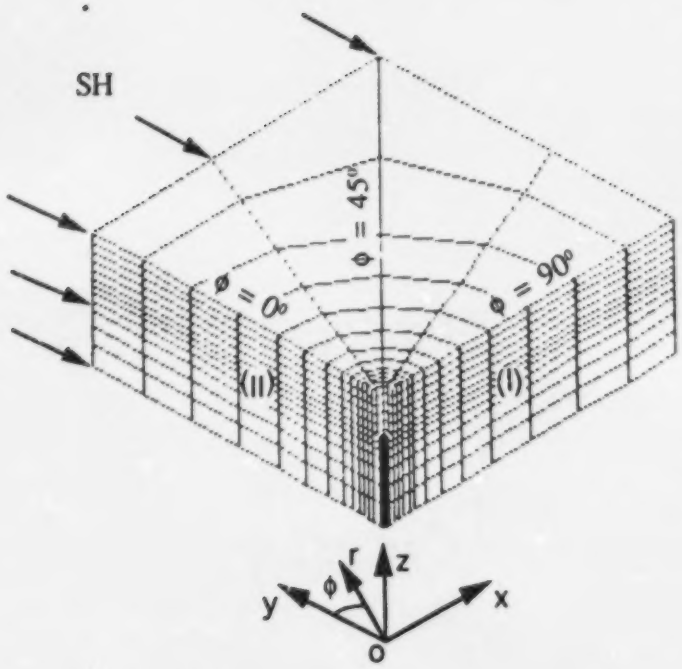

Constraints of the model :

1. Boundary I: zero nodal displacement in y direction .	
2. Boundary II: zero nodal displacement in x direction.	
3. Bottom: zero nodal displacement in z direction.	
4. z axis: zero nodal displacements in both x and y directions.	
5. Origin: zero nodal displacements in x, y and z directions.	

Figure 4-3 Three dimensional finite element model with a stress-relief hole. The model has the dimensions of 15 cm x 15 cm x 6 cm with 1101 nodes and 768 elements. The stress-relief hole has a diameter of 0.5 cm and a depth of 2.0 cm. The axes x, y and z form a globe coordinate system, and the angle ϕ, the axes r and z form a cylindrical coordinate system, where ϕ is the angle between the direction of the applied uniaxial stress and the radial direction. The uniaxial stress SH is applied in the form of surface pressure.

the stress-relief hole is expected and consequently the finite element mesh must be dense in this region. In plan view of the model, the high density mesh region around the hole is determined from the stress concentration area in an elastic thin plate with a hole (e.g., Fenner, 1986). The area defined in the radial direction from the centre is approximately five times that of the hole diameter. The area outside of the region should not experience large stress concentrations and a lower density mesh is sufficient. Around the hole, the high density mesh region in the vertical direction was determined by trial due to the lack of any prior work. This was accomplished by first obtaining a stress field from the FEA, then modifying the calculated model on the basis of where the stress concentration appears. These calculations suggest that the high density mesh volume along the vertical direction is approximately twice the hole depth. Considering the stress concentrations in the horizontal and the vertical directions, a refined three dimensional space around the hole was formed as shown in Figure 4-3.

An 8-node isoparametric solid element with orthotropic material properties was used. A prism-shaped element is formed by duplicating of two nodes. This kind of element is useful in constructing the mesh at the centre of a model.

The element loading may be input as any combination of nodal force and face pressure. In our analysis, the uniaxial stress is applied in the form of face pressure. The solution for an element includes the stress components, the principal stresses, the elastic strain components, and the principal strains. The nodal solution includes the displacement components, nodal stresses and the nodal forces. Because the output of stress components is in the form of nodal

stresses calculated from the element stresses, which are stored per element and are averaged at a node whenever two or more elements connect to the same node, the nodal stress components related to the normal direction on the free surfaces of a model may be not equal to zero. This problem will be encountered in the analysis of the stress field of the plate model.

When a hole is modelled, there are three primary factors affecting the accuracy of the stress-relief displacements, especially those on the surface of a model, due to the effect from the applied stress boundary. This effect on the surface stress-relief displacements are similar to a bending. We refer to these displacements as boundary effect displacements.

The first factor is the ratio of the model width to the model thickness; the smaller the ratio, the greater the boundary effect displacements. From trial and error if this ratio was equal to 2.5, the surface stress-relief displacements were found to converge to zero at an appropriate radial distance from the hole and the boundary effect displacements were sufficiently small to be unresolvable by the interference fringes.

The second factor is the ratio of the hole depth to the model thickness which primarily affects the surface vertical displacement. Figure 4-4 shows an example of the stress-relief displacements along the direction of the stress-relief hole wall at the radial distance of the hole radius for a model with thickness of 12.0 cm and a hole depth of 2.0 cm (i. e., the ratio is equal to 6.0). From the figure, the radial and the tangential displacements rapidly converge to zero near the bottom of the hole. The vertical displacements, however, do not converge to zero until the bottom boundary of the model. There results suggest that the optimum model should have as large a ratio as

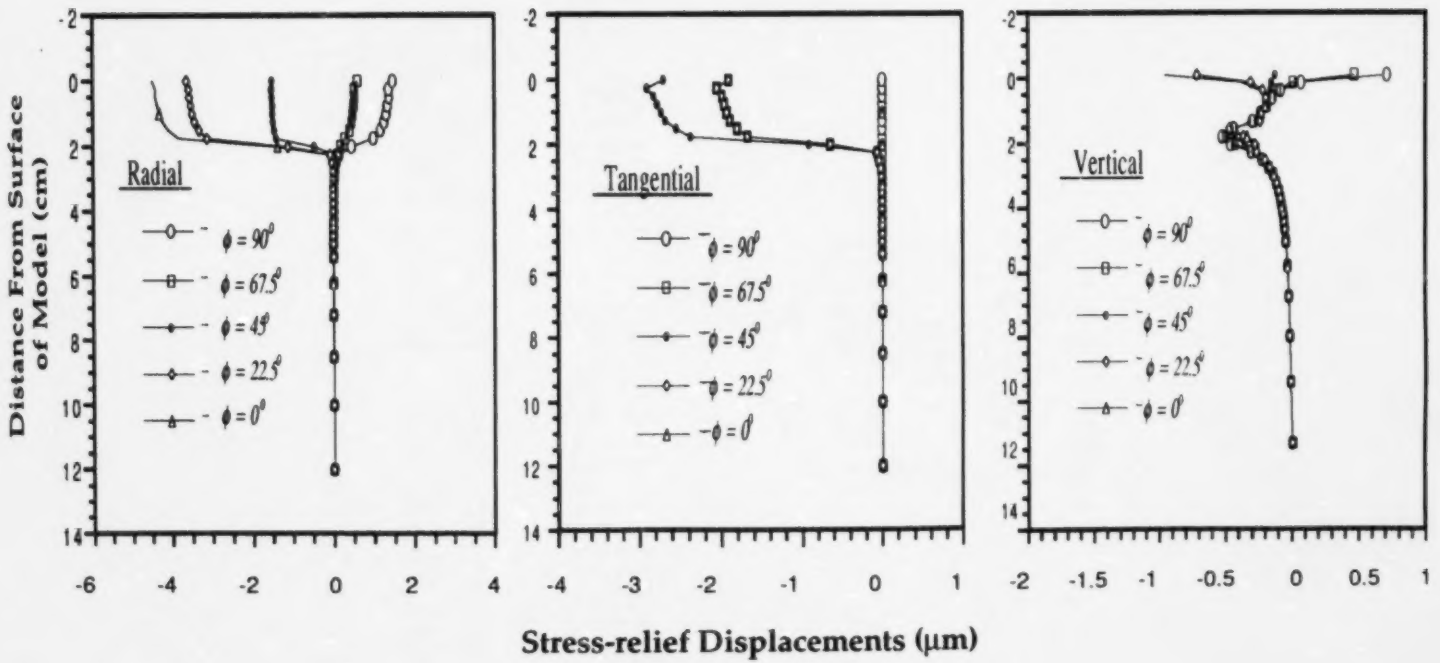

Figure 4-4 Stress-relief displacements of a finite element modelling from the surface (0.0 cm) to the bottom (12.0 cm) at the radial position of the stress-relief hole wall. The FE model has dimensions of 30 cm x 30 cm x 12 cm (thickness) with a stress-relief hole diameter of 0.5 cm and a depth of 2.0 cm. The radial and tangential displacements convergence to zero near the bottom of the hole (2.0 cm), but the vertical displacement convergences to zero until at the bottom boundary of the model.

possible. A ratio of 6.0 or more was found appropriate for the calculations.

A final factor is the ratio of the width of model to the diameter of a stress-relief hole. The larger the diameter is, the greater the boundary effect displacements. If the ratio is too small the boundary effect displacements will contaminate the displacements induced by the stress-relief hole. In the calculations and again on the basis of trial and error, 15.0 was adopted as the smallest value of this ratio. In most of the models, this ratio was either 30.0 or 60.0.

A program of ANSYS 4.4 used for computing a finite element model is given in Appendix B (Program I).

4.3. Stress-relief Displacements

As regards a FEA, a two step process is needed to calculate the stress-relief displacements. First, the displacements without a stress-relief hole and subject to the desired stresses are calculated. Next, the same calculation is performed for the model but this time containing a finite depth stress-relief hole. The stress-relief displacements are the difference between the displacements of these two calculations. In our study, the surface stress-relief displacements are of the most concern because they will be used to produce a synthetic fringe pattern for comparison with the observed fringe pattern.

Figure 4-5 gives an example of the surface stress-relief displacements in the cylindrical coordinate system for a model with a hole diameter of 0.5 cm and a depth of 2.0 cm, a Poisson's ratio of 0.25, and a ratio of the applied stress to Young's modulus (SH/E) of 1.0 MPa/GPa. In this case, negative radial displacements denote motion towards the hole axis, that is, the hole presses

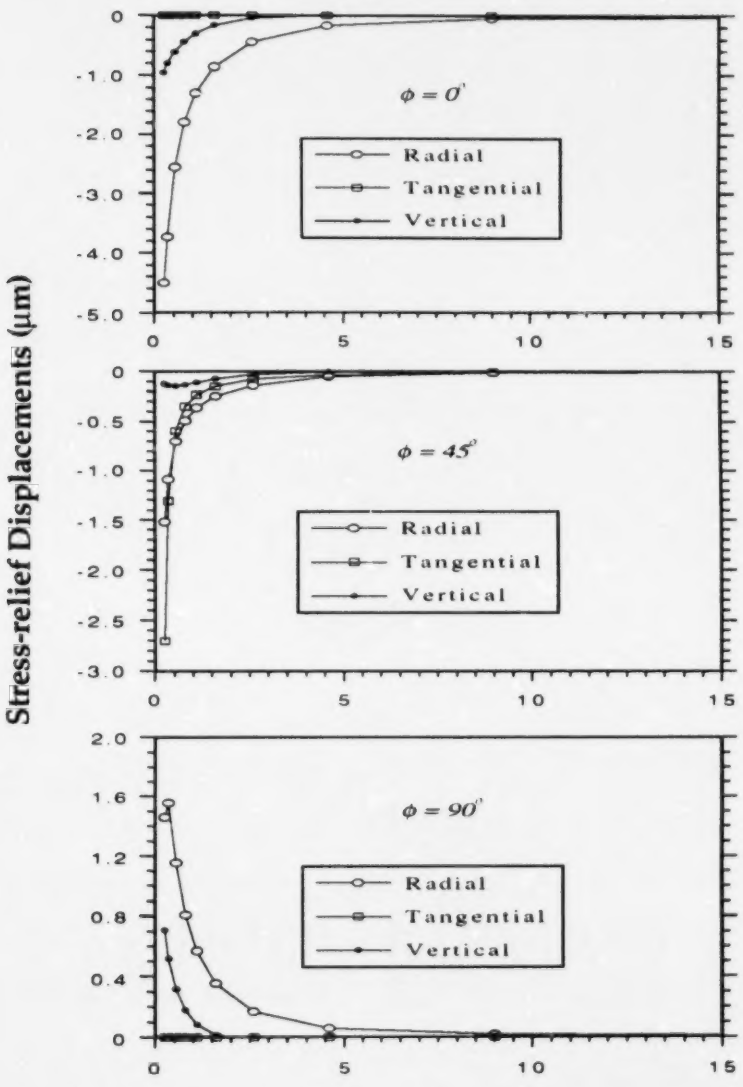

Figure 4-5 Surface stress-relief displacements of a FE model with the dimensions of 30 cm x 30 cm x 12 cm (thickness) and with a stress-relief hole of a diameter of 0.5 cm and a depth of 2.0 cm. The model has a ratio of the applied uniaxial stress to Young's modulus of 1.0 MPa/GPa and Poisson's ratio of 0.25.

inward. Negative vertical displacements indicate that the surface of the model is displaced down whereas positive vertical displacements imply outward bulging. Hence, at ϕ equal to 0^0 and 45^0, the model surface moves in and down towards the hole. At ϕ equal to 90^0, the model surface bulges outward from the surface. These displacements form a saddle shaped surface near the stress-relief hole.

The primary variables affecting the magnitude and distribution of the induced displacements are the size of the stress-relief hole, the elastic properties of material, and the magnitude of the applied stress. The effect of these variables on the induced surface displacements are discussed below in terms of the displacements on the boundary of the stress-relief hole at ϕ equal to 0^0, 45^0 and 90^0.

Table 4-1 summarizes all the parameters used in the finite element calculations.

For the size of the stress-relief hole, the two parameters of diameter and depth, are considered. This is fundamental to the relationship between the stresses and the stress-relief displacements in the design of a field experiment as we must know what drilling depths and diameters are appropriate for proper measurement of typical stress levels in the crust.

A model of width 15.0 cm and thickness 6.0 cm, with 1101 nodes and 768 elements, was used to explore the effect of the hole diameter on the displacements. In this series of calculations, the hole diameter was the only variable. The hole depth (2.0 cm), the elastic modulus E (20.0 GPa), Poisson's ratio υ (0.25) and the applied stress SH (20.0 MPa) were held constant. Figure 4-6 gives the result for stress-relief displacements at the edge of the hole in the

Table 4 -1 Parameters of the Finite Element Calculations

Variables of calculation	Size of model (cm) x*	y**	z***	Nodes	Elements	Size of hole (cm) diameter	depth	υ	E (GPa)	SH (MPa)
Hole diameter	15	15	6	1101	768	0.3, 0.5, 1.0, 1.5, 2.0	2.0	0.25	20	20
Hole depth	30	30	12	1782	1352	0.5	0.5,1.0,1.5,2.0 2.5,3.0,3.5,4.0	0.25	20	20
Poisson's ratio	15	15	6	1101	768	0.5	2.0	0.15,0.25 0.35,0.45	20	20
Applied stress	15	15	6	1101	768	0.5	2.0	0.25	20	2.5,5,10,15, 20,30,40

*width in x direction. **width in y direction. ***Thickness.

directions of ϕ equal to 0^0, 45^0 and 90^0 for hole diameters of 0.3 cm, 0.5 cm, 1.0 cm, 1.5 cm, and 2.0 cm.

In Figure 4-6, the relationship between the hole diameter (for a constant hole depth) and the stress-relief displacements is nonlinear. Secondly, the radial displacements at $\phi = 90^0$ increase from roughly 0.6 μm to 4.5 μm and decrease at $\phi = 0^0$ from -0.25 μm to -16.1 μm. The vertical displacements increase at $\phi = 90^0$ from 0.25 μm to 2.6 μm and decrease at $\phi = 0^0$ from zero to -4.0 μm. The variation of the displacements is very large, therefore, control of the stress-relief hole diameter in practice is important.

The depth of the stress-relief hole is also a crucial parameter in our study because in a stress measurement using the holographic stressmeter the depth of the stress-relief hole is limited by practical experimental constraints. A query here is at which depth of stress-relief hole will the deepening of the hole result in no further variation in the stress-relief displacements. In other words, may the hole depth be neglected after a certain depth or does the hole depth always remain a significant variable? In order to explore this question, a model of width 30.0 cm, and thickness 12.0 cm with 1782 nodes and 1352 elements was used. The calculations were conducted with stress-relief hole depths of 0.5 cm to 4.0 cm with an interval of 0.5 cm. The constant variables are the hole diameter (0.5 cm), Poisson's ratio (0.25), Young's modulus (20 GPa), and the applied stress (20 MPa).

Conceptually, the holographic stress-relief technique is similar to residual stress measurements in nondestructive tests. The difference is that the measurement of residual stress by the hole-drilling technique employs strain gages to measure the surface deformation of an object. In terms of the

experience in residual stress measurement, if the residual stresses are uniform with depth, the surface strains around the hole are fully relieved when the hole depth is approximately equal to the hole diameter (Rendler and Vigness, 1966; Flaman and Manning, 1985).

Since strain gage measurement is not sensitive to the surface normal displacements, the residual stress measurement consists of an analysis of the in-plane strain or displacements only. If we do not consider the vertical displacements here the finite element analysis supports, to a degree, Rendler and Flaman's conclusion (Figure 4-7). That is, when the hole depth equals the hole diameter, (i. e., when the ratio of the hole depth to the hole diameter is equal to 1.0), the radial displacement approximates its minimum value (-4.5 μm) at ϕ equal to 0^0 and 70 percent of its maximum value (1.5 μm) at ϕ equal to 90^0. However, the vertical displacements are not so well behaved. For example, if we assume that the vertical displacement is at its limit with ratio 8.0, then only about 45 percent of the displacement at $\phi = 90^0$ is relieved when the hole diameter equals the hole depth. Therefore, due to the variation of the vertical displacements and their substantial influence in holographic stress measurement, the ratio of hole depth to hole diameter of 1.0 cannot be used as an experimental guide-line. This effect is especially crucial when the object beam has a small angle with respect to the normal direction of a surface, whereupon the surface normal displacements are more heavily weighted.

The stress-relief displacements as a function of the ratio SH/E for a stress-relief hole diameter of 0.5 cm and a depth of 2.0 cm, a Young's modulus of 20 GPa, and a Poisson's ratio of 0.25 are plotted in Figure 4-8. The SH/E ratios used in the calculations were 0.125, 0.25, 0.75, 1.0, 1.5, and 2.0 MPa/GPa. As

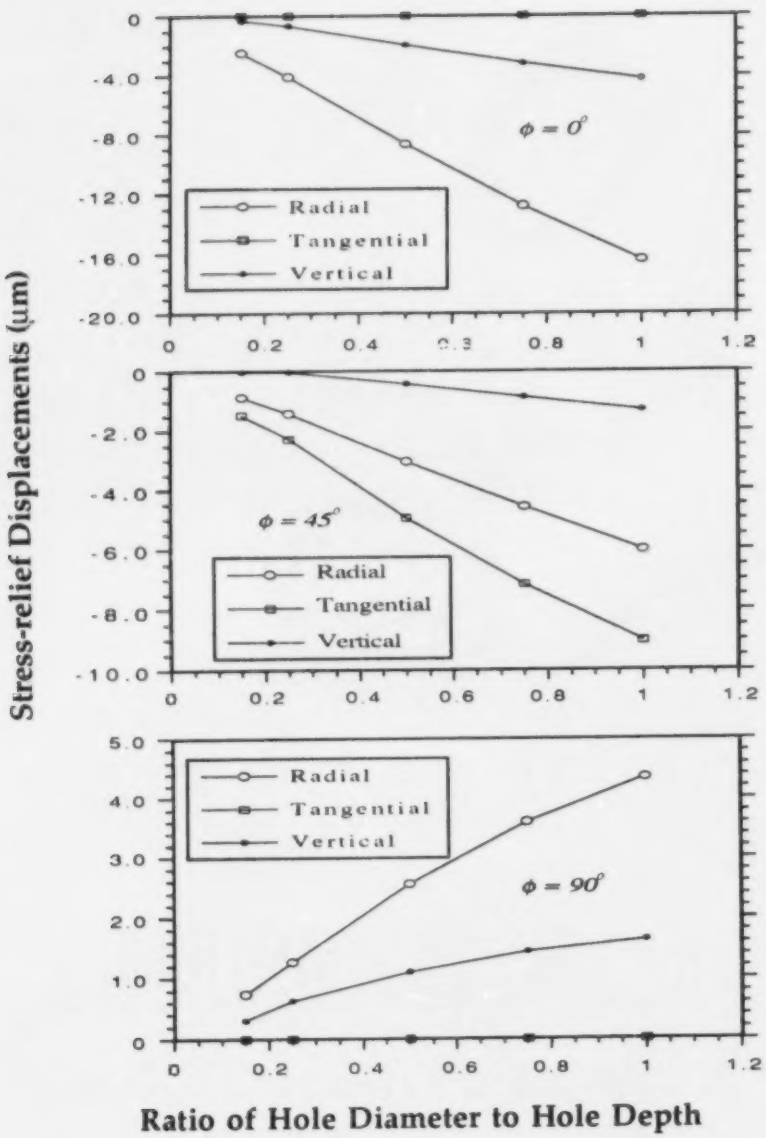

Figure 4-6 Stress-relief displacements vs. ratio of stress-relief hole diameter to depth (2.0 cm) for $\phi = 0^0$, $\phi = 45^0$, and $\phi = 90^0$ at a ratio SH/E equal to 1.0 MPa/GPa and Poisson's ratio equal to 0.25.

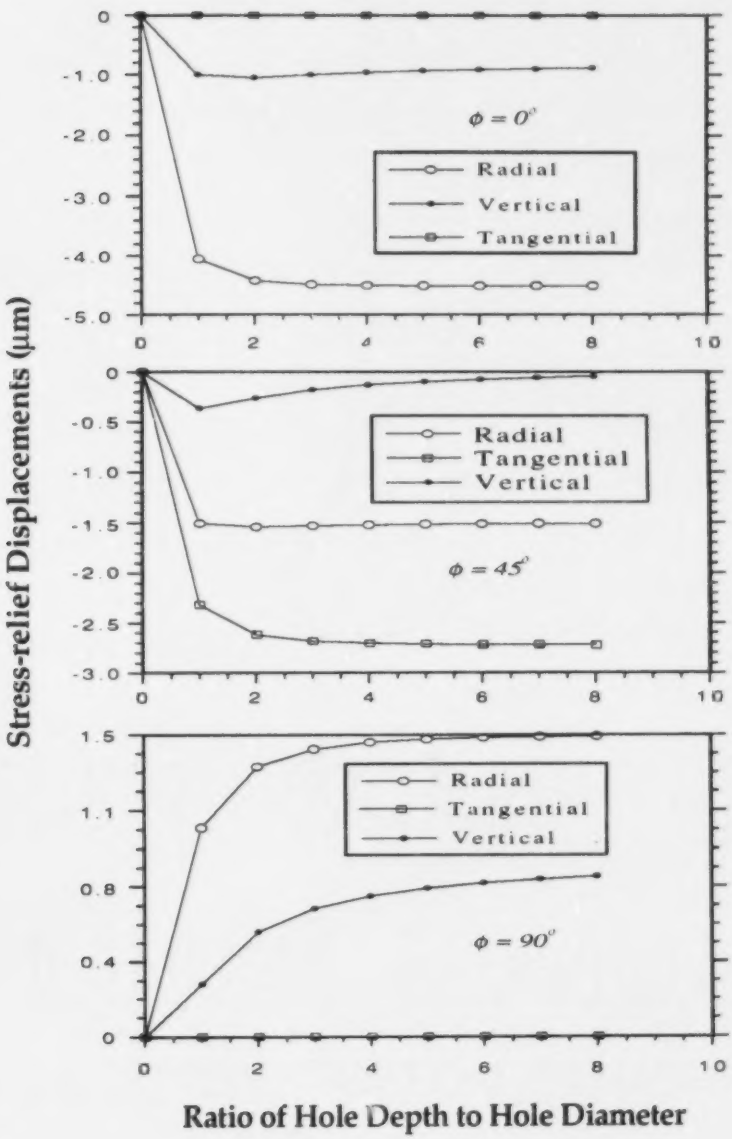

Figure 4-7 Stress-relief displacements vs. the ratio of stress-relief hole depth to stress-relief hole diameter (0.5 cm) for $\phi=0^0$, $\phi = 45^0$, and $\phi = 90^0$ at a ratio of SH/E equal to 1.0 MPa/GPa and Poisson's ratio equal to 0.25.

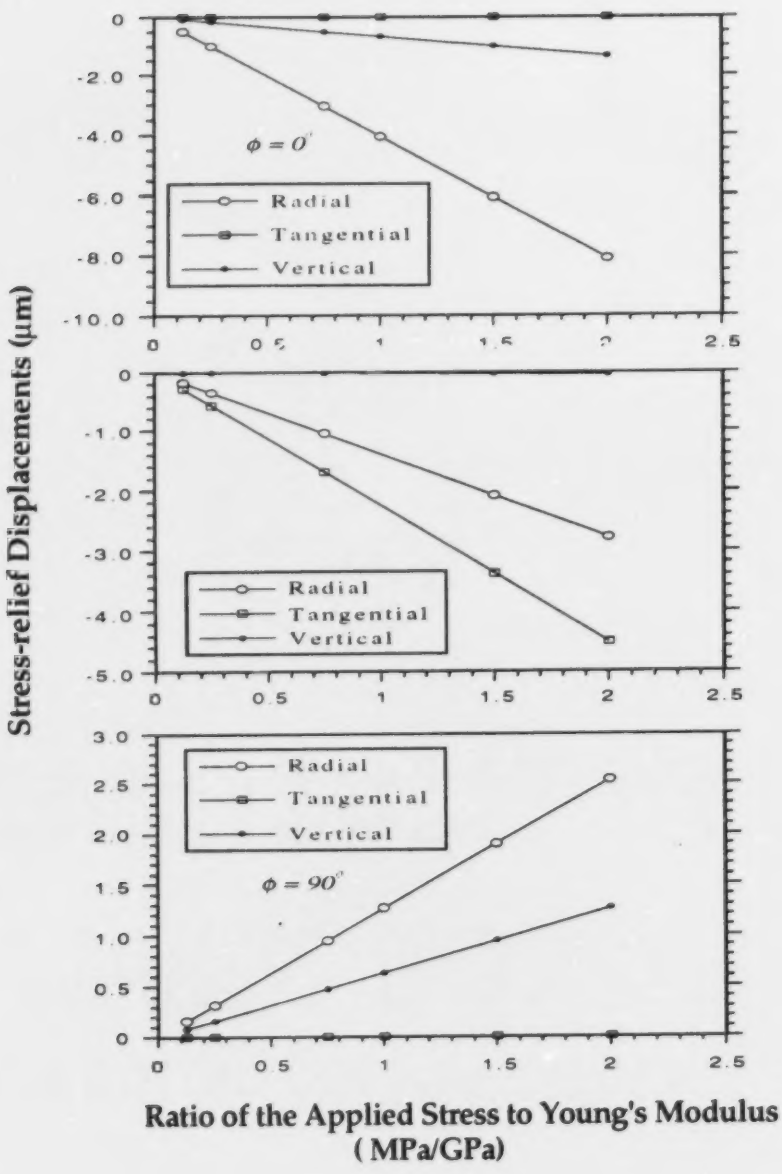

Figure 4-8 Stress-relief displacements vs. ratio of the applied stress to Young's modulus (SH/E) for $\phi = 0^0$, $\phi = 45^0$, and $\phi = 90^0$ with a stress-relief hole of a diameter of 0.5 cm and a depth of 2.0 cm.

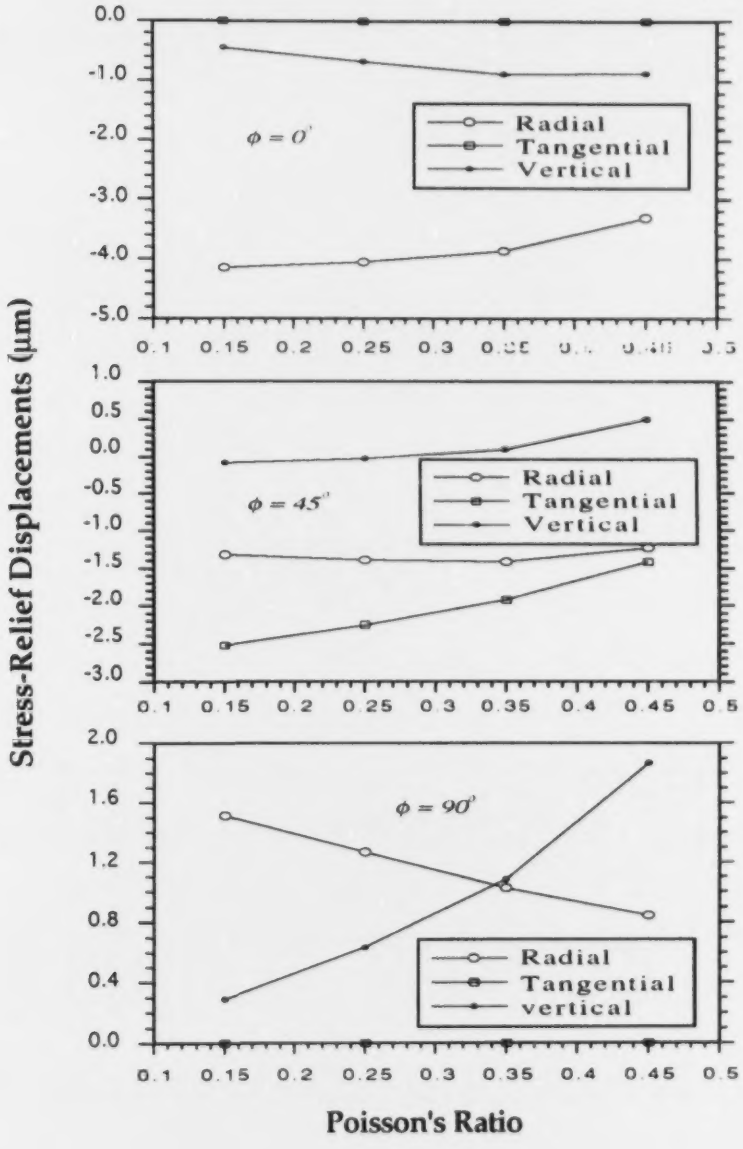

Figure 4-9 Stress-relief displacements vs. Poisson's ratio for $\phi = 0^0$, $\phi = 45^0$, and $\phi = 90^0$ with a stress-relief hole diameter of 0.5 cm and a depth of 2.0 cm and with a ratio of the applied stress to Young's modulus of 1.0 MPa/GPa.

seen in Figure 4-8, all stress-relief displacements vary linearly with SH/E ratio. This characteristic shows that the existence of a stress-relief hole does not affect the relationship of elasticity between the displacements and the applied stresses. The linear relation is expected and is useful in that it will allow simplification of further stress analysis. That is, for a rock with a given set of elastic properties, one needs only to set up its linear relation by using a few calculations and then scaling the results to obtain the displacement field expected. The fact that the displacements are linear with respect to the SH/E ratio further indicates that the goodness of the finite element modelling as a nonlinear response would indicate an erroneous solution.

Finally, the stress-relief displacements are calculated for the values of Poisson's ratios of 0.15, 0.25, 0.35, and 0.45. The hole diameter (0.5 cm), the hole depth (2.0 cm), Young's modulus (20.0 GP) and the applied stress (20.0 MPa) were held constant. The results of these calculations at ϕ equal to 0^{o}, 45^{0} and 90^{o} are given in Figure 4-9. Compared with the above factors related to the dimensions of stress-relief hole and the SH/E ratios, the effect of Poisson's ratio on the stress-relief displacements is more complex. For example, the magnitude of radial displacements increases while the magnitude of the vertical displacements decreases with Poisson's ratio at ϕ equal to 90^{o}. This relationship switches at ϕ equal to 0^{0}.

4.4 Synthetic Fringe Patterns

A surface stress-relief displacement field from the finite element analysis is transformed to a synthetic fringe pattern by the forward modelling mentioned in section 2.3. These calculations are conducted first by the

program DISFRI (Program II in Appendix B) which first calculates the stress-relief displacements by subtracting nodal displacements for the finite element modelling without a stress-relief hole from the modelling with a stress-relief hole. Next DISFRI calculates the corresponding fringe orders from the obtained stress-relief displacements. The fringe orders are then interpolated by UNIMAP in UNIRAS (Program III in Appendix B) into a 200 x 200 grid. The fringe pattern image is then plotted by the program FRIIMA in UNIRAS (Program IV in Appendix B) over a 10 x 10 cm^2 area with a superposed centimetre net. For the synthetic fringe patterns to be shown, the vertical direction (y axis) is the direction of the applied uniaxial stress and the horizontal line crossing the centre of the hole is the x axis.

Here, equation 2.26 is used to calculate the fringe orders. Hence, when a zero stress-relief displacement appears, the corresponding bright fringe has order -0.5. In the synthetic fringe pattern calculations, the coordinates of source S of the object beam (9.7, 0.0, 23.5) and the centre of the hologram (0.0, 0.0, 17.85) in centimetre, respectively, as well as the laser wave length (632.8 nm), are the same as those to be used in the holographic experiments. This optical configuration gives the vertical displacements more weight than the horizontal displacements in the formation of fringe pattern because the angle between the object beam and the normal direction of the surface of object is only 17^0.

The position of the source point of the object beam affects the shape of fringe pattern (Nelson and McCrickerd, 1986) as the sensitivity vector will differ. Combining Nelson and McCrickerd's explanation with the coordinates of the source point S and the observation point H in our calculations, the

fringe patterns are symmetric with respect to x axis because S, H and the centre of the hole, are all within the x-z plane (Figure 4-10). The greater phase shifts occur on the right side of the image because S has positive value of x and consequently the displacement vectors on the right are more closely aligned with the sensitivity vector. Therefore, denser packing of interference fringes would be expected on the right side of the patterns despite the fact that the displacement field is symmetric with respect to the x and y axes.

The fringe patterns for different sizes of stress-relief holes, SH/E ratios and Poisson's ratios are presented based on the FE calculations. Both the fringe order and density are high in the vicinity of a stress-relief hole as would be expected for the larger displacements there. In some cases, the density even exceeds our ability to resolve individual fringes in the 200 x 200 point grids. Thus, lower order fringes that are more removed from the stress-relief hole may be used to determine stress magnitudes.

The fringe patterns which have different hole diameters corresponding to the calculations of Figure 4-6 are shown in Figure 4-11. This type of study will aid in the choice of an appropriate stress-relief hole diameter both in the laboratory experiments and in the borehole measurements. In Figure 4-11, the fringe patterns change rapidly with increasing diameter of the stress-relief holes. The fringe patterns for the larger hole diameter easily exceed the expected bounds. Only the first fringe pattern for a 0.5 cm diameter hole has the fringe pattern 'butterfly' lobes contained within a limited area. Here, the fringe of order -0.5 represents zero stress-relief displacements located outside of the 'butterfly'. Consequently, a hole diameter of 0.5 cm may be used in the laboratory experiments..

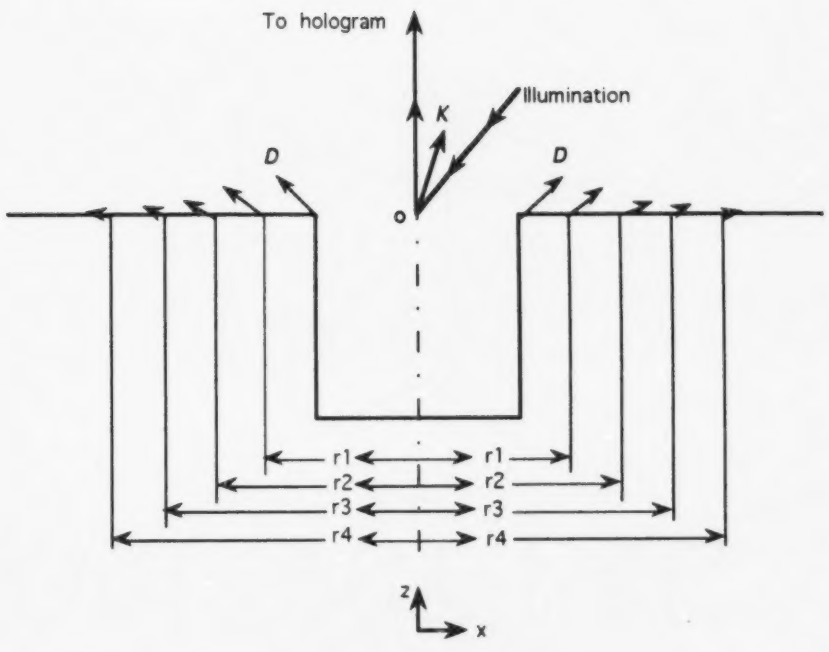

Figure 4-10 Variation of displacement vector with radial position when a hole is drilled and the relation between the sensitive vector ***K*** and the displacement vectors when an uniaxial stress is applied in the direction normal to x-z plane (y direction) as shown in Figure 4-3. On the left side, the fringes are less dense because the angle between the sensitivity vector and the displacement vector is large, and on the right side, the fringes are denser because the angle is small.

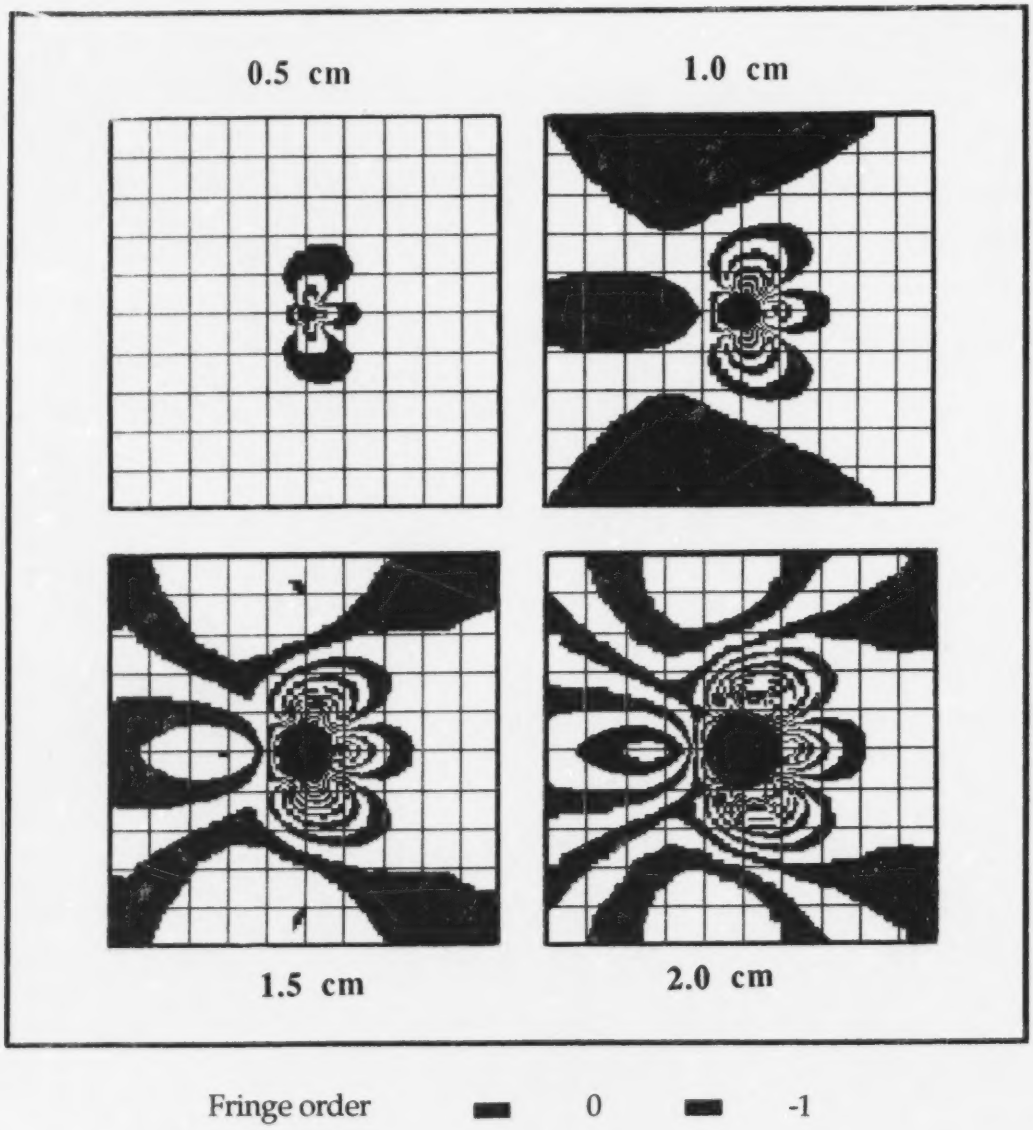

Figure 4-11 Synthetic fringe patterns for stress-relief hole diameters equal to 0.5 cm, 1.0 cm, 1.5 cm, and 2.0 cm, and constant depths equal to 2.0 cm. The FE model has the ratio of the applied stress to Young's modulus of 1.0 MPa/GPa and Poisson's ratio of 0.25. The fringe patterns are shown in an area of 10.0 cm x 10.0 cm with centimetre grids.

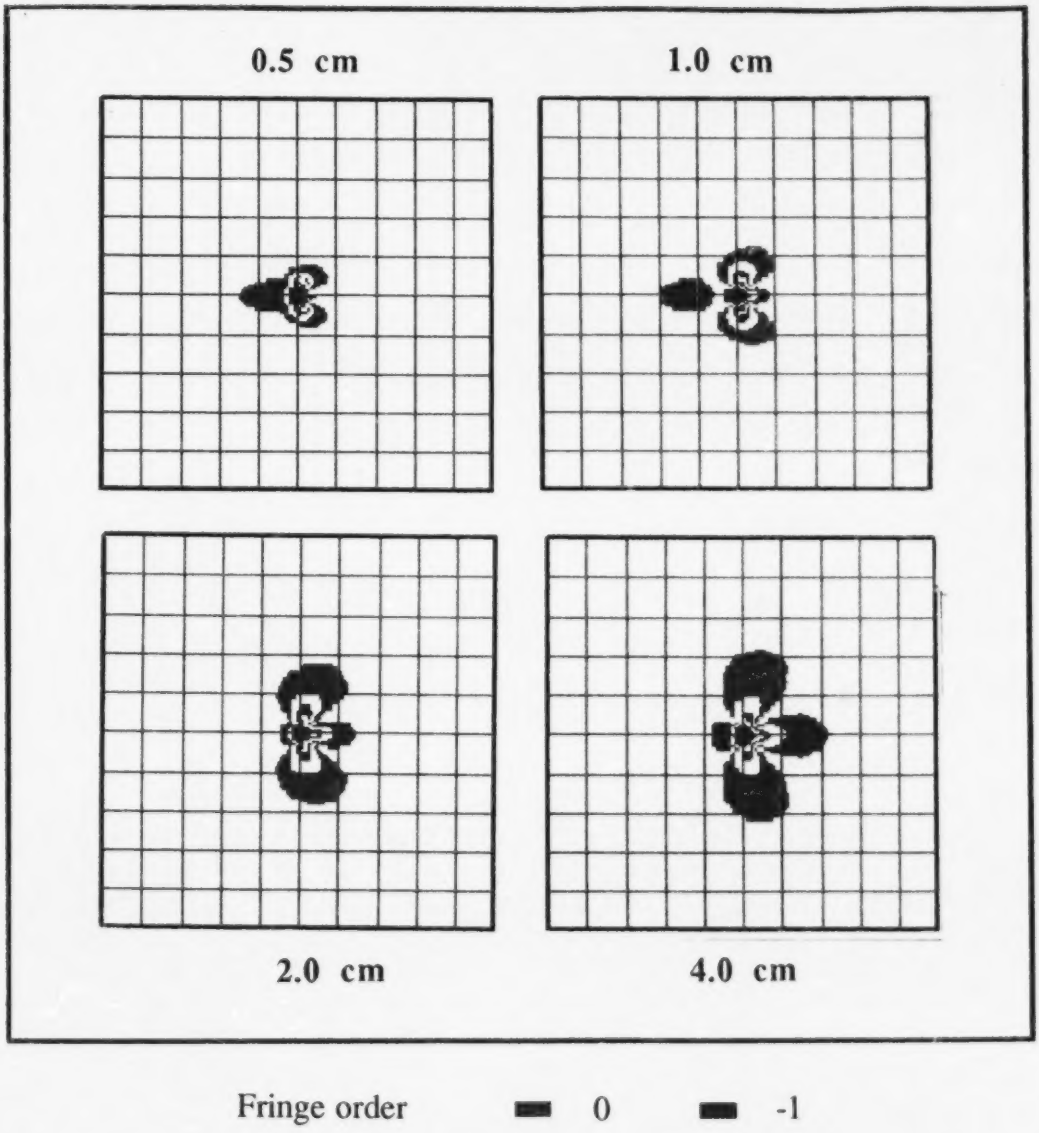

Figure 4-12 Synthetic fringe patterns for stress-relief hole depths equal to 0.5 cm, 1.0 cm, 2.0 cm, and 4.0 cm, and constant diameters equal to 0.5 cm. The FE model has the ratio of the applied stress to Young's modulus of 1.0 MPa/GPa and Poisson's ratio of 0.25. The fringe patterns are shown in an area of 10.0 cm x 10.0 cm with centimetre grids.

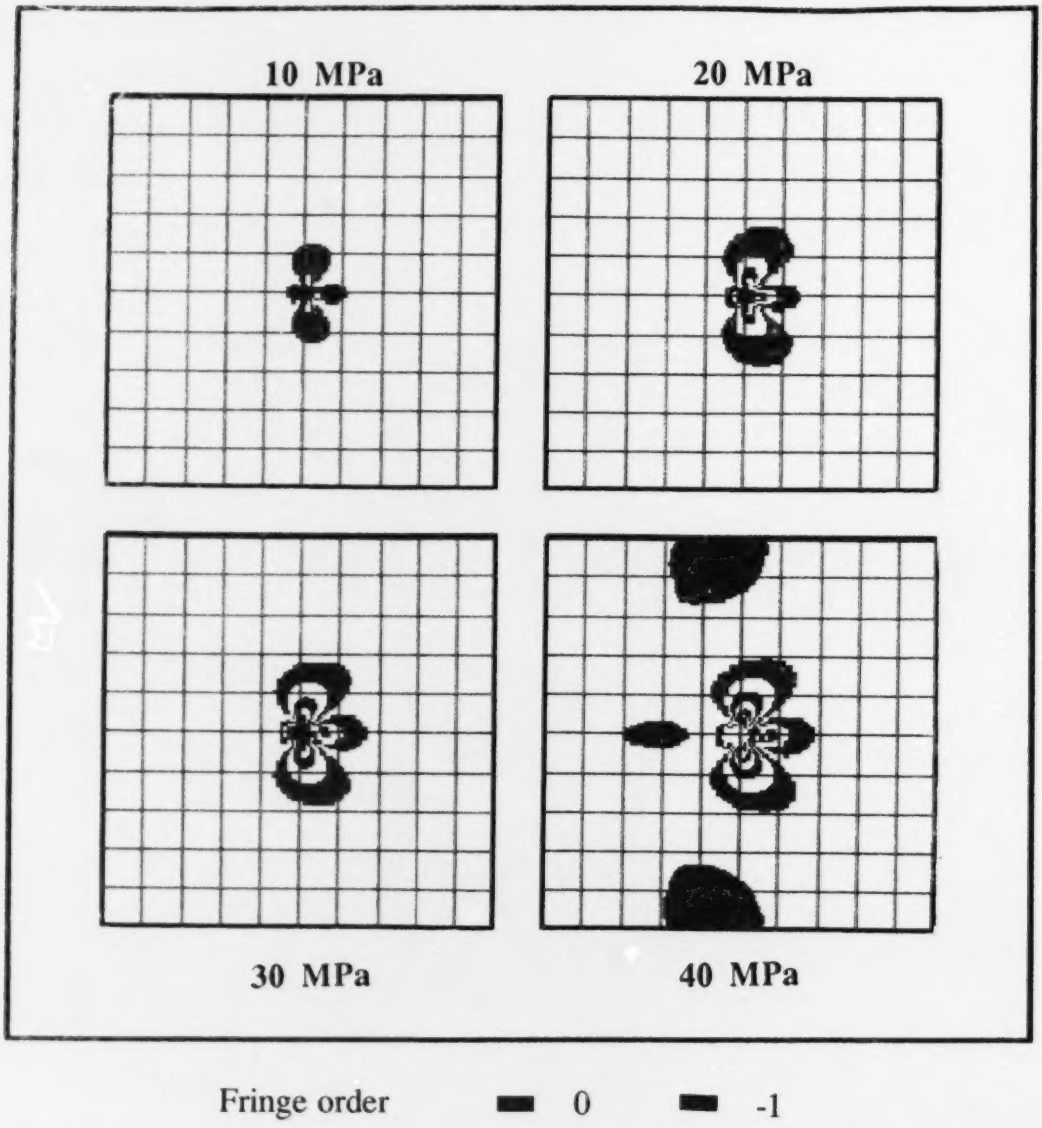

Figure 4-13 Synthetic fringe patterns for the applied uniaxial stresses equal to 10MPa, 20 MPa, 30MPa, and 40 MPa with a constant Young's modulus = 20 GPa (SH/E ratios are equal to 0.5, 1.0, 1.5, and 2.0 MPa/GPa). The FE model has the hole diameters of 0.5 cm and the hole depths of 2.0 cm and Poisson's ratio of 0.25. The fringe patterns are shown in an area of 10.0 cm x 10.0 cm with centimetre grids.

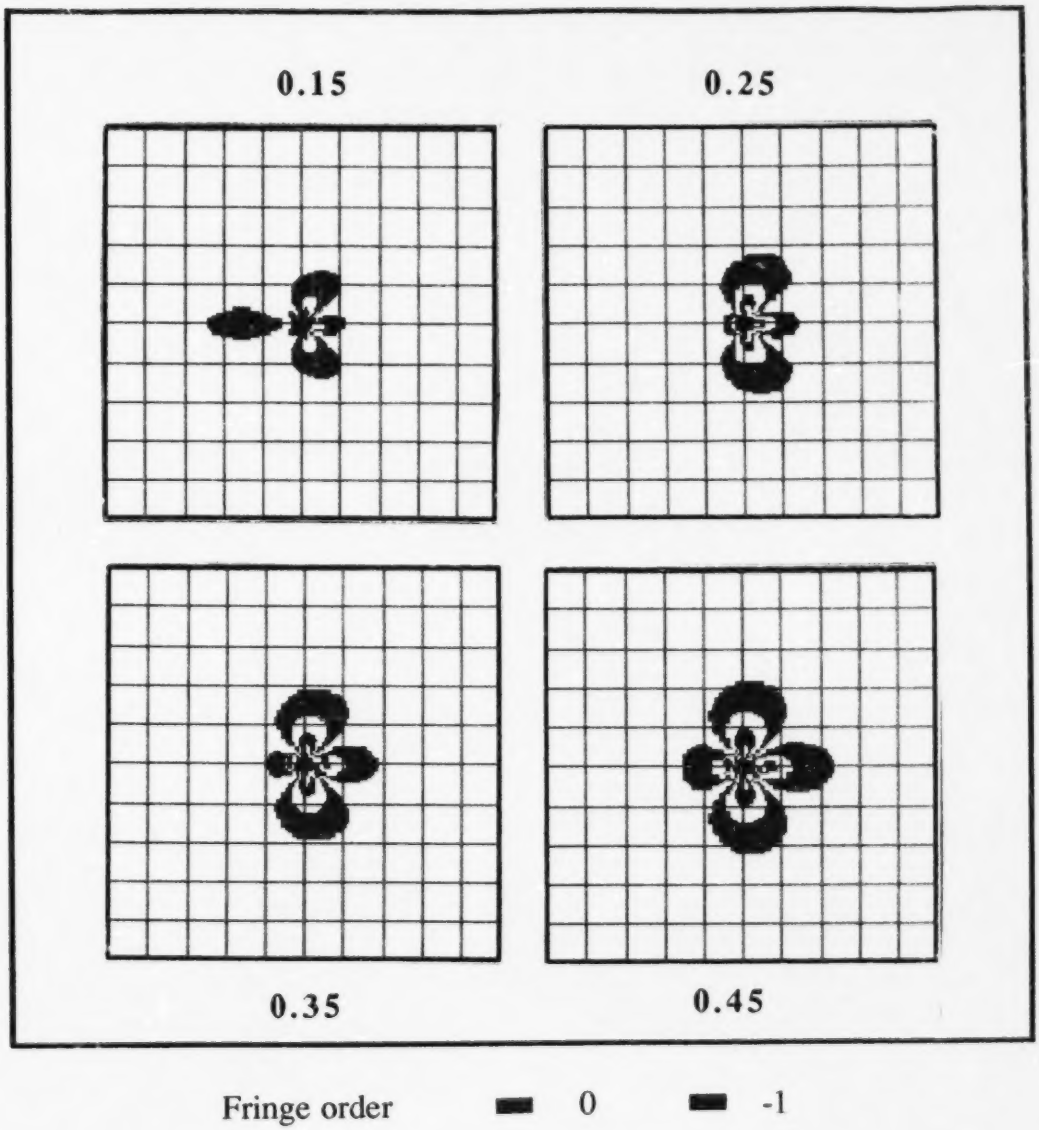

Figure 4-14 Synthetic fringe patterns for Poisson's ratios equal to 0.15, 0.25, 0.35, and 0.45. The FE model has the hole diameters of 0.5 cm and the hole depths of 2.0 cm and the ratio of applied stress to Young's modulus of 1.0 MPa/GPa. The fringe patterns are shown in an area of 10.0 cm x 10.0 cm with centimetre grids.

Figure 4-12 examines the effect of varying hole depths. Here, we chose cases with hole depths of 0.5 cm, 1.0 cm, 2.0 cm and 4.0 cm (Figure 4-7) to evaluate how the fringe patterns change for hole depth/hole diameter ratios larger than unity. The depth of 0.5 cm, which is considered as a guide-line for stable displacements in the measurement of residual stress from strain gages, is not the limit for obtaining stable holographic fringe patterns here. The change of the fringe pattern is substantial even for hole depths greater than 2.0 cm which is four times the hole diameter. This comparison suggests that the stress-relief hole depth must be considered in the analysis of the fringe patterns.

The fringe patterns showing the effect of increasing the SH/E ratio from the calculations of Figure 4-8 are given in Figure 4-13. The number of visible fringes along the vertical axis increases from one to four with SH/E of 0.5, 1.0, 1.5, and 2.0 MPa/GPa. The changes of the fringe patterns in this study indicate that the SH/E ratio strongly influences the formation of the fringe patterns.

The effect of Poisson's ratio on the fringe patterns is another important consideration in our study. It has a noticeable effect on the synthetic fringe patterns and hence a different interpretation would be arrived at if the value of Poisson's ratio using in the analysis was substantially in error. Figure 4-14 shows the fringe patterns corresponding to the calculations of Figure 4-9 for Poisson's ratios equal to 0.15, 0.25, 0.35, and 0.45. Comparing the fringe pattern of $\upsilon = 0.15$ with that of $\upsilon = 0.45$, the change in the fringe patterns is apparent.

4.5 Comparison of Displacement Models

The finite element analysis supplies a comparative tool for exploration of

potential errors caused by the analytic plate and infinite depth hole models in calculating the stress-relief displacement field. In the following, we will discuss the possible sources of error for these two analytic models.

As noted in the background sections, there are two possible inadequacies for these analytic models. One is the assumption of plane stress and the other is the geometry of the modelled stress-relief hole.

As regards the assumption of plane stress, Sternberg and Sadowsky (1949) examined the inadequacy in the stress solution for a cylindrical hole in an infinite plate of arbitrary thickness (Figure 4-15) in which the x- and y-axes are parallel to the principal stress directions and the boundary conditions are

$$\begin{aligned}
&\sigma_z = \tau_{zr} = \tau_{z\theta} = 0 \quad \text{on } z = \pm c \text{ (surfaces of plate)} \\
&\sigma_r = \tau_{r\theta} = \tau_{rz} = 0 \quad \text{on } r = a \text{ wall of hole} \\
&\sigma_x = \sigma_1, \sigma_y = \sigma_2, \tau_{xy} = 0 \quad \text{at infinity} \\
&\sigma_z = \tau_{rz} = \tau_{\theta z} = 0 \quad \text{at infinity.}
\end{aligned} \tag{4.2}$$

For a hole radius a=1 and the principle stresses $\sigma_1 = -\sigma_2 = 1$, the plane-stress solution is

$$\sigma_r = \left[1 - \frac{4}{r^2} + \frac{3}{r^3} - \frac{4\nu\,(c^2 - 3z^2)}{(1+\nu)\,r^4}\right]\cos 2\theta$$

$$\sigma_\theta = \left[-1 - \frac{3}{r^4} - \frac{4\nu\,(c^2 - 3z^2)}{(1+\nu)\,r^4}\right]\cos 2\theta,$$

$$\tau_{r\theta} = \left[-1 - \frac{2}{r^2} + \frac{3}{r^4} \frac{4\nu\,(c^2 - 3z^2)}{(1+\nu)\,r^4}\right]\sin 2\theta,$$

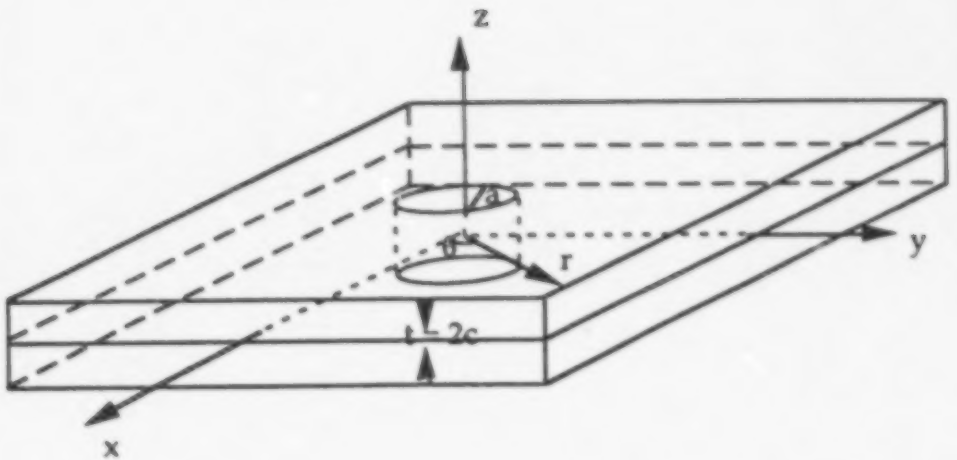

Figure 4-15 Infinite plate of Sternberg and Sadowsky with a circular hole in Cartesian and cylindrical coordinate systems. t is the thickness of the plate and a is the radius of the hole.

$$\sigma_z = \tau_{\theta z} = \tau_{zr} = 0. \qquad (4.3)$$

Apparently, the solutions violate the given boundary conditions in equation 4.2 because the following relations from equation 4.3 differ from equation 4.2.

$$\sigma_z = \tau_{zr} = \tau_{z\theta} = 0 \quad \text{on } z = \pm c \text{ (surfaces of plate)}$$
$$\sigma_r = \frac{4\nu}{1+\nu}(3z^2 - c^2)\cos 2\theta \quad \text{at } r = a = 1 \text{ (wall of hole)}$$
$$\tau_{r\theta} = \frac{4\nu}{1+\nu}(3z^2 - c^2)\sin 2\theta \;,\; \tau_{rz} = 0 \quad \text{at } r = a = 1 \text{ (wall of hole)}$$
$$\sigma_r = \sigma_\theta = \sigma_z = \tau_{r\theta} = \tau_{\theta z} = \tau_{zr} = 0 \quad \text{at infinity}. \qquad (4.4)$$

where the radial stress σ_r and the shear stress $\tau_{r\theta}$ are no longer zero at the wall of the hole (r = a).

For a comparative analysis, a finite element calculation of the plate with a thickness of 4.0 cm and the hole diameter of 0.5 cm at $\upsilon = 0.25$, E = 20.0 GPa subject to principal stresses of σ_1 = 20.0 MPa and σ_2 = 0 MPa was conducted. The model has the size of 30 cm x 30 cm x 4 cm with 1281 nodes and 1040 elements. The result of the stresses on the wall of the hole for θ equal to 0^0 to 90^0 is shown in Figure 4-16. It is apparent that the plate problem really is not a plane stress problem because all stresses are related to the vertical coordinate z. The variation of the stresses with the vertical coordinate occurs principally near the model surface. The vertical stresses are disturbed to the depth approximately equal to the hole diameter. Note that here the radial stress does not equate to zero at the free surface of the hole wall. This is because we use the nodal stresses that are stored per element and then are averaged at a node whenever two or more elements connect to this node. Since the

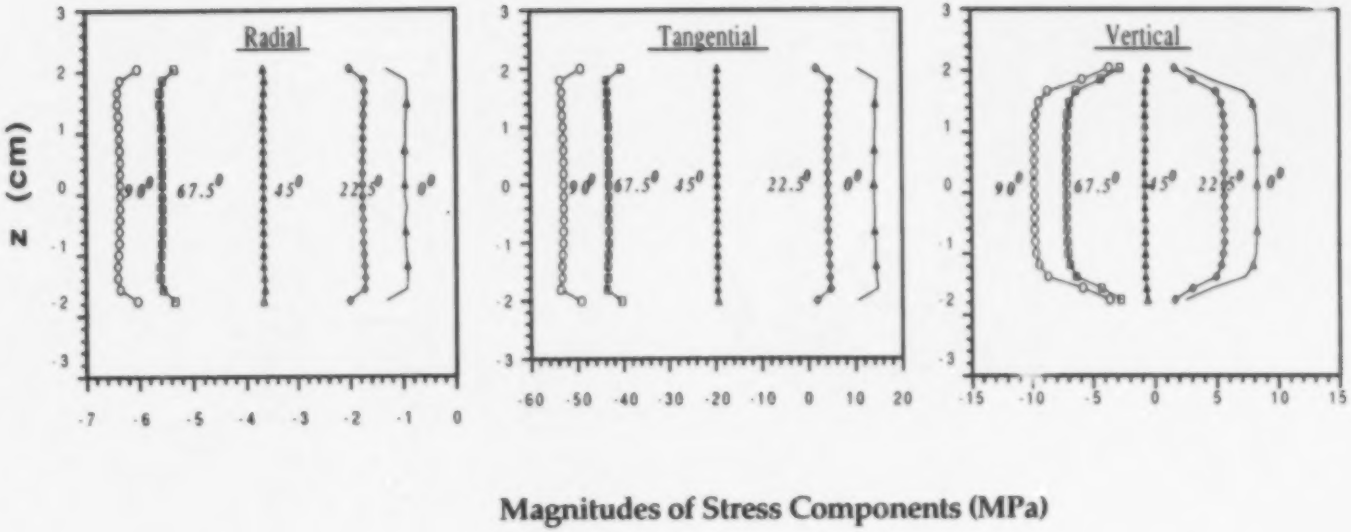

Figure 4-16 Nodal Stresses along the wall of a throughgoing hole (diameter equal to 0.5 cm) of a plate model for FE analysis. The FE model has the dimensions of 30.0 cm x 30.0 cm x 4.0 cm (thickness), and 1782 nodes and 1352 elements. The ratio of the applied stress to Young's modulus used is 1.0 MPa/GPa and Poisson's ratio is 0.25. z equal to 2.0 cm and -2.0 cm are the surfaces of the plate.

elements stresses are not equal to zero, the nodal stresses cannot vanish.

For a further analysis, Figure 4-17 compares four stress-relief displacement models which are the analytic plate model, the analytic infinite depth hole model, the FE plate model with a throughgoing hole discussed above, and the FE model with a finite depth hole discussed in 4.2. The parameters held constant are the hole diameter of 0.5 cm, υ of 0.25 and the SH/E ratio of 1.0 MPa/GPa. Since the modelled hole depth is 2.0 cm, the thicknesses of the analytic plate model and the FE plate model both are 4.0 cm. The calculated radial and tangential displacements are shown in Figure 4-17a and Figure 4-17b, respectively. The infinite depth hole model has the greatest magnitudes whereas the FE model with a finite depth hole has the smallest. In Figure 4-17c, the vertical displacements of the analytic plate model are very large in the vicinity of the hole and are roughly ten times those of the FE models at the edge of the stress-relief hole. This difference will increase with hole depth because the vertical displacement of the analytic plate model increases linearly with the hole depth.

Figure 4-18 gives the fringe patterns corresponding to the displacements of Figure 4-17 for the analytic plate model, the infinite depth hole model and the FE plate model. The fringe pattern corresponding to the FE model with a finite depth hole is shown in Figure 4-11 for a hole diameter of 0.5 cm. Comparing these fringe patterns, the FE plate model (Figure 4-18a) is most similar to the finite element model with a finite depth hole (Figure 4-11), but the fringes along the horizontal axis expand and along the vertical axis shrink. The difference could be a consequence of the hole geometry because one has hole bottom and the other has not. However, the fringe patterns of

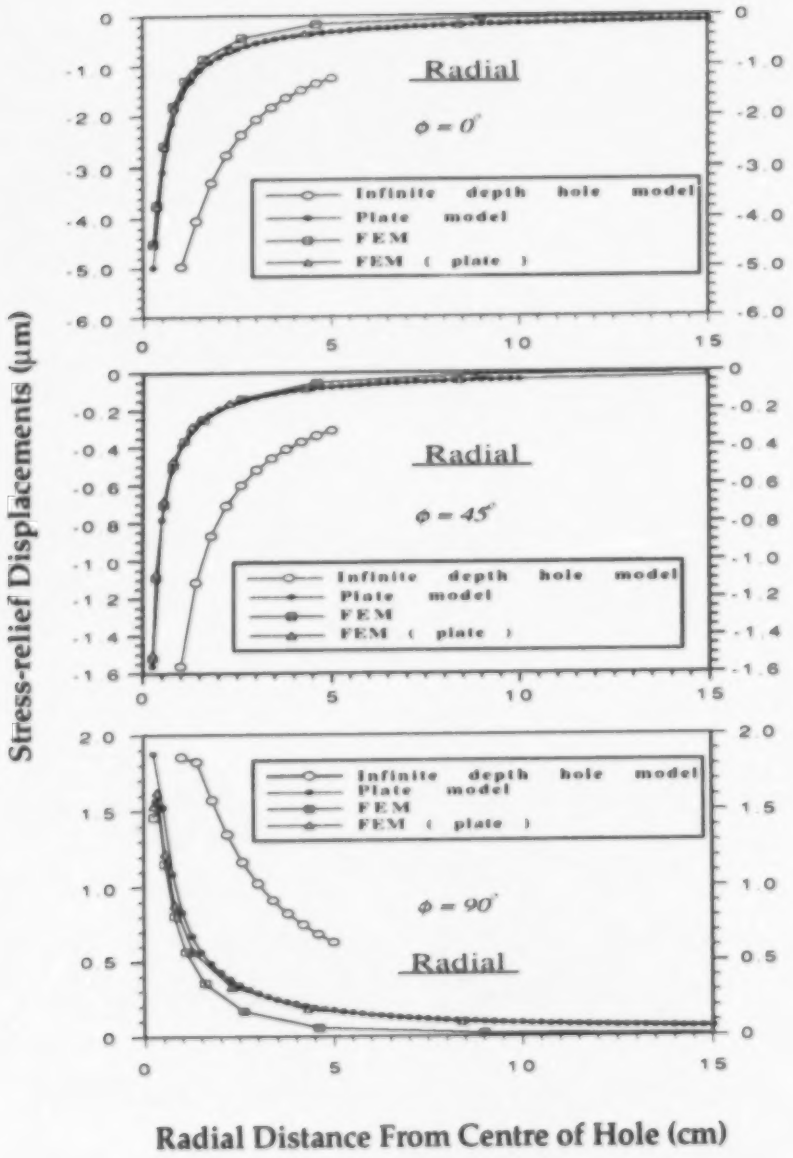

Figure 4-17a Comparison of the radial surface stress-relief displacements of the infinite depth hole model, the plate model, the FE model with a throughgoing hole, and the FE model with a finite depth hole for a stress-relief hole diameter of 0.5 cm.

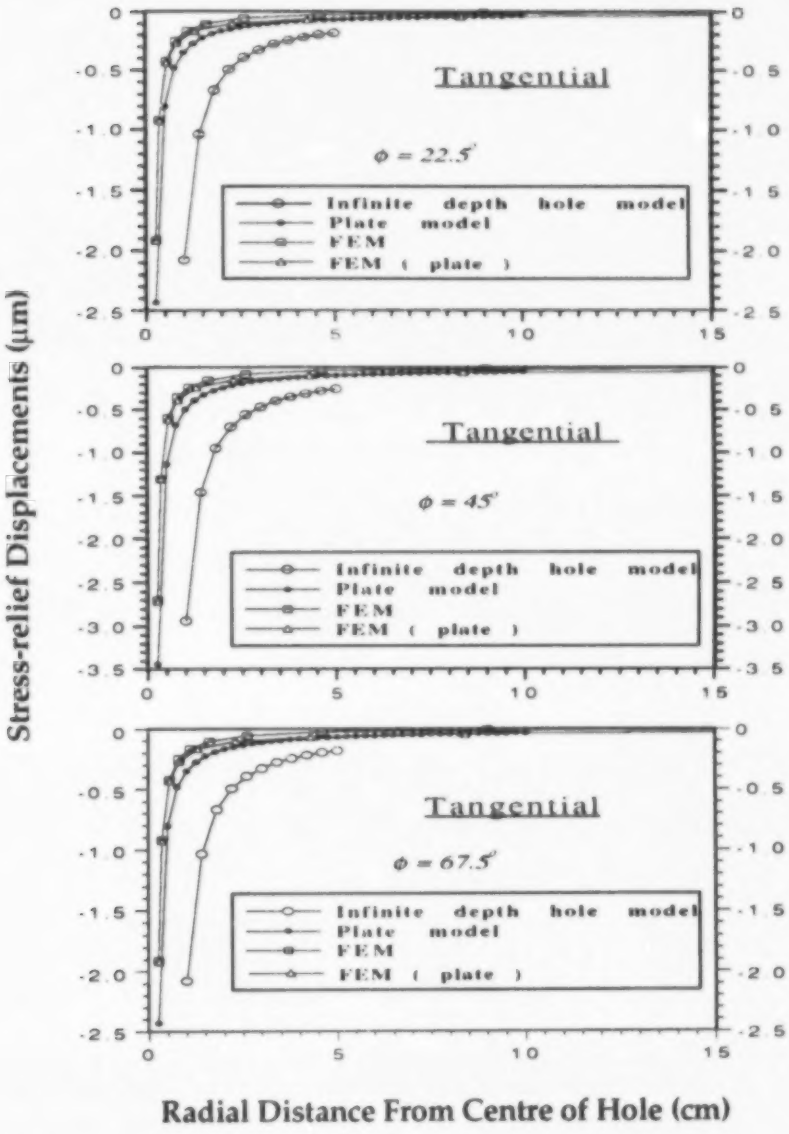

Figure 4-17b Comparison of the tangential stress-relief displacements of the infinite depth hole model, the plate model, the FE model with a throughgoing hole and the FE model with finite depth hole for a stress-relief hole diameter of 0.5 cm.

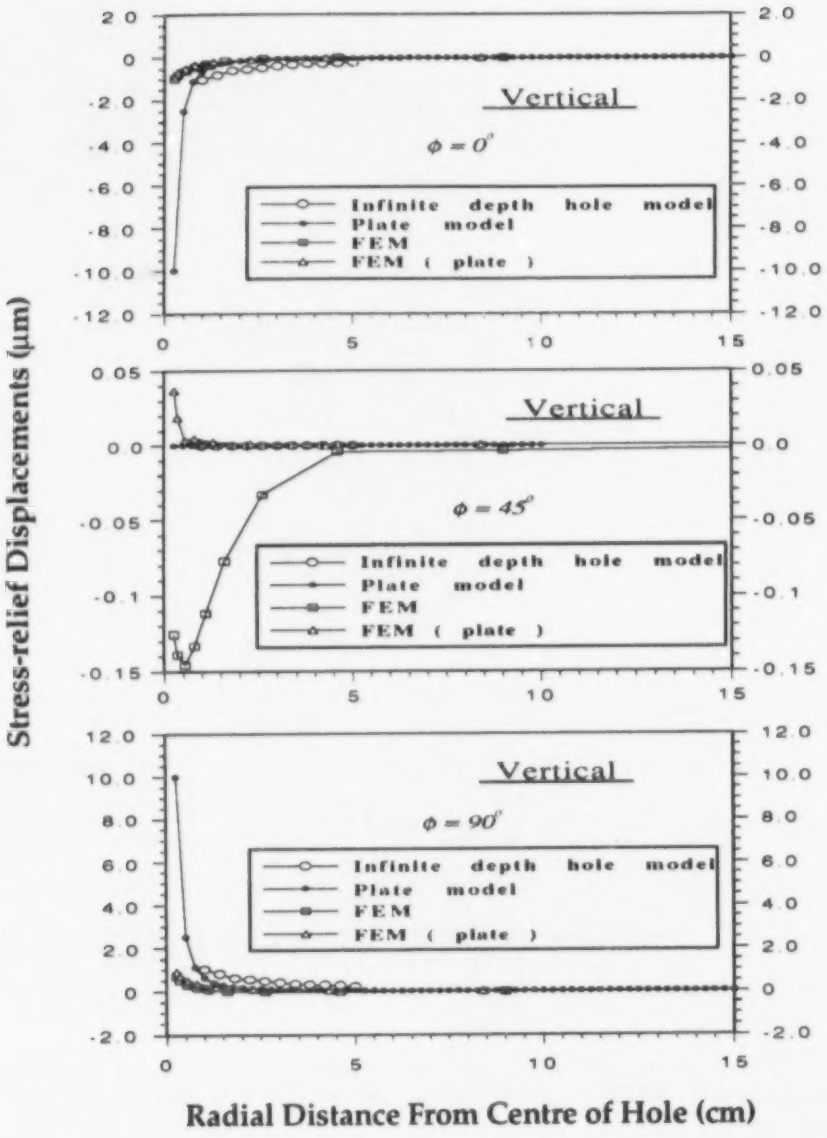

Figure 4-17c Comparison of the vertical surface stress-relief displacements of the infinite depth hole model, the plate model, the FE model with throughgoing hole, and the FE model with finite depth hole for a stress-relief hole diameter of 0.5 cm.

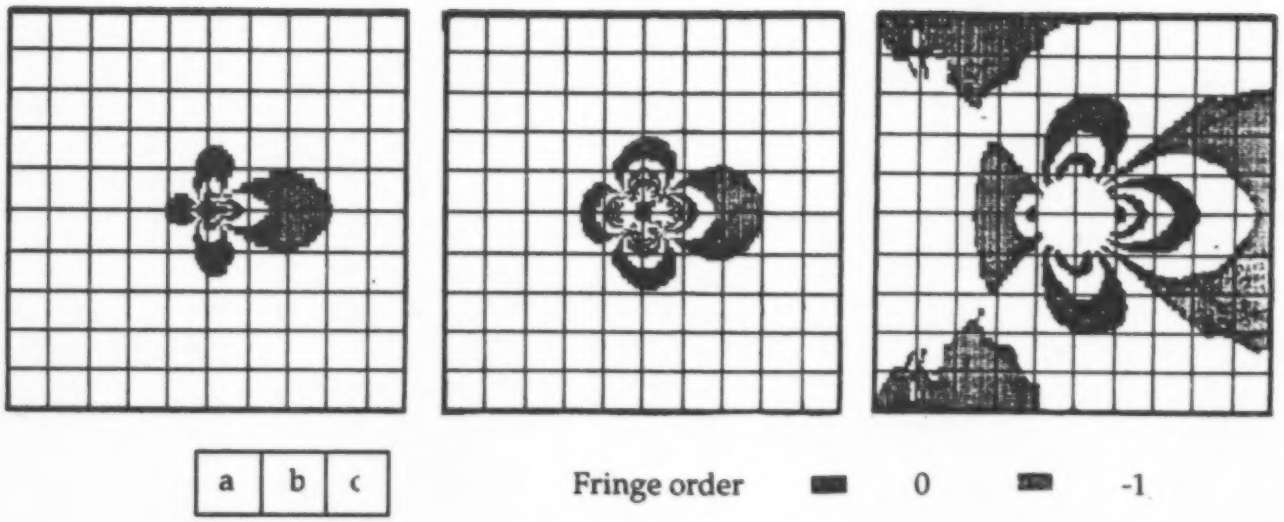

Figure 4-18 Comparison of the synthetic fringe patterns of the FE model with throughgoing hole (a), the analytic plate model (b), and the infinite depth hole model (c) with a stress-relief hole diameter of 0.5 cm. The thickness of the FE model and the plate model is 4.0 cm, the ratio SH/E is 1.0 MPa/GPa, and Poission ratio is 0.25. The fringe pattern of the FE analysis for a finite depth hole (2.0 cm) is shown in Figure 4-11. All fringe patterns are shown in an area of 10 cm x 10 cm with centimetre grids. Note that no fringes are shown in the 2.0 cm diameter region for the infinite depth hole model because the solution of Smither et al.(1991) is not provideed.

the analytic plate model (Figure 4-18b) and infinite depth hole model (Figure 4-18c) are very different. The expansion of the fringes along the horizontal axis is shown. The dark fringes of the infinite depth hole model almost cover the entire 10 cm x 10 cm area while the other models only cover a small part of the area. Note that no fringes are seen in the 2.0 cm diameter region for the infinite depth hole model because the solution of Smither et al. (1991) is not provided in this region.

Discussions related to the above comparison are, admittedly, somewhat qualitative. However, as may be seen from the differing fringe patterns, if taken in reverse the models would yield substantially different stress magnitudes. That is, what stress magnitudes would be determined using different displacement models for a nearly equivalent displacement field or fringe pattern?

A surface trend analysis (Unwin, 1969) is used to quantitatively compare the stress applied to two analytic models with respect to that of the FE model with a finite depth hole. The ratio RSS (Ratio of Sum of Squares) is expressed as a percentage or a decimal of the corrected sum of squares of the displacements U_f of the FE model to that of the displacements U_{anal} from the analytic models. That is

$$RSS = \frac{\sum_{i=1}^{n}\sum_{j=1}^{m} U_{f_{ij}}^2 - \left(\sum_{i=1}^{n}\sum_{j=1}^{m} U_{f_{ij}}\right)^2/(NxM)}{\sum_{i=1}^{n}\sum_{j=1}^{m} U_{anal_{ij}}^2 - \left(\sum_{i=1}^{n}\sum_{j=1}^{m} U_{anal_{ij}}\right)^2/(NxM)}, \qquad (4.5)$$

where N and M are the number of data points in the x and y directions,

respectively. This method can be used to obtain the equivalent coefficient of correlation, √RSS, directly. If √RSS were to equate to unity the fit of two groups of the displacement data from different displacement models is considered the best. The present computational procedure consists of varying the stress applied to the analytic models until a value of √RSS closest to 1.0 is reached whereupon the displacement field of an analytic model is considered to best approximate that of the FE model. At this point the ratio of the stress applied to an analytic model to the stress applied to the FE model is determined. The calculations were conducted both using only single displacement components and using all displacement components. The results are listed in Table 4-2.

Table 4-2 The Ratios of Stresses (SH) Between Various Displacement Models

Model	Single displacement component			All displacement components
	Radial	Tangential	Vertical	
FEM*	1.0	1.0	1.0	1.0
Plate Model	0.9	0.78	0.12	0.47
Revised Plate Model**	0.9	0.78	0.47	0.84
Infinite Depth Hole Model	0.26	0.12	0.22	0.25

* with a finite depth hole.
** ignore the displacements within 1.0 cm radial distance.

If we compare the calculations for all the displacement components of the

analytic plate model to the FE model, the applied stress ratio is 0.47. That suggests that the stress magnitude obtained from the plate model would be less than half of that from the FE model. This ratio rises up to 0.84 when the data points within radial distance 1.0 cm from the centre of the hole are ignored. The infinite depth hole model is in even poorer agreement with the FE model because the ratio is only 0.25.

If the displacement components are considered separately, the radial displacements of the plate model has the highest stress ratio of 0.9. However, the ratio of the infinite depth hole model are still low at only 0.26. For the tangential displacement, the infinite depth hole model is again in poorest agreement at 0.12. For the vertical displacements, the plate model has the lowest ratio of 0.12. When the data points within diameter of 1.0 cm are deleted, the ratio reaches up to 0.47 which still low.

From the above comparison of the stress ratios, the analytic plate model may better approximate, in a statistical sense, the finite element model if we ignored the displacements close to the edge of the stress-relief hole. However, the infinite depth hole model may not provide a proper stress-relief displacement field to obtain the precise stress magnitude.

Chapter 5 Laboratory Experiment

In earlier sections, we contrasted the two existing analytic displacement models with the 3-D finite element model in order to determine possible sources of error of the analytic models. However, both analytic and numerical techniques remain suspect until they are experimentally verified. In this chapter, we will discuss a series of laboratory holographic experiments which test the validity of the finite element modelling. This section includes descriptions of the experimental set-up, the calibration of the applied stress measurement system, the recognition of experimental noise, and most importantly, the comparison of the fringe patterns from the resulting holograms to those produced from the finite element calculations.

5.1 Set-up and Calibration

The holographic experiment set-up consists of three components: the optical system, the mechanical system and the stress measurement system. Because local vibrations are potentially deleterious to data quality, the set-up is installed on a 1.2 m x 2.42 m vibration-isolation steel honeycomb platform.

Figure 5.1 shows the configuration of the optical system. A He-Ne laser with maximum output of 10 mW at a wave length of 632.8 nm is the source of coherent light. This laser beam is separated into reference and object beams by a beam splitter which here is only a simple piece of glass. The reference beam is reflected at mirror 1 and then propagates through a lens to directly illuminate the holographic film. The object beam is reflected at mirror 2 and

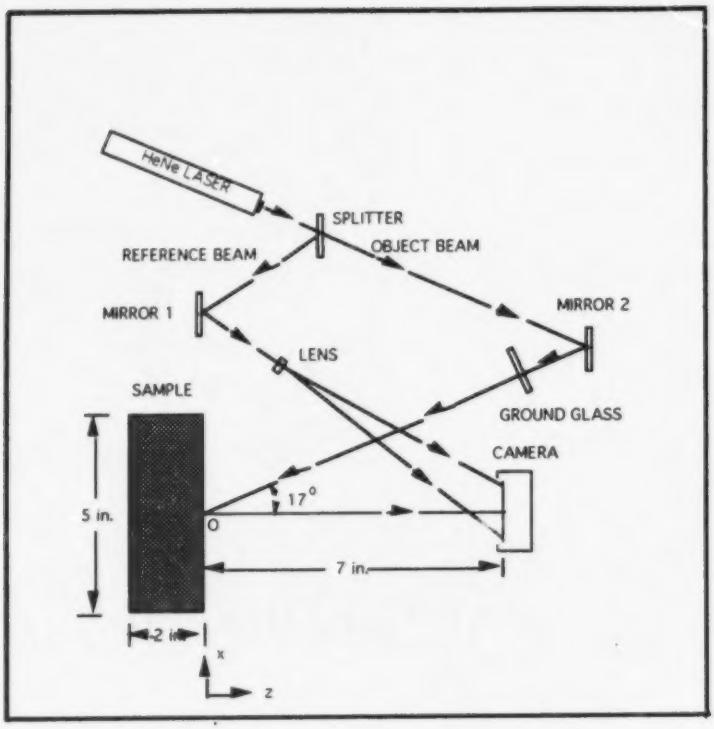

Figure 5-1 Configuration of double-exposure holographic optical system. A HeNe laser with maximum output 10 mW at wave length 632.8 nm is used for the source. The laser light is separated into reference and and object beams by a splitter. The reference beam is reflected at mirror 1 and then passes through the lens to illuminate the holographic film. The object beam is reflected at mirror 2 and then passes through a ground glass which diffuses the beam to illuminate the surface of the sample and then is reflected to the holographic film.

then passes through a ground glass which diffuses the beam to illuminate the surface of the sample. This light then is scattered (nonspecular reflection) back to the holographic film. The distance between the sample and the holographic film is 17.8 cm (7.0 in) and the angle α as shown is 17^{0}. The origin of the coordinate system about this optical system is located at O as shown in Figure 5-1 which is the centre of the block surface and also coincides with the axis of the stress-relief hole. The axis of the stress-relief hole, the centre of the holographic film, and the source point S of the object beam are all contained within the x-z plane. The coordinates of these points are given in Table 5-1.

Table 5-1

	x (cm)	y (cm)	z (cm)
Source point S	9.7	0.0	23.5
Centre of sample surface O	0.0	0.0	0.0
Centre of holographic film	0.0	0.0	17.85

The mechanical part of the experimental configuration consists of a manual hydraulic pressure pump of 69 MPa (10 kpsi), a manual pressure generator of 207 MPa (30 kpsi), a hydraulic pressure gauge, and a steel stressing frame which holds the sample (Figure 5-2). When a sample is placed into the steel frame, the pump first applies an approximate pressure via two hydraulic rams and then the pressure is adjusted to the desired value by the pressure generator.

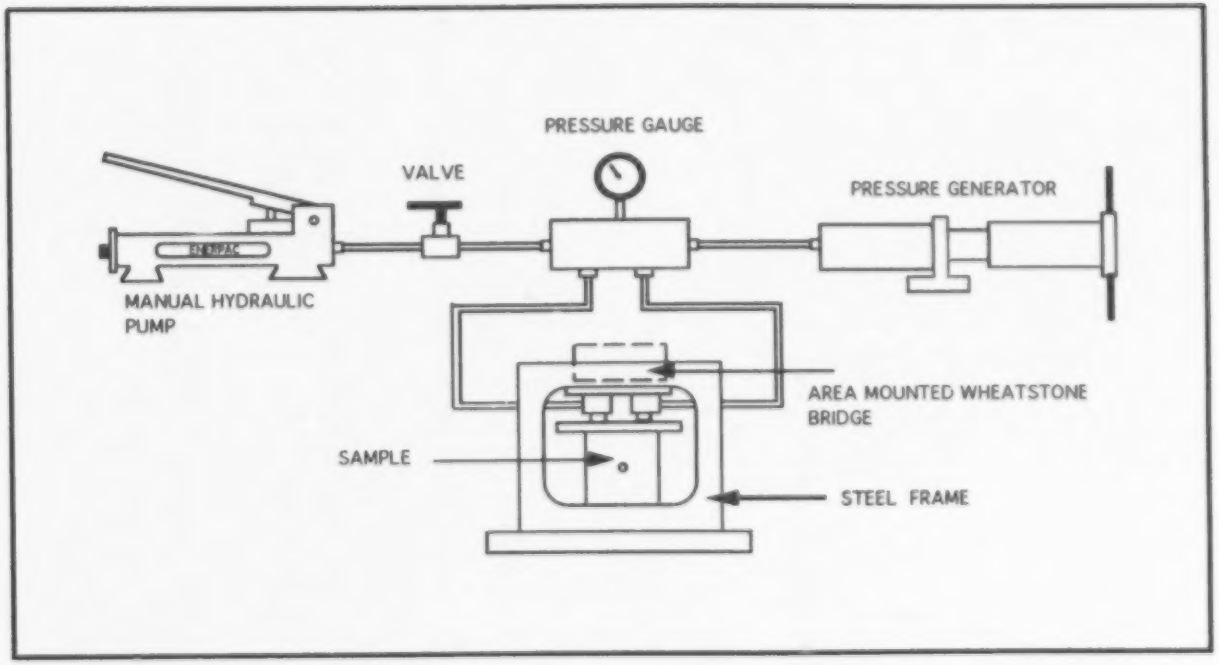

Figure 5-2 Schemtic of mechanical system for applying an uniaxial stress to a block sample. The system consists of a manual hydraulic pump of 69MPa, a pressure generator of 207 MPa, a hydraulic pressure gauge and a steel frame for placing sample. A Wheatstone bridge used for measuring stress applied to a sample is mounted on the top of the steel frame.

The hydraulic pressure gauge used is of insufficient accuracy to measure pressure to the degree of sensitivity required in the tests. Consequently, a Wheatstone bridge consisting of four strain gages of type CEA-06-500UW-120 with size of 15 mm x 5 mm and resistance of 120±0.3% Ohms (at 24°C) is mounted on the top of the steel frame. This bridge allows the stress applied on a sample to be measured by the output voltage resulting from the deformation of the steel frame.

This force measurement system requires calibration; that is, the relationship between the output voltage of the mounted Wheatstone bridge on the steel frame and the applied force is required. To calibrate, a load cell consisting of four strain gauges in a Wheatstone bridge arrangement mounted on a steel pipe (outer diameter: 5.5 cm, internal diameter: 5.0 cm and height: 4 cm) was constructed. The response of this load cell to force under an activation voltage of 7.0 volts was determined by using a standard testing machine in the structure engineering laboratory of the Department of Civil Engineering at the University of Alberta to obtain a linear relation of the applied force to the output voltage. The calibrated load cell was then placed into the steel frame in our laboratory, and the responses of the load cell and the steel frame were simultaneously recorded under the same activation voltage as used in the standard testing machine (Figure 5-3). The response of the load cell is represented as

$$y = -0.2174 + 0.07046\ x \qquad (5.1)$$

with the correlation coefficient R = 0.998 and the standard error S_δ = 0.097.

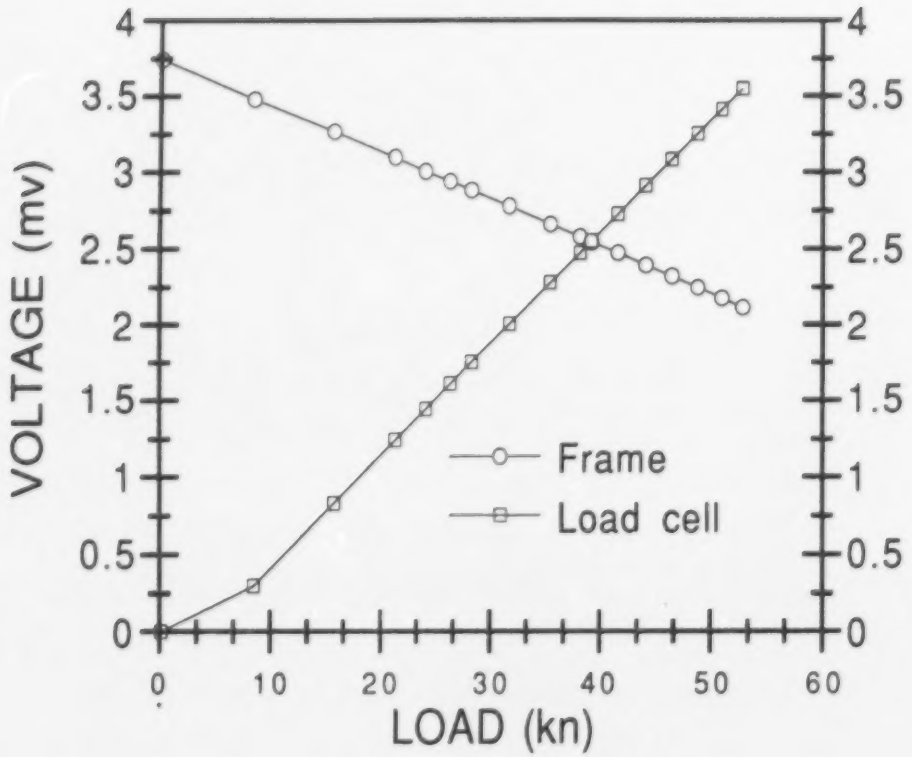

Figure 5-3 Output voltages vs load applied to a sample for the Wheatstone bridge mounted on the steel frame and a load cell under an activation voltage of 7.0 volts.

The response of the steel frame is

$$y = 3.7496 - 0.03075\ x \qquad (5.2)$$

with the correlation coefficient R = 0.999 and the standard error S_δ = 0.0076. Here, y represents the output voltage of Wheatstone bridge in millivolts and x represents the load applied to a sample in kN. Comparison of these two linear relationships thus allows determination of the force applied to a sample. The uniaxial stress applied to the sample then may be obtained by giving the area of a surface over which the force is applied. In Figure 5-3, the curve labelled "frame" is used to measure the applied force in our experiments. For the response of the load cell, the beginning part of the curve is not linear. This nonlinearity is not understood but it and the linear part of the curve are repeatable. Since the forces applied in the experiments are above the range where this nonlinearity appears, the nonlinear part is ignored in the calibration fit of equation 5.2.

5.2 Finite Element Models

Blocks of plexiglass with dimension of 12.7 cm x 12.7 cm x 5.08 cm (5 in x 5 in x 2 in) are used in the experiments. Strain tests on two cylindrical plexiglass samples in the steel frame show that the plexiglass has a Poisson's ratio of 0.4 ± 0.01 and Young's modulus of 3.0 ± 0.05 GPa. The geometry of the finite element model of the plexiglass block is the same as shown in Figure 4-3 except the dimensions and the boundary conditions. There are 1452 nodes

and 1092 elements in this finite element model.

The boundary conditions on the plexiglass block are that the top and bottom surfaces as shown in Figure 5-2 are constrained by friction because they contact the stressing frame as the force is applied through them. Because the distribution of friction on these two surfaces is unknown, calculations were conducted for two extreme cases of either infinite friction or nonexistent friction. The real distribution of friction on these two surfaces may be considered to lie between these two extreme cases. The remaining boundaries of the block plexiglass sample are free of constraints.

The finite element model is only one quarter of the whole plexiglass block; these two extreme friction cases were tested by constructing the boundary conditions as follows:

The case of infinite friction is modelled by giving zero in-surface nodal displacements (in the x and z directions) on the boundary over which the force is applied (Figure 4-3) regardless of the existence of the stress-relief hole.

The case of zero friction is modelled by two different methods. The first method is to conduct a calculation without a stress-relief hole and free of constraints on the applied force boundary. Then, the in-surface nodal displacements obtained at the boundary are input as the displacement boundary condition for the calculation with a stress-relief hole. This process maintains the same in-surface displacements on the applied force boundary whether there is or there is not a stress-relief hole.

The second zero friction model was calculated by keeping the applied force boundary free of constraints in the calculations both with and without a stress-relief hole. A characteristic of this modelling is that there are no

anomalous boundary effect displacements in the calculation without a stress-relief hole; however, the displacements appear due to the loss of the symmetry when a stress-relief hole is modelled.

For convenience, we call these three models, model 1, model 2, and model 3, respectively.

Figure 5-4 shows the stress-relief displacements resulting from these three models for a sample subject to an uniaxial stress of 6.0 MPa and for a stress-relief hole having a diameter of 0.5 cm and a depth of 1.0 cm. The radial and tangential displacements for these models are similar. The vertical displacements of model 3, however, differ from those of model 1 and 2. This is a consequence of the boundary effect displacements inherent to model 3.

Synthetic fringe patterns produced from these three models are compared in Figure 5-5. The fringe pattern of model 1 differs somewhat from that of model 2. However, the fringe pattern of model 3 is substantially different from the other two. The large bending of model 3 is illustrated by the existence of the fringes with order -2, -1, 0, 1, and 2 in the vertical direction from the top or bottom boundary towards the stress-relief hole. Note that the uniaxial stress is in the vertical direction in the fringe pattern.

Based on the comparison of the displacements and the fringe patterns above, model 1 was chosen for use in further calculations due to the large bending in model 3 and the similarity of model 1 and model 2.

In order to illustrate the weight of the different displacement components in the formation of the fringe patterns, the synthetic fringe patterns which separately employ each of three displacement components from the calculation of model 1 of Figure 5-5 are plotted in Figure 5-6. This figure

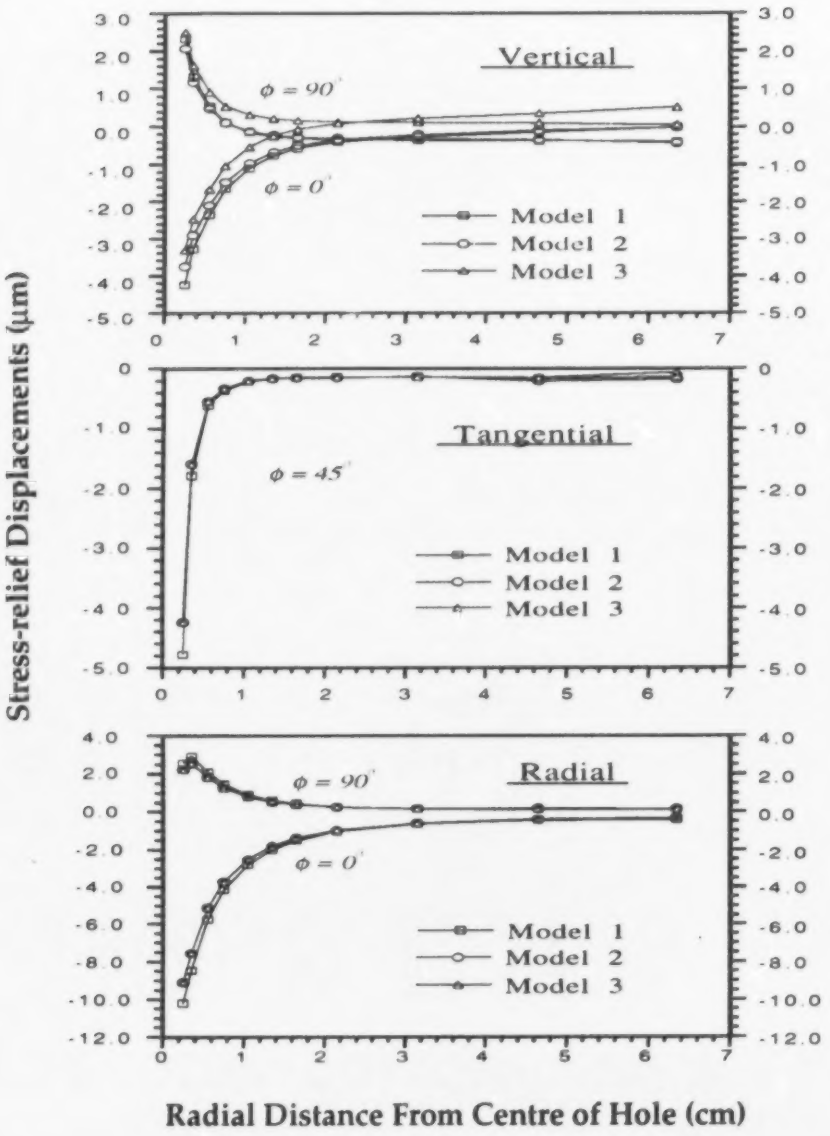

Figure 5-4 Stress-relief displacements of three FE models with different boundary condition for a plexiglass sample under an uniaxial stress of 6.0 MPa. The size of the stress-relief hole is diameter of 0.5 cm and depth of 1.0 cm.

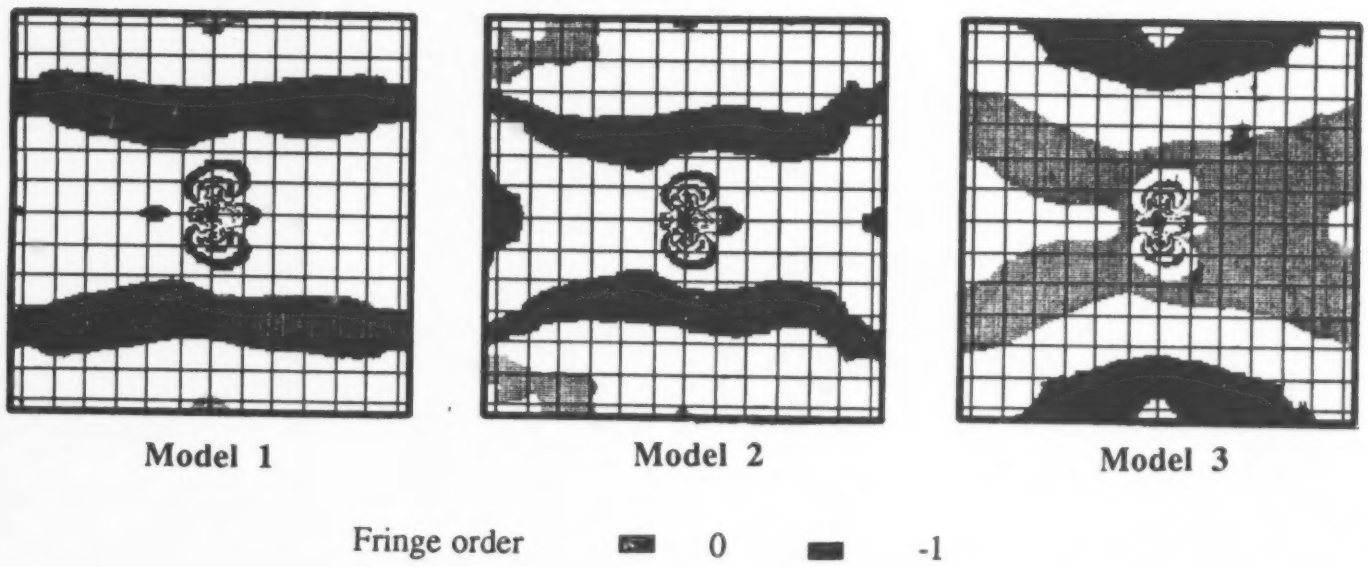

Figure 5-5 Synthetic fringe patterns of three FE models of plexiglass sample with an applied uniaxial stress in the vertical direction. The boundary over which the force is applied has the characteristic: model1: friction equal to infinity; model 2: friction equal to zero but the obtained in-plane displacements of the boundary in the calculation without a stress-relief hole is used to construct a new boundary condition for the calculation with a stress-relief hole; model 3: friction equal to zero and the boundary is of free constraint for both calculations with and without a stress-relief hole. The fringe patterns are shown in a 12.7 cm x 12.7 cm area with centimetre grids.

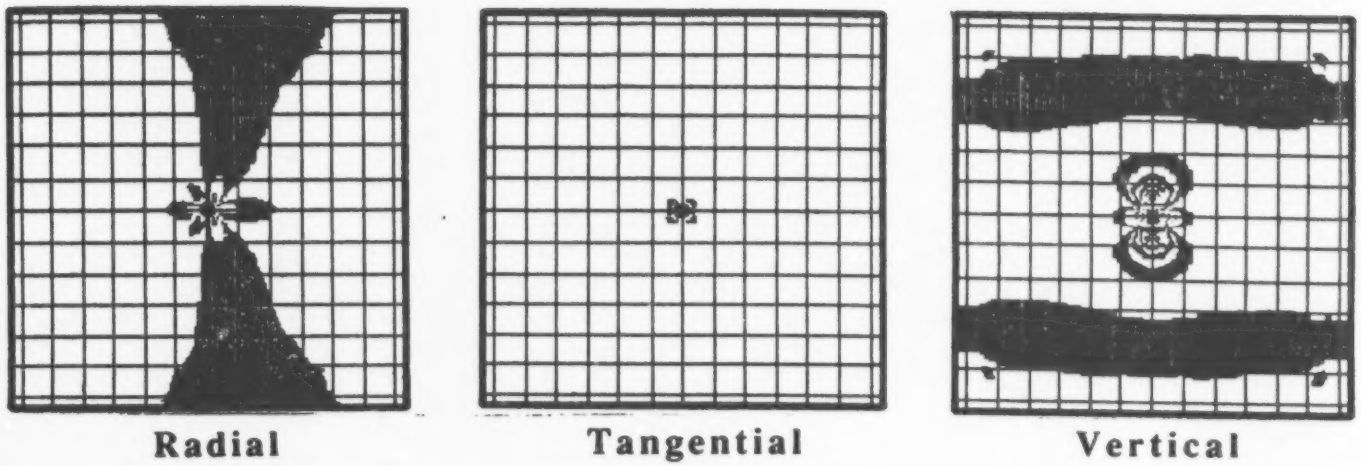

Figure 5-6 Synthetic fringe patterns of three stress-relief displacement components of FE model 1 with a stress-relief hole diameter of 0.5 cm and a depth of 1.0 cm and an uniaxial stress of 6.0 MPa. The fringe patterns are shown in a 12.7 cm x 12.7 cm area with centimetre grids.

shows that the optical system used is most sensitive to the out-of-plane displacements as this displacement component forms many more fringes than the other two in-plane components. The tangential component contributes little to the formation of the fringes because only a very small area near the stress-relief hole is covered by dark fringes with order -1; the remaining area has the bright fringe of order -0.5 that represents zero displacements

5.3 Experiments

The primary objective of the laboratory experiments here is to test the feasibility of the 3-D finite element method in the determination of stress-relief displacements. If the finite element method satisfactorily predicts the stress relief displacements observed under controlled laboratory conditions, then it may be applicable to in situ stress measurements. A series of laboratory experiments using plexiglass blocks were conducted with the experimental parameters listed in Table 5-2. In these experiments, the surfaces of the plexiglass blocks were painted with a white flat paint for the purpose of reflecting light. A centimetre net was drawn on the surfaces of the blocks as a reference to determine the position of fringes.

The analysis of the experimental results are based on the comparison of the synthetic fringe patterns from the finite element calculations to the observed fringe patterns. This analysis is, at present, only semiquantitative in that the fringe patterns are compared visually with respect to the centimetre grid scale. Deficiencies of this approach are that possible bias may be

Table 5-2 Holographic Experiment Parameters

Type of experiment	Hole diameter (cm)	Hole depth (cm)	Applied stress (MPa)	Time between exposure (hour)
Experiments with variable hole depth	0.5±0.05	0.5±0.05	6.0±0.21	3.0
	0.5±0.05	1.0±0.05	6.0±0.21	2.5
	0.5±0.05	2.0±0.05	6.0±0.21	2.5
Experiments with variable applied stress	0.5±0.05	1.0±0.05	4.0±0.21	3.0
	0.5±0.05	1.0±0.05	6.0±0.21	2.5
	0.5±0.05	1.0±0.05	8.0±0.21	1.0
Experiments on thermal effects	0.5±0.05	1.0±0.05	6.0±0.21	5 min.
	0.5±0.05	1.0±0.05	6.0±0.21	1.0*

* The first exposure immediately after drilling.

introduced via the observer's perception of a fringe in the photographs.

In the experiments, the diameter of the stress-relief hole needs to be sufficiently small in order that the fringe pattern is constrained to a limited area and to limit the potential for effects between the top and bottom surface of the plexiglass and the stress-relief hole. Based on the calculations of Chapter 4, a stress-relief hole diameter of 0.5 cm was chosen. The maximum depth of the stress-relief hole was chosen as 2.0 cm. This depth is about 40% the thickness of the test plexiglass block.

Since the material elastic properties have been determined and the diameter of the stress-relief hole is fixed, the only variables in the experiments are the depth of the stress-relief hole and the magnitude of the applied uniaxial stress. Hence, two series of experiments, in which one of these two variables was varied, were conducted.

The first series of tests consisted of three experiments in which the depths of the stress-relief hole were 0.5 cm, 1.0 cm, and 2.0 cm with the blocks subject to an applied stress of 6.0 MPa. These depths are equal to, double and four times the diameter of the hole, respectively. They were chosen to determine whether the fringe patterns stabilize with increasing hole depth.

Figure 5-7a shows the synthetic and observed fringe patterns for the hole depth equal to 0.5 cm. Note that this depth is considered to be the stabilization depth of the induced stress-relief strain in the residual stress measurements by strain gages as described earlier. Comparing these two fringe patterns, the vertical lobes are similar. In particular, the lower lobe matches very well in terms of shape and position. One major difference between the observed and the synthetic fringe patterns, however, is that a few roughly

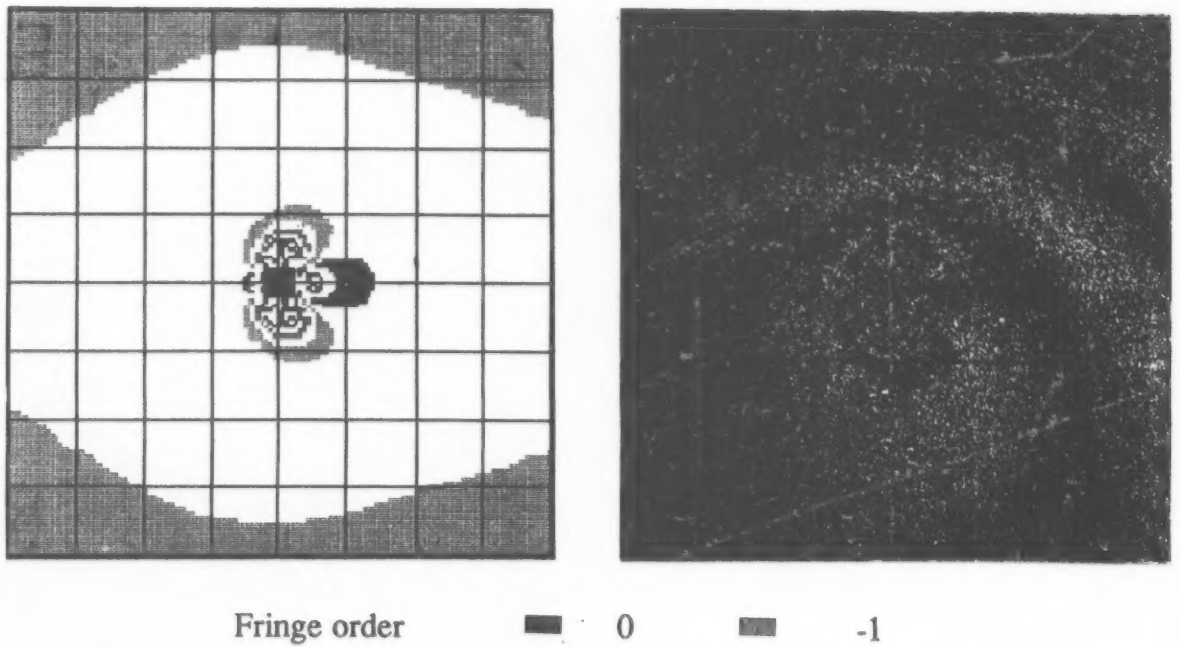

Figure 5-7a Synthetic and observed fringe patterns of the plexiglass sample with a stress-relief hole diameter of 0.5 cm and a depth of 0.5 cm, and an uniaxial stress of 6.0 MPa in the vertical direction. The fringe patterns are shown in a 8.0 cm x 8.0 cm area with centimetre grids. In the synthetic fringe pattern, the dark fringes have the orders -1, -1, 0, 1, and 2 from the top or bottom boundary towards the stress-relief hole, and -2, -3 from the right or left boundary towards the stress-relief hole.

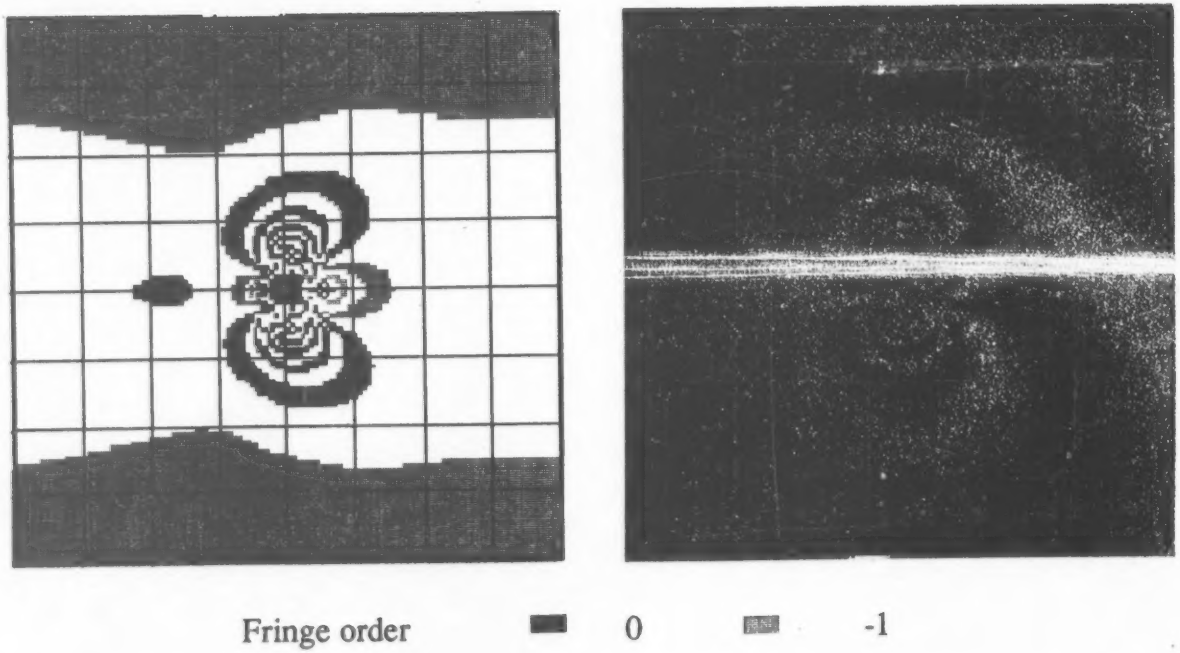

Figure 5-7b Synthetic and observed fringe patterns of the plexiglass sample with a stress-relief hole diameter of 0.5 cm and a depth of 1.0 cm, and an uniaxial stress of 6.0 MPa in the vertical direction. The fringe patterns are shown in a 8.0 cm x 8.0 cm area with centimetre grids. In the synthetic fringe pattern, the dark fringes have the orders 0, 1, 2, 3, 4, and 5 from the top or bottom boundary towards the stress-relief hole, and 0, -1, and -2 from the right or left boundary towards the stress-relief hole.

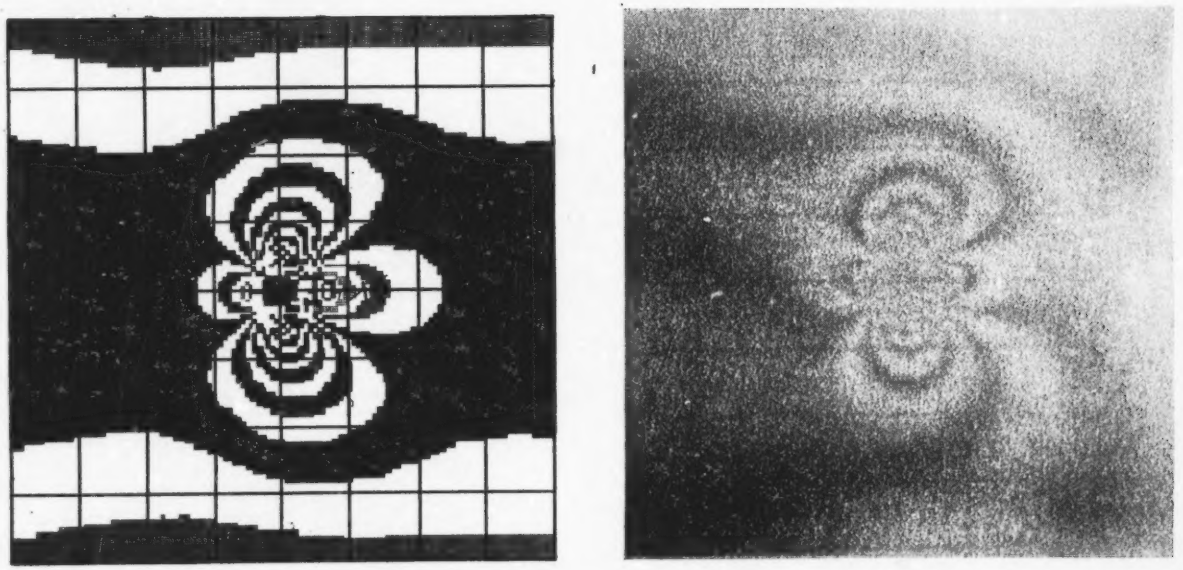

Figure 5-7c Synthetic and observed fringe patterns with a stress-relief hole of diameter of 0.5 cm and a depth of 2.0 cm, and an uniaxial stress of 6.0 MPa in the vertical direction. The fringe patterns are shown in a 8.0 cm x 8.0 cm area with centimetre grids. In the synthetic fringe pattern, the dark fringes have the orders 0, 1, 2, 3, 4, 5, and 6 from the top or bottom boundary towards the stress-relief hole, and 1, 0, -1, -2, and -3 from the right or left boundary towards the stress-relief hole.

circular fringes appear in the upper part of the observed fringe pattern. Based on the analysis of Schmitt (1987), these fringe are likely due to a translation in the z direction away from surface of the sample. Also, it is possible that these fringes are caused by the thermal expansion due to the drilling of the stress-relief hole.

Figure 5-7b shows the fringe patterns of the experiment and the finite element calculation for the hole depth of 1.0 cm. Here, the vertical lobes of the two fringe patterns are in very good agreement. Unfortunately, the horizontal lobes are obscured by scattered light during reconstruction because the film was scratched.

Figure 5-7c shows the fringe patterns of experiment and finite element calculation for the hole depth of 2.0 cm. The agreement between the observed and the synthetic fringe patterns is considered to be excellent in this of experiment.

The second series of experiments were conducted with hole diameters of 0.5 cm and hole depths of 1.0 cm under increasing uniaxial stress magnitude. Figure 5-8a shows the synthetic and observed fringe patterns under an applied stress of 4.0 MPa. The lobes of both fringe patterns are consistent with the exception that the zero order fringe in the synthetic fringe pattern covers a larger area. In the observed fringe pattern, the white streaks caused by a scratch on the film again obscure the horizontal lobes.

Figure 5-8b shows the synthetic and observed fringe patterns under an applied uniaxial stress of 8.0 MPa. Both fringe patterns also are consistent. However, the horizontal lobes of the observed fringe pattern do not appear because the time duration between exposures is only one hour. This time

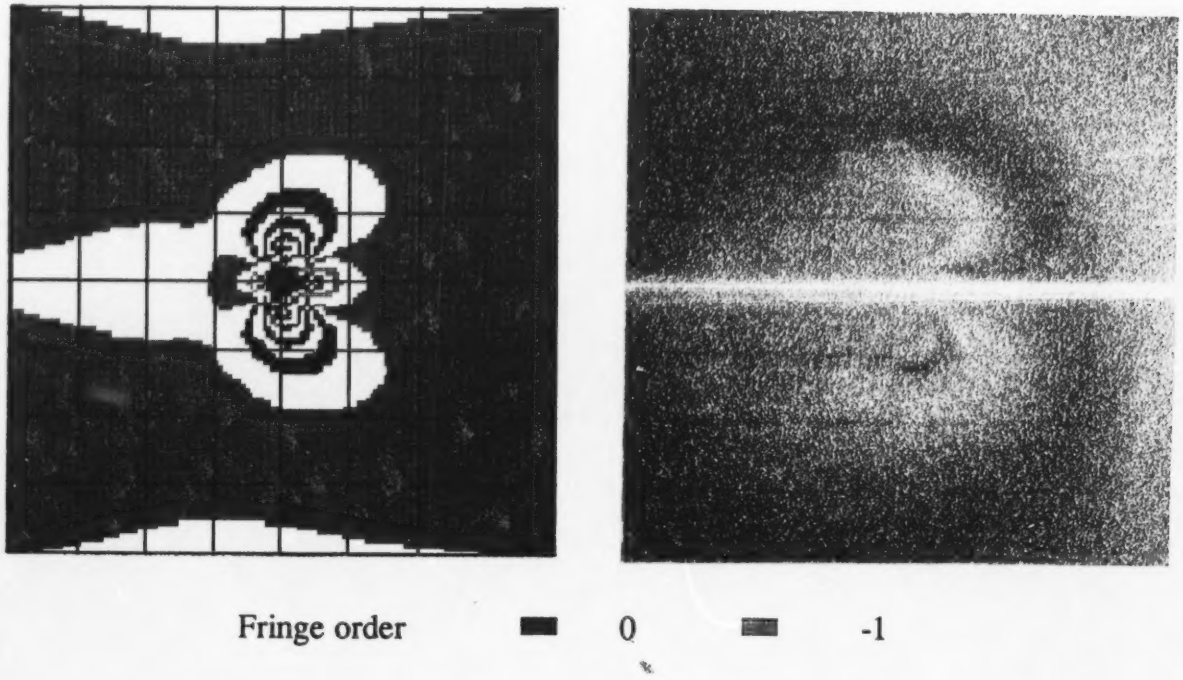

Figure 5-8a Synthetic and observed fringe patterns of the plexiglass sample with a stress-relief hole diameter of 0.5 cm and a depth of 1.0 cm, and an uniaxial stress of 4.0 MPa applied in the vertical direction. The fringe patterns are shown in a 8.0 cm x 8.0 cm area with centimetre grids. In the synthetic fringe pattern, the dark fringes have the orders 0, 1, 2, 3, 4, and 5 from the top or bottom boundary towards the stress-relief hole, and 0, -1, and -2 from the right or left boundary towards the stress-relief hole.

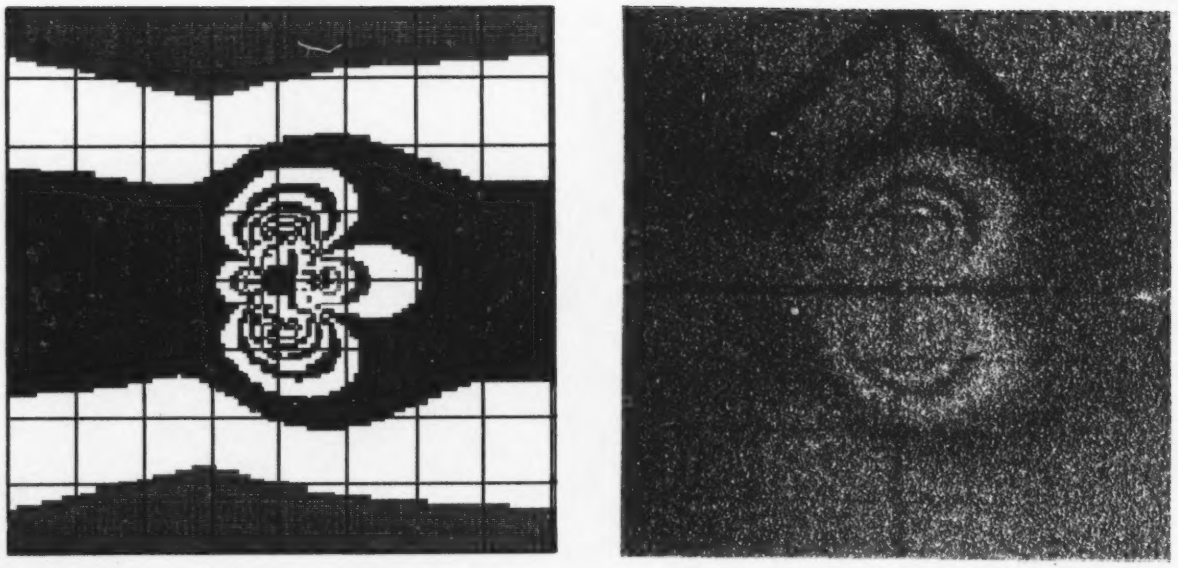

Figure 5-8b Synthetic and observed fringe patterns of the plexiglass sample with a stress-relief hole diameter of 0.5 cm and a depth of 1.0 cm, and an uniaxial stress of 8.0 MPa applied in the vertical direction. The fringe patterns are shown in a 8.0 cm x 8.0 cm area with centimetre grids. In the synthetic fringe pattern, the dark fringes have the orders 0, 1, 2, 3, 4, 5, and 6 from the top or bottom boundary towards the stress-relief hole, and 1, 0, -1, -2, and -3 from the right or left boundary towards the stress-relief hole.

period is one and half to two hours less than that used in other experiments. The non-emergence of the horizontal lobes is possibly due to the effects of the thermal expansion. A detailed analysis of this effect will be given in next section.

According to these two series of experiments, the following preliminary conclusions may be made. First, the effect of the depth of a stress-relief hole on the fringe patterns is substantial. When the depth is 0.5 cm, the lobes cover only a small area, this area increases rapidly to the depth of 2.0 cm. The substantial change of the fringe patterns for the hole depth greater than the hole diameter indicates that the stability criteria used for strain measurement in nondestructive testing is inadequate for the holographic experiment. Second, a general observation is that the noise, which may consist of spurious translations or thermal expansion, is suppressed for the deep holes due to the larger stress-relief displacements. Finally, and most importantly, the synthetic fringe patterns match well with the observed fringe patterns. This fact indicates that the finite element analysis appropriately models the stress-relief displacements.

Analytic calculations are usually easier to implement, especially when an iterative analysis is required. In practice, therefore, one would still hope that an analytic model would suffice to provide the correct displacements. In order to test the validity of the existing analytic models, Figure 5-9 gives the synthetic fringe patterns of the analytic plate model and infinite deep hole model with the same parameters as Figure 5-7b. As seen in Figure 5-9, the fringe patterns are substantially different from that of Figure 5-7b. In

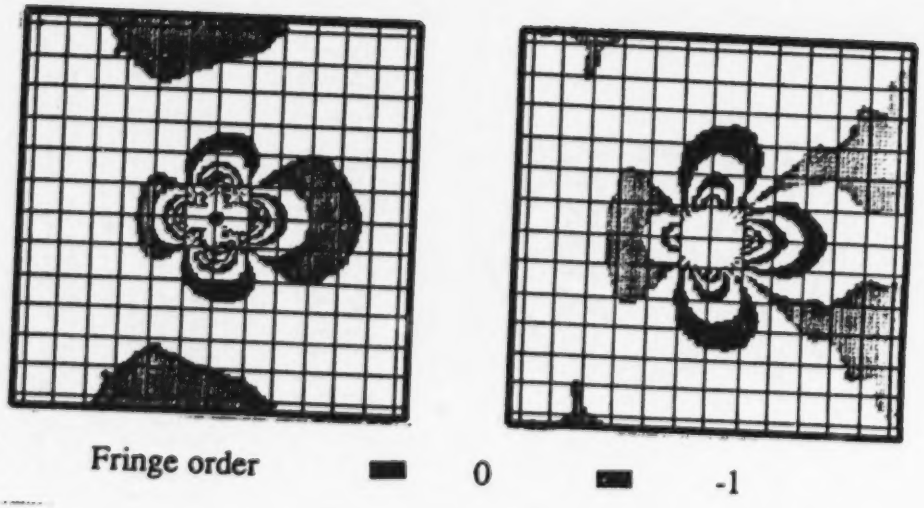

Figure 5-9 Synthetic fringe patterns for plexiglass samples with a stress-relief hole diameter of 0.5 cm and an applied uniaxial stress of 6.0 MPa for plate model with thickness of 2.0 cm (left) and the infinite depth hole model (right). The fringe patterns are shown in a 12.7 cm x 12.7 cm area with centimetre grids. There are no fringes in the 2.0 diameter region for the infinite depth hole model because the solution of Smither et al. (1991) is not provided.

particular, both analytic fringe patterns display large horizontal lobes. This suggests that neither analytic models correctly model the observed fringe pattern.

5.4 Thermal Error

The thermal expansion induced by frictional heating by the drill bit is manifest as the thermal displacements of the surfaces of the plexiglass sample. This is a major source of the error in our experiments and is the reason that the time between exposures was a few hours long. The following analysis of the thermal effects may be able to explain the mismatch of some of the fringe patterns, such as seen in Figure 5-8b.

The magnitude of thermal expansion is related to the speed of the drilling, the force applied to the drill bit, the time used for drilling, and the size of hole to be drilled. Here, the speed of the drilling is considered constant. The force applied to drill is unknown because the drill is manually applied. In general, the deeper the hole is drilled, the greater the thermal heating and subsequent expansion.

In the experiments, if the second exposure is taken immediately after drilling, the fringe patterns are seriously disturbed by the thermal expansion. This case is especially apparent when a deep hole is drilled. In some cases, the fringes induced by stress relief are nearly entirely obscured by thermal fringes and are uninterpretable with respect to stress information. In order to eliminate the effect of the thermal expansion, the time duration between exposures was tested from a half hour to three hours by increments of a half hour. A time duration of two and half hours or more was finally chosen for

use in the experiments to allow the samples to cool.

The surface thermal displacements caused by thermal expansion have the following characteristics. First, since the thermal source is the wall of the stress-relief hole, the thermal displacements are large around the edge of the stress-relief hole and decline with increasing radial distance. Second, unlike the out-of-plane stress-relief displacements which are positive in the axis perpendicular to the uniaxial stress direction and negative in the axis parallel to the stress direction, the out-of-plane thermal displacements are always positive and result in a bulging out of the material.

Two cases are most interesting in our study. The first is the fringe pattern produced only by thermal displacements. The second is the fringe pattern produced by the displacements in which the stress-relief displacements mix with the thermal displacements.

The fringe pattern produced only by the thermal displacements was observed by taking a double-exposure hologram with both exposures after drilling. Figure 5-10 shows an example of the experiment subject to the same conditions as Figure 5-7b. The difference of this experiment from Figure 5-7b is that the first exposure was taken immediately after drilling (within two minutes) while the second exposure was taken one hour later. This fringe pattern may be described as a series of concentric circles with increasing fringe density near the hole. This is consistent with the first expected characteristic of the thermal expansion mentioned above.

The case in which the thermal displacements mix with the stress-relief displacements was observed by taking the second exposure immediately (within three minutes) after drilling. An observed fringe pattern subject to

the same conditions as Figure 5-7b is shown in Figure 5-11. In comparison, the observed fringe patterns of Figures 5-11 and 5-7b are much different. The fringe lobes along the vertical axis in Figure 5-11 are reduced while those along the horizontal axis are expanded. The reason for the change of the lobes is that the out of plane thermal displacements increase the magnitude of the out-of-plane displacements in the horizontal axis and suppress those in the vertical axis.

As indicated in Figure 5-6, the out-of-plane displacements dominate the formation of the fringe patterns. This suggests, to some degree, that the thermal expansion may be approximately modelled by out-of-plane displacements. An attempt by a trial and error process was made to model the observed fringe pattern of Figure 5-11 by superposing a out-of-plane thermal displacement with an exponential function

$$u_z = 5.329 \times 10^{-4} e^{-2.5\, r} \qquad (5.3)$$

on the displacements of the finite element modelling of Figure 5-7b. In this equation, the units of out-of-plane displacement u_z and the radial distance from the centre of the stress-relief hole r both are in centimetres. When r is equal to 0, the displacement value of 5.329×10^{-4} cm which equates the coefficient of equation 5.3 is twice of the magnitude of the out-of-plane displacement at the edge of the stress-relief hole at $\phi = 90^{\circ}$ for the finite element modelling of Figure 5-7b. Comparing the observed and synthetic fringe patterns in Figure 5-11, two fringe patterns are very close, especially with respect to the horizontal lobes.

Note that this simple thermal displacement model is for purposes of illustration only; temperature measurement of the plexiglass sample may help to determine the areal distribution of the thermal displacements. Meanwhile, the substantial thermal expansion we see from this modelling and the experiments indicates that, in retrospect, plexiglass was a poor material to choose due to its extremely high thermal expansion coefficient and low thermal diffusivity. The plexiglass material characteristics required that the experimenter sit quietly in a lightless room for a few hours. Schmitt (1987) observed these thermal displacements in rock also but they were not nearly as severe due to a low coefficient of expansion in dolomitic marlstone.

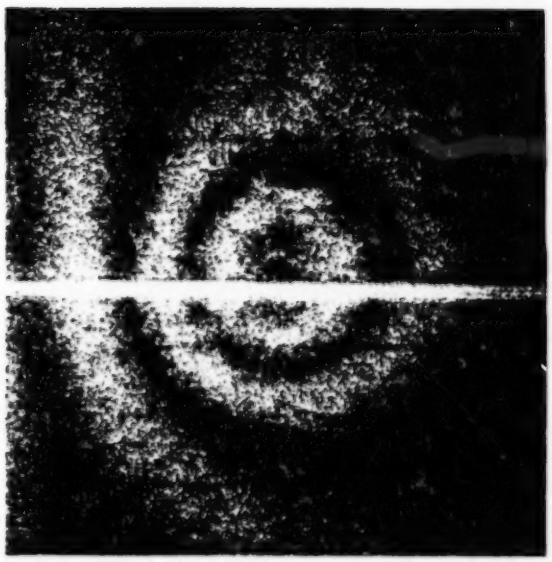

Figure 5-10 Observed fringe pattern induced by the thermal heating when a stress-relief hole of diameter of 0.5 cm and a depth of 1.0 cm is drilled into a plexiglass sample under an uniaxial stress of 6.0 MPa applied in the vertical direction.

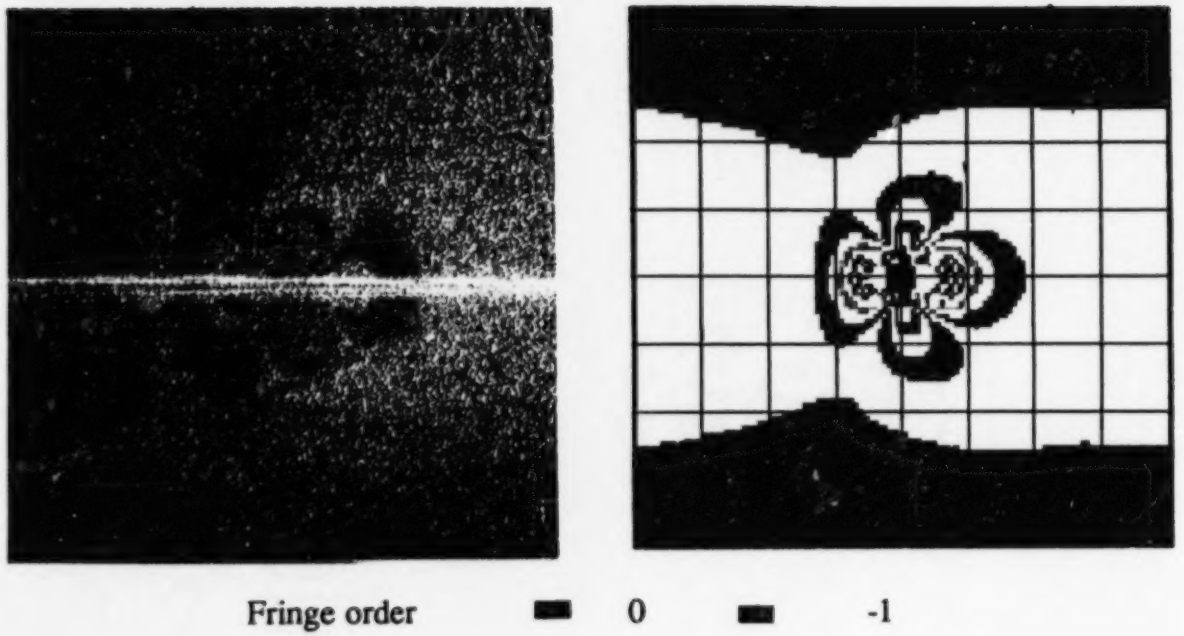

Figure 5-11 Observed and Synthetic fringe patterns of the plexiglass sample with thermal effect and with a stress-relief hole diameter of 0.5 cm and a depth of 1.0 cm, and an uniaxial stress of 6.0 MPa applied in vertical direction. The fringe patterns are shown in a 8.0 cm x 8.0 cm area with centimetre grids. In the synthetic fringe pattern, the dark fringes have the orders 0, 1, 2, and 3 from the top or bottom boundary towards the stress-relief hole, and 0, -1, -2, -3, and -4 from the right or left boundary towards the stress-relief hole.

Conclusions

The primary objective of this thesis was to develop and test a numerical model of stress-relief displacements. The ultimate goal of this work is to determine the in-situ stress tensor by interpreting an interferometric fringe pattern from a double-exposure hologram which records the surface displacements induced by drilling a small finite depth hole into a borehole wall. Assuming that surface stress-relief displacements are induced over a small area relative to the borehole dimensions, the stress-relief displacement model is simplified to a plane surface with an uniform stress distribution in the direction of stress-relief hole. Two existing analytic displacement models for modelling the surface stress-relief displacements are the plate model (Schmitt, 1987) and the infinite depth hole model (Smither and Ahrens, 1991). The interpretation of the field holograms suggests these analytic models may have considerable error due to inappropriate assumptions in their derivation about stress states and the geometry of stress-relief hole. This situation supplies a motivation to use a three dimensional finite element method where the restrictive assumptions of the analytic models are not necessary.

Using the 3-D finite element method, we explored the characteristics of stress-relief displacements and the resulting synthetic holographic fringe patterns under an uniaxial stress. In particular the analysis focussed on the effects of stress-relief hole size, the elastic material properties and the applied stress on the stress-relief displacements. In this analysis, the following results

were obtained:

1. The diameter of a stress-relief hole for a constant depth results in the greatest variation of the magnitude of the displacements. This suggests that selection of the diameter of a stress-relief hole is crucial in measurements of the expected stress state in a given area on the borehole wall.

2. The effect of the stress-relief hole depth on the displacements, especially those out-of-plane, is substantial. Two important results were obtained. First, the stability criteria used in the residual stress measurements when the depth of the stress-relief hole is equal to its diameter is insufficient for the holographic experiment. Second, unlike the analytic plate model of Schmitt (1987), the in-plane displacements from the finite element calculations are a function of the hole depth and the out-of-plane displacements do not depend linearly on the hole depth.

3. The relationship between the applied stresses and the surface stress-relief displacements determined in the finite element modelling is linear as expected. This implies that the applied stress may easily be obtained if the elastic properties of materials remain the same.

4. Poisson's ratio also has a substantial effect on the stress-relief displacements. The change of the displacements due to variation in Poisson's ratio is more complex than the other factors. The magnitude of the radial and vertical displacements in the direction parallel to the applied stress increase and decrease with increasing Poisson's ratio, respectively. The relationship switches at the azimuth perpendicular to the direction of the applied stress.

A comparison of the analytic and the finite element models were conducted by using an example with a stress-relief hole diameter of 0.5 cm

and a depth of 2.0 cm for a SH/E ratio of 1.0 MPa/GPa and a Poisson's ratio of 0.25. The results show that the finite element model with a finite depth hole produces the smallest displacements while the infinite depth hole model produces the greatest. The difference between these models are quantitatively evaluated by a least squares method. When the stress-relief displacements of the analytic models best fit those of the finite element model with a finite depth hole, the applied stress predicted by the analytic plate model is 53 percent less and by the infinite depth hole model is 75 percent less. Application of these analytic models to stress analysis consequently results in an underestimation of stress magnitudes.

To further prove the feasibility of the 3-D finite element model, holographic experiments were conducted on blocks of plexiglass with dimensions of 12.7 cm x 12.7 cm x 5.08 cm. Young's modulus and Poisson's ratio of the plexiglass were measured in the laboratory to be 3.0 ± 0.05 GPa and 0.4 ± 0.01, respectively. Two groups of experiments were carried out. In the first set, the depth of stress-relief hole was varied whereas in the second set the magnitude of the applied uniaxial load was changed. The comparison shows that 3-D finite element method is effective because the observed and the synthetic fringe patterns are consistent. One problem in the experiments was that the thermal displacements generated by drilling a stress-relief hole are a major source of noise. This noise was eliminated by allowing the samples to cool prior to taking the second picture.

One of the remaining problems is that the simplified model used in this thesis with a plane surface and uniform applied stress distribution along the depth of the model may not satisfy the actual boundary conditions and stress

state encountered in a borehole. At present, the errors introduced by this simplification are unknown. Hence, modelling according to the actual boundary conditions of a borehole will be necessary.

The other is a 3-D 20-node isoparametric solid element should be used in future study. This element is a higher version of the 3-D 8-node isoparametric solid element used in this thesis and is better suited to model curved boundaries such as the wall of a stress-relief hole or the wall of a borehole in our problem.

From this study, we see that the combination of the holographic method and the 3-D finite element method shows potential for accurate quantitative measurement of the in situ stress tensor. Although the research in this thesis is motivated by borehole measurements, the method may be more applicable to the determination of in situ stresses in other areas of interest related to civil and mechanical engineering.

Future work which builds on the present study will include development of a scheme for the direct inversion of the fringe patterns for the stresses and the construction of a holographic tool for use in mining applications. We are also presently working collaboratively with Dr. T. Ahrens on his present holographic system and hope to soon apply this system to stress measurements near the San Andreas fault in Southern California.

REFERENCES

Baran, N.M., Finite Element Analysis on Microcomputers, McGraw-Hill,1988.

Bass, J.D., Schmitt, D. R. and Ahrens, T. J., Holographic In Situ Stress Measurements, Geophys. J. R. astr. Soc., 85, pp.13-41, 1986.

Chow, C.L. and Cundiff, C.H., On Residual-Stress Measurements in Light Truck Wheels Using the Hole-Drilling Method, Exp. Mech., 25, pp. 54-59, 1985.

Cohn, S.N., Holographic In-Situ Stress Measurement in Geophysics, Ph. D. thesis, California Institute of Technology, 1983.

Cooling, C.M., Hudson, J.A.and Tunbridge, L.W., In-situ Rock Stress and Their Measurement in the U.K., Part II. Site Experiments and Stress Field Interpretation, J. Rock Mech. Min. Sci. & Geomech. Abstr., 25, pp. 371-382, 1988.

Crouch, S.L., A Note on the Stress Concentrations at the bottom of a Flat Borehole, J. of the South African Institute of Mining and Metallurgy, pp. 100-102, 1969.

de Larminat and Wei, R.P., Normal Surface Displacement Around a Circular Hole by Reflection Holographic Interferometry, Exp. Mech., 18, pp. 74-80, 1978.

Department of Mechanical Engineering, Chengdu University of Technology and Sciences, Finite Element Method in Elasticity, 1984.

Desalvo, G. J. and Gorman, R. W., ANSYS Engineering Analysis System, User's Manual, 1989.

Evans, W.T. and Premier, G.C., Holographic Analysis of the Deformation of a Diesel Engine Piston, Exp. Mech., 29, pp. 455-459, 1989.

Fairhurst,C., In Situ Stress Determination –– an Appraisal of Its Significance in Rock Mechanics, Proc. Int. Symp. on Rock Stress and Rock Stress Measurements, pp. 3-17, 1986.

Fenner, R. T., Engineering Elasticity--Application of Numerical and Analytical Techniques, Sohn Wiley & Sons, pp 228-pp236, pp274-275, 1986.

Flaman, M.T. and Boag, J.M., Comparison of residual-stress Variation with Depth-Analysis Technique for the Hole-drilling Method, Exp. Mech., 30, pp.352-355, 1990.

Flaman, M.T. and Manning, B.H., Determination of Residual-Stress Variation with Depth by Hole-Drilling Method, Exp. Mech., 25, pp. 205-207, 1985.

Francon, M., Holography, Academic Press, 1974.

Hast, H., Limits of Stress Measurements in the Earth's Crust, Rock Mechanics, 11, pp.143-150, 1979.

Hiramatsu, Y. and Oka, Y., Stress Around a Shaft or Level Excavated in Ground with a Three-Dimensional Stress State, Mem. Fac. Engng., Kyoto, 24, pp. 56-76, 1962.

Huang, Y., Engineering Elasticity, Qinghua University Press, 1982.

Hughes, T.J.R., Ferencz, R.M., and Raefsky, A.Y., The finite Element Method: Linear Static and Dynamic Finite Element Analysis Prentice-Hall, Englewood Cliffs, NJ, 1987.

Hudson, J.A. and Cooling C.M., In Situ Rock Stresses and Their Measurement in the U.K., Part I. The Current State of Knowledge, J. Rock Mech. Min. Sci. & Geomech. Abstr., 25, pp. 363-370, 1988.

ISRM, Suggested Methods for Rock Stress Determination, Int. J., Rock. Mech. Sci. & Geomech. Abstr., 24, pp. 53-73, 1987.

Jaeger, J.C., and Cook, G.W., Fundamental of Rock Mechanics, Third Edition, Chapman and Hall, 1979.

Kielbassa, S.and Duddeck, H., Stress-Strain Field at the Tunelling Face-Three-dimensional Analysis for Two-dimensional Technical Approach, Rock Mechanics and Rock Engineering, 24, pp.115-132, 1991.

Lang, P.A., Thompson, P.H. and Ng, L.K.W., The effect of Residual Stress

and Drill Holes Size on the In Situ Stress Determined by Overcoring, Proc., of the Int. Symp. on Rock Stress and Rock Stress Measurements, Stockholm, pp.687-694, 1986.

Leeman, E.R., and Hayes, D.J., A Technique for Determining the Complete State of Stress in Rock Using a single borehole, Proc. 1st Cong. Int. Soc. Rock. Mech., Lisbon, 2, pp. 17-24, 1966.

Leeman, E.R., The determination of the Complete State of Stress in Rock in a Single Borehole --- Laboratory and Underground Measurements, Int J. Rock Mech. Min. Sci. , 5, pp. 31-56, 1968.

Leeman, E.R., The CSIR "Doorstopper" and Triaxial Rock Stress Measuring Instruments, Rock Mechanics, 3, pp. 25-50, 1971.

Logters, G. and Voort, H., In Situ Determination of the Deformation Behaviour of a Cubical Rock-Mass Sample Under Tri-Axial Load, Rock Mechanics, 6, pp. 65-79 1974.

Nelson, D.V. and McCrickerd, J.T., Residual-Stress Determination Through Combined Use of Holographic Interferometry and Blind-Hole Drilling, Exp. Mech., 26, pp.371-378, 1986.

Ostrovsky Y.I., Shchepinov, V.P. and Yakovlev, V.V., Holographic Interferometry in Experimental Mechanics, Springer-Verlag, 1991.

Park, D.-W. and Jung, J.-O., Application of Holographic Interferometry to the Study of Time-Dependent Behaviour of Rock and Coal, Rock Mechanics and Rock Engineering, 21, pp. 259-270, 1988.

Rendler, N. J. and Vigness, I., Hole-drilling Strain-gage Method of Measuring Residual Stresses, Exp. Mech., 6, pp.577-586, 1966.

Schmidt, J. L., Ahrens, T. J., Jacoby, J. L., Tomren, D. R., Evensen, D. A. and Bhuta, P. G., An Optical Instrument for In-situ Stress Measurements in Rocks, TRW Rep. AT-SVD-TR-74-6.

Schmitt, D. R., Smither, C. and Ahrens, T.J., In-situ Holographic Elastic Moduli Measurements from Boreholes, Geophysics, 54, pp. 468-477, 1988.

Schmitt, D. R., Application of Double-Exposure Holography to the Measurement of In Situ Stress and the Elastic Moduli of Rock from a Borehole, Ph.D Thesis, California Institute of Technology, 1987.

Seferlind, L. J., Applied Finite Element Analysis, John Wiley & Sons, 1976.

Smith, H. M., Principles of Holography, Wileey —— Intersciences, 1969.

Smith, I, M., Programming the Finite Element Method, John Wiley & Sons, 1982.

Smither, C. L.and Ahrens, T.J., Displacements from Relief of In Situ Stress by a Cylindrical Hole, Int. J. Rock Mech. Min. Sci. & Geomech. Abstr., 28, pp. 175-186, 1991.

Smither, C. L., Stress-relief Displacements Induced by Drilling, Ph. D. Thesis, California Institute of Technology, 1992.

Smither, C. L., Schmitt, D.R. and Ahrens, T.J., Analysis and Modelling of Holographic Measurements of In Situ Stress, Int. J. Rock Mech. Min. Sci. & Geomech. Abstr., 25, pp. 353-362, 1988.

Sternberg E. and Sadowsky, M.A., Three-Dimensional Solution for the Stress Concentration Around a Circular Hole in a Plate of Arbitrary Thickness, J. Applied Mech., 16, 1949.

Swanson Analysis System, Inc., ANSYS Primer for Stress Analysis, Revision 4.4, 1989.

Unwin, D., An Introduction to Trend Surface Analysis, University of Leicester, 1969.

Van Heerden, W.L., Stress Concentration Factor for the Flat Borehole End for Use in Rock Stress Measurements, Eng. Geol., 3, pp. 307-323, 1969.

Wang, Y. and Wong, T.F., Finite Element Analysis of Two Overcoring Techniques for In Situ Stress Measurement, Int. J. Rock Mech. Min. Sci. & Geomech.Abstr., 24, pp. 41-52, 1987.

Wang, J.-Y, Measurement of Residual Stress by the Hole-Drilling Method: General Stress-Strain Relationship and its solution, Exp. Mech. 28, pp.355-358, 1988.

Will, P., Totzauer, W., and Michel, B., Analysis of Surface Cracks by Holography, Theoretical and Applied Fracture Mechanics, 9, pp.33-38, 1988.

Wittke, W., Rock Mechanics, Theory and Applications with Case Histories, Springer-Verlag, 1990.

Xue, Z.-L., Elasticity, People's Education Press, 1979.

Youngdahl, C.K. and Sternberg, E., Three-Dimensional Stress Concentration Around a Cylindrical Hole in a Semi-Infinite Elastic Body, J. Appl. Mech., 33, pp. 855-865, 1966.

Zou, D.-H. and Kaiser, P.K., Determination of In Situ Stresses from Excavation-Induced Stress Changes, Rock Mechanics and Rock Engineering, 23, pp. 167-184, 1990.

Appendices

APPENDIX A: Introduction of 3-D Finite Element Method

The basic equation of the finite element analysis for a linear, static problem is (Desalvo and Gorman, 1989)

$$[K]\{u\} = \{R\}, \tag{A.1}$$

where

[K] = total stiffness matrix (sum of element stiffness matrices);

{u} = nodal displacement vector;

{R} = nodal load vector.

Equation A.1 is a set of linear equations. In theory, the finite element calculation is to solve this set of linear equations in order to obtain the nodal displacement vector {u} of a finite element model. To solve {u}, the essential work is to establish the total stiffness matrix [K]. Because the matrix [K] is an assembly of element stiffness matrices [k], the derivation of the element stiffness matrix [k] is the basis of the finite element method. In the following, we will discuss how the matrix [k] is derived and how the total stiffness matrix is then assembled.

First, we review three fundamental equations which describe the relationship between stress tensor, strain tensor and displacements of a three dimensional problem of elasticity with isotropic material properties. These

equations are

(i) The equilibrium conditions

$$\begin{bmatrix} \frac{\partial}{\partial x} & 0 & 0 & \frac{\partial}{\partial y} & 0 & \frac{\partial}{\partial z} \\ 0 & \frac{\partial}{\partial y} & 0 & \frac{\partial}{\partial x} & \frac{\partial}{\partial z} & 0 \\ 0 & 0 & \frac{\partial}{\partial z} & 0 & \frac{\partial}{\partial y} & \frac{\partial}{\partial x} \end{bmatrix} \begin{Bmatrix} \sigma_x \\ \sigma_y \\ \sigma_z \\ \tau_{xy} \\ \tau_{yz} \\ \tau_{zx} \end{Bmatrix} = - \begin{Bmatrix} F_x \\ F_y \\ F_z \end{Bmatrix} , \qquad \text{(A.2)}$$

where σ_x, σ_y, σ_z, τ_{xy}, τ_{yz}, and τ_{zx} are stress components and F_x, F_y, and F_z are body forces.

(ii) The constitutive equations

$$\begin{Bmatrix} \sigma_x \\ \sigma_y \\ \sigma_z \\ \tau_{yz} \\ \tau_{yz} \\ \tau_{zx} \end{Bmatrix} = \frac{E(1-\nu)}{(1+\nu)(1-2\nu)} \begin{bmatrix} 1 & \frac{\nu}{1-\nu} & \frac{\nu}{1-\nu} & 0 & 0 & 0 \\ \frac{\nu}{1-\nu} & 1 & \frac{\nu}{1-\nu} & 0 & 0 & 0 \\ \frac{\nu}{1-\nu} & \frac{\nu}{1-\nu} & 1 & 0 & 0 & 0 \\ 0 & 0 & 0 & \frac{1-2\nu}{2(1-\nu)} & 0 & 0 \\ 0 & 0 & 0 & 0 & \frac{1-2\nu}{2(1-\nu)} & 0 \\ 0 & 0 & 0 & 0 & 0 & \frac{1-2\nu}{2(1-\nu)} \end{bmatrix} \begin{Bmatrix} \varepsilon_x \\ \varepsilon_y \\ \varepsilon_z \\ \gamma_{xy} \\ \gamma_{yz} \\ \gamma_{zx} \end{Bmatrix} , \qquad \text{(A.3)}$$

where E is the modulus of elasticity (Young's modulus) and ν is Poisson's ratio and ε_x, ε_y, ε_z, γ_{xy}, γ_{yz}, and γ_{zx} are strain components.

and (iii) the strain-displacement definition

$$\begin{Bmatrix} \varepsilon_x \\ \varepsilon_y \\ \varepsilon_z \\ \gamma_{xy} \\ \gamma_{yz} \\ \gamma_{zx} \end{Bmatrix} = \begin{bmatrix} \frac{\partial}{\partial x} & 0 & 0 \\ 0 & \frac{\partial}{\partial y} & 0 \\ 0 & 0 & \frac{\partial}{\partial z} \\ \frac{\partial}{\partial y} & \frac{\partial}{\partial x} & 0 \\ 0 & \frac{\partial}{\partial z} & \frac{\partial}{\partial y} \\ \frac{\partial}{\partial z} & 0 & \frac{\partial}{\partial x} \end{bmatrix} \begin{Bmatrix} u \\ v \\ w \end{Bmatrix} , \qquad (A.4)$$

where u, v, and w are the displacement components in the x, y, and z directions.

Using **F**, σ, ε, and **e** to represent the body forces, the stress tensor, the strain tensor and the displacement vector, respectively, equations A.2, A.3 and A.4 may be abstracted to

$$\mathbf{A}^T\sigma = -\mathbf{F}, \qquad (A.5)$$

$$\sigma = \mathbf{D}\,\varepsilon, \qquad (A.6)$$

and

$$\varepsilon = \mathbf{A}\mathbf{e}, \qquad (A.7)$$

respectively, where **A** is the strain-displacement operator, and **D** is the stress-strain matrix.

We now turn to discuss the relationship of the nodal displacements and the displacements in an element. For a finite element analysis, the displacements in an element need to be approximated by a set of displacement functions which usually are a set of polynomials with the form

$$u(x,y,z) = a_1 + a_2x + a_3y + a_4z + a_5x^2 + a_6y^2 + a_7z^2 + a_8xy + a_9yz + a_{10}zx + ...+ a_mz^n,$$

$$v(x,y,z) = a_{m+1} + a_{m+2}x + a_{m+3}y + a_{m+4}z + a_{m+5}x^2 + a_{m+6}y^2 + a_{m+7}z^2 + a_{m+8}xy + a_{m+9}yz + a_{m+10}zx + ...+ a_{2m}z^n,$$

$$w(x,y,z) = a_{2m+1} + a_{2m+2}x + a_{2m+3}y + a_{2m+4}z + a_{2m+5}x^2 + a_{2m+6}y^2 + a_{2m+7}z^2 + a_{2m+8}xy + a_{2m+9}yz + a_{2m+10}zx + ...+ a_{3m}z^n. \quad (A.8)$$

These polynomials may be truncated at an arbitrary order according to accuracy requirements. The polynomials with higher order will results in a more accurate displacement solution for an element. If the truncation is at the fourth term, a set of linear displacement functions will be given.

The ultimate objective here is to express the displacements in an element by the nodal displacements. To reach this objective, the nodal coordinates are first substituted into the polynomials which have been truncated such that the left side of the polynomials is the nodal displacements represented by the nodal coordinates and the coefficients on the right side. Secondly, the coefficients which are the functions of the nodal displacements and the nodal coordinates are obtained by solving the polynomials. The relation of the nodal displacements and the displacements in an element are finally derived by substituting the resulting coefficients into the original polynomials. The relation is

$$\mathbf{e} = \mathbf{N}\,\delta^{e}, \qquad \text{(A.9)}$$

where **N** is a matrix consisting of element shape functions. The element shape function is important in finite element analysis because it gives the displacement 'shape' in an element.

For example, a linear rectangular brick element of eight nodes as shown in Figure A-1 has the shape functions (Smith, 1982) of

$$N_i = \frac{1}{8}(1 + \xi_0)(1 + \eta_0)(1 + \zeta_0), \quad (i = 1, 2, 3, \ldots, 8), \qquad \text{(A.10)}$$

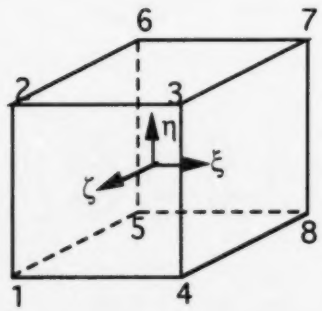

Figure A-1 Rectangular brick element

where ξ, η, and ζ form a local coordinate system with the origin at the geometric centre, $\xi_0 = \xi\xi_i$, $\eta_0 = \eta\eta_i$ and $\zeta_0 = \zeta\zeta_i$ are the variables in this element, and ξ_i, η_i, and ζ_i are the nodal coordinates which are either equal to 1 or -1. The full matrix **N** is

$$\mathbf{N} = \begin{bmatrix} N_u & 0 & 0 \\ 0 & N_v & 0 \\ 0 & 0 & N_w \end{bmatrix} \qquad \text{(A.11)}$$

where $N_u = N_v = N_w = [N_1, N_2, N_3, N_4, N_5, N_6, N_7, N_8]$ corresponds to the three displacement components u, v, and w. The transpose of the nodal displacement vector $(\delta^e)^T = [u_1, u_2, u_3, u_4, u_5, u_6, u_7, u_8, v_1, v_2, v_3, v_4, v_5, v_6, v_7, v_8, w_1, w_2, w_3, w_4, w_5, w_6, w_7, w_8]$. If the matrix **N** and the nodal displacement vector δ^e are substituted into equation A.9, the relationship of the nodal displacements and the displacements in this brick element will be established.

Once the shape functions are obtained, the next step is to derive the element stiffness matrix [k] from energy principles. For an alternative method, the principle of virtual work (Fenner, 1986)

$$\sum_i F_i^* \, d\delta_i^* = \int\int\int (\sigma_x^* d\varepsilon_x^* + \sigma_y^* d\varepsilon_y^* + \sigma_z^* d\varepsilon_z^* + \sigma_{xy}^* d\varepsilon_{xy}^* + \sigma_{yz}^* d\varepsilon_{yz}^* + \sigma_{zx}^* d\varepsilon_{zx}^*) \, dx \, dy \, dz, \qquad \text{(A.12)}$$

is used here, where F_i^* is the external load, and $d\delta_i^*$, and $d\varepsilon_x^*$, $d\varepsilon_y^*$ and so on are the infinitesimal virtual displacement and virtual strain changes, respectively. Assuming that there are virtual displacements in an element, the corresponding nodal virtual displacements vector and virtual strain tensor are δ^{*e} and ε^*, respectively. Consequently, from equation A.12 we have

$$(\delta^{*e})^T \mathbf{F}^e = \int\int\int (\varepsilon^*)^T \sigma \, dx \, dy \, dz \qquad \text{(A.13)}$$

where $\mathbf{F}^e$ is the nodal force vector of an element. Substituting equations A.7 and A.9 into equation A.13, thus

$$(\delta^{*e})^T \mathbf{F}^e = \int\int\int (\delta^{*e})^T (\mathbf{A}\mathbf{N})^T \sigma \, dx \, dy \, dz \quad . \tag{A.14}$$

Because the virtual nodal displacements in δ^{*e} are constant variables, equation A.14 becomes

$$\mathbf{F}^e = \int\int\int (\mathbf{A}\mathbf{N})^T \sigma \, dx \, dy \, dz \quad . \tag{A.15}$$

In terms of equations A.6, A.7, and A.9, we have

$$\sigma = \mathbf{D}\,(\mathbf{A}\mathbf{N})\,\delta^e. \tag{A.16}$$

Using this relation in equation A.15, and considering the nodal displacement components in δ^e are constant variables, hence

$$\mathbf{F}^e = \left\{\int\int\int (\mathbf{A}\mathbf{N})^T \mathbf{D}(\mathbf{A}\mathbf{N}) \, dx \, dy \, dz\right\}\delta^e \quad . \tag{A.17}$$

Letting $\mathbf{B} = \mathbf{AN}$ and rewriting this equation, we have

$$\mathbf{F}^e = [k]\ \delta^e \quad , \tag{A.18}$$

where the matrix

$$[k] = \int\int\int (\mathbf{B})^T \mathbf{D}(\mathbf{B})\ dx\ dy\ dz \qquad (A.19)$$

is the element stiffness matrix.

If the displacement functions are linear the matrices **B** and **D** will only contain constant variables then equation A.19 simplifies to

$$[k] = (\mathbf{B})^T \mathbf{D}\ (\mathbf{B})\ \Delta V, \qquad (A.20)$$

where ΔV is the volume of element.

When the element stiffness matrix [k] is derived, the assembly of the total stiffness matrix [K] is able to be implemented in terms of equation A.18. This is a relatively straightforward as the elements are mathematically connected to each other by their nodes. If the total stiffness matrix [K] is established, the nodal load vector {**R**} will be formed automatically according to the arrangement of nodes and finally the nodal displacement vector {u} in equation A.1 will be solved.

APPENDIX B: Programs

Program I

THIS IS A PROGRAM OF ANSYS 4.4 OF STRESS ANALYSIS USED FOR COMPUTING STRESS-RELIEF DISPLACEMENTS ON THE SURFACE OF A INFINITE HALF-SPACE. THE COMPUTED MODEL HAS SIZE OF 30 CM X 30 CM X 12 CM WITH 1782 NODES AND 1352 ELEMENTS (WITHOUT HOLE). THE SIZES OF THE STRESS-RELIEF HOLES ARE DIAMETERS OF 0.5 CM AND DEPTHS OF 0.5, 1.0, 1.5 ,2.0, 2.5, 3.0, 3.5, 4.0 CM.

FILE NAME: FEMSRD

SEPTEMBER 6, 1991

```
C
C PREPROCESSING
C
   /prep7
   /show,,,2 (vector plot)
   /view,,-0.2,0.2,-0.2
   eplot
C
C Set coordinate systems by key points and change the vertical axis from y to z
C
   k,1
   k,2,1
   k,3,,,1
   cskp,11,0,1,3,2
   cskp,12,1,1,3,2
C
C Active cylindrical coordinate system
C
   csys,12
C
C Define element type
C
   et,1,45
C
C Define material properties (elastic modulus and Poisson's ratio)
C
   ex,1,2e11
   nuxy,1,0.25
C
C Generate nodes in the horizontal
```

```
C
    n,1
    n,2,0.05
    n,6,0.05,90
    fill
    ngen,4,5,2,6,1,0.1
    ngen,2,5,17,21,1,0.2
    ngen,2,5,22,26,1,0.25
    ngen,2,5,32,36,1,0.5
    ngen,2,5,37,41,1,1.0
    ngen,2,5,42,46,1,2.0
    ngen,2,5,47,51,1,4.1
C
C  Active globe coordinate system
C
    csys,11
C
C  Generate nodes continuously
C
    n,57,16
    n,58,16,6.6274
    n,59,16,16
    n,60,6.6274,16
    n,61,,16
    n,62,30
    n,63,30,12.426
    n,64,30,30
    n,60,12.426,30
    n,61,,30
C
C  Generate nodes in the vertical
C
    ngen,2,66,1,66,1,,,2.0
    ngen,2,66,67,132,1,,,1.5
    ngen,2,66,133,198,1,,,1.3
    ngen,2,66,199,264,1,,,1.0
    ngen,2,66,265,330,1,,,0.8
    ngen,2,66,331,396,1,,,0.4
    ngen,21,66,397,462,1,,,0.25
C
C  Generate elements.
C
    e,1,2,3,3,67,68,69,69
    e,1,3,4,4,67,69,70,70
    e,1,4,5,5,67,70,71,71
    e,1,5,6,6,67,71,72,72
C
    e,2,7,8,3,68,73,74,69
    egen,4,1,5
    egen,11,5,5,8,1
    egen,10,66,1,52,1
```

```
C
C  Specify boundary conditions
C
C    constraints
C
     nsel,y,-0.1,0.01
     d,all,ux
     nall
     nsel,x,-0.1,0.01
     d,all,uz
     nall
     nsel,z,-0.1,0.01
     d,all,uy
C
C    load (uniaxial stress)
C
     nsel,y,29.9,30.1
     psf,all,,,2e8
     nall

C
C  Delete some of elements to form a stress-relief hole. Only one of the following
C  deletions is used in practical computing for a given hole size.
C
C    hole depth 0.5 cm
C
     edele,1301,1312
     edele,1249,1260
C
C    hole depth 1.0 cm
C
     edele,1197,1208
     edele,1145,1156
C
C    hole depth 1.5 cm
C
     edele,1093,1104
     edele,1041,1052
C
C    hole depth 2.0 cm
C
     edele,989,1000
     edele,937,948
C
C    hole depth 2.5 cm
C
     edele,885,896
     edele,833,844
C
C    hole depth 3.0 cm
C
```

```
    edele,781,792
    edele,729,740
C
C   hole depth 3.5 cm
C
    edele,677,688
    edele,625,636
C
C   hole depth 4.0 cm
C
    edele,583,594
    edele,521,532
C
C  Write data into solver
C
    sfwrite
    finish
C
C SOLUTION
C
    /solve
C
C POSTPROCESSING
C
    /post1
    set
    /show,,,2
    /view,,-0.2,0.2,-0.2
C
C  Active cylindrical coordinate system
C
    csys,12
C
C  Display the deformed shape of  a model
C
    pldisp,  1
C
C  Contour display of stresses and displacements
C
    plnstr,ux   (uy,uz,sige,sig1,sig2,sig3)
C
C  Output stresses
C
    prnstr,all
C
C  Output displacements
C
    prndis,all
C
    finish
C
```

```
C  Exit from ANSYS
C
    /eof
```

Program II

```
C     ------------------------------------------------------------------------
---
C
C THIS PROGRAM IS USED TO COMPUTE STRESS-RELIEF DISPLACEMENTS AND THE
C CORRESPONDING FRINGE ORDERS. THE DATA OF DISPLACEMENTS IS FROM 3-D FINITE
ELEMENT C CALCULATION.
C
C FILE NAME: DISFRI
C
C  JULY 1, 1991
C
C  A, wave length of laser light.
C NP, NR  number of nodes in one path and number of paths.
C N, N1  number of nodes in one quadrant and in four quadrants.
C  M1, M2  real numbers in calculation of direction cosine.
C  X1, Y1, Z1  coordinates of light source of object beam.
C  X2, Y2, Z2  coordinates of the centre of hologram.
C  R(100)  node positions in the radial direction.
C  X(400),Y(400)  node positions in globe coordinates.
C  UHR(100), UHT(100), UHZ(100)  node displacements with stress-relief hole.
C  UBR(100), UBT(100), UBZ(100)  node displacements without stress-relief hole.
C  HBR(100), HBT(100), HBZ(100)  stress-relief displacements.
C NODE1, NODE2 node number.
C  RD1(20,5),TD1(20,5),ZD1(20,5)  arraies used for rearranging stress-relief
C  displacements.
C  RD(100),TD(100),ZD(100)  stress-relief displacements in cylindrical
C  coordinate system.
C  C  XD(400),YD(400),ZD(400) stress-relief displacements in globe
C  coordinate system.
C  ND(400) fringe orders in four quadrants.
C
C     ------------------------------------------------------------------------
-
C
      PARAMETER  (A=6.328E-5,PI=3.141591)
      PARAMETER  (X1=9.70,Y1=0.0,Z1=23.05)
      PARAMETER  (X3=0.0,Y3=0.0,Z3=17.85)
      DIMENSION  X(400),Y(400),XD(400),YD(400),ZD(400),R(100)
      DIMENSION  RD(100),TD(100),RD1(20,5),TD1(20,5),ZD1(20,5)
      DIMENSION  UHR(100),UHT(100),UHZ(100),HBR(100),HBT(100),HBZ(100)
      DIMENSION  UBR(100),UBT(100),UBZ(100),NODE1(100),NODE2(100)

      REAL  M1,M2,ND(400)
      CHARACTER*20 INFILE1,INFILE2,INFILE3,OUTFILE1,OUTFILE2C
C
C Enter the number of node
C
```

```
      WRITE(*,500)
500   FORMAT('enter NR and NP')
      READ(*,600) NR,NP
600   FORMAT(2I5)
      N=NR*NP
      N1=4*N
C
C  Define input file names and output file names
C
      WRITE(*,1000)
1000  FORMAT('enter node position file in cylindrical coordinate system')
      READ(*,1100) INFILE1
1100  FORMAT(A20)

      WRITE(*,1200)
1200  FORMAT('enter hole displacement file in cylindrical coordinate system')
      READ(*,1100) INFILE2

      WRITE(*,1250)
1250  FORMAT('enter block displacement file in cylindrical coordinate system')
      READ(*,1100) INFILE3

      WRITE(*,1300)
1300  FORMAT('enter output file for fringe order')
      READ(*,1100) OUTFILE1

      WRITE(*,1350)
1350  FORMAT('enter output file for stress-relief displacements')
      READ(*,1100) OUTFILE2

      OPEN(UNIT=1,FILE=INFILE1,STATUS='old',ACCESS='SEQUENTIAL',FORM='FORMATTED')
      OPEN(UNIT=2,FILE=INFILE1,STATUS='old',ACCESS='SEQUENTIAL',FORM='FORMATTED')
      OPEN(UNIT=3,FILE=INFILE1,STATUS='old',ACCESS='SEQUENTIAL',FORM='FORMATTED')
C
      READ(1,*)  (R(I),I=1,N)
      READ(2,*)  (NODE1(I),UHR(I),UHT(I),UHZ(I),I=1,N)
      READ(3,*)  (NODE2(I),UBR(I),UBT(I),UBZ(I),I=1,N)
C
      CLOSE(1)
      CLOSE(2)
      CLOSE(3)
C
C  Calculate the difference of displacements
C
      DO 20 I=1,N
        HBR(I)=UHR(I)-UBR(I)
        HBT(I)=UHT(I)-UBT(I)
        HBZ(I)=UHZ(I)-UBZ(I)
20    CONTINUE
C
C  Set the tangential displacements of path1 and path5 to zero (due to too small)
```

```
C
C   Path1
C
        DO 25 I=1,N,5
          HBT(I)=0.0
25      CONTINUE
C
C   Path5
C
        DO 26 I=5,N,5
          HBT(I)=0.0
26      CONTINUE
C
C  Rearrange the displacements from the order in terms of node number
C  to the order in terms of paths
C
        DO 30 J=1,NR
          K=N-5+J
          L=0
          DO 30 I=J,K,NR
            L=L+1
            RD1(L,J)=HBR(I)
            TD1(L,J)=HBT(I)
            ZD1(L,J)=HBZ(I)
30      CONTINUE
C
        K=0
        DO 40 J=1,NR
          DO 40 I=1,NP
            K=K+1
            RD(K)=RD1(I,J)
            TD(K)=TD1(I,J)
            ZD(K)=ZD1(I,J)
40      CONTINUE
C
C  Transform displacements from  the cylindrical to the globe
C
        TH1=0.0
        TH2=PI/8.0
        TH3=PI/4.0
        TH4=3*PI/8.0
        TH5=PI/2.0
C
        DO 100 I=1,NP
          NT1=I
          NT2=I+NP
          NT3=I+2*NP
          NT4=I+3*NP
          NT5=I+4*NP
C
C    Transform the coordinates
```

```
C
          X(I)=R(I)*COS(TH1)
          Y(I)=R(I)*SIN(TH1)
          X(NT2)=R(NT2)*COS(TH2)
          Y(NT2)=R(NT2)*SIN(TH2)
          X(NT3)=R(NT3)*COS(TH3)
          Y(NT3)=R(NT3)*SIN(TH3)
          X(NT4)=R(NT4)*COS(TH4)
          Y(NT4)=R(NT4)*SIN(TH4)
          X(NT5)=R(NT5)*COS(TH5)
          Y(NT5)=R(NT5)*SIN(TH5)
C
C     Transform the displacements
C
          XD(I)=RD(I)*COS(TH1)+TD(I)*COS(PI/2.0+TH1)
          YD(I)=RD(I)*SIN(TH1)+TD(I)*SIN(PI/2.0+TH1)

          XD(NT2)=RD(NT2)*COS(TH2)+TD(NT2)*COS(PI/2.0+TH2)
          YD(NT2)=RD(NT2)*SIN(TH2)+TD(NT2)*SIN(PI/2.0+TH2)

          XD(NT3)=RD(NT3)*COS(TH3)+TD(NT3)*COS(PI/2.0+TH3)
          YD(NT3)=RD(NT3)*SIN(TH3)+TD(NT3)*SIN(PI/2.0+TH3)

          XD(NT4)=RD(NT4)*COS(TH4)+TD(NT4)*COS(PI/2.0+TH4)
          YD(NT4)=RD(NT4)*SIN(TH4)+TD(NT4)*SIN(PI/2.0+TH4)

          XD(NT5)=RD(NT5)*COS(TH5)+TD(NT5)*COS(PI/2.0+TH5)
          YD(NT5)=RD(NT5)*SIN(TH5)+TD(NT5)*SIN(PI/2.0+TH5)
100     CONTINUE
C
C  Reflect one quadrant to four quadrants
C
        DO 150 I=1,N
          IN=I+N
          INN=I+2*N
          INNN=I+3*N
C
          X(IN)=-X(I)
          X(INN)=-X(I)
          X(INNN)=X(I)
          Y(IN)=Y(I)
          Y(INN)=-Y(I)
          Y(INNN)=-Y(I)
C
          XD(IN)=-XD(I)
          XD(INN)=-XD(I)
          XD(INNN)=XD(I)
          YD(IN)=YD(I)
          YD(INN)=-YD(I)
          YD(INNN)=-YD(I)
          ZD(IN)=ZD(I)
```

```
        ZD(INN)=ZD(I)
        ZD(INNN)=ZD(I)
150     CONTINUE
C
C  Calculate fringe order
C
        DO 200 I=1,N1
           M1=SQRT((X(I)-X1)**2+(Y(I)-Y1)**2+Z1**2)
           M2=SQRT((X(I)-X3)**2+(Y(I)-Y3)**2+Z3**2)
C
          ALFA1=(X(I)-X1)/M1
          BLTA1=(Y(I)-Y1)/M1
         GAMM1=-Z1/M1
C
          ALFA2=(X3-X(I))/M2
          BLTA2=(Y3-Y(I))/M2
         GAMM2=Z3/M2
C
         ALFA=ALFA1-ALFA2
         BLTA=BLTA1-BLTA2
         GAMM=GAMM1-GAMM2
          DELTA=2*PI*(XD(I)*ALFA+YD(I)*BLTA+ZD(I)*GAMM)/A
C
          ND(I)=(DELTA/PI-1.0)/2.0
200     CONTINUE
C

    OPEN(UNIT=4,FILE=OUTFILE1,STATUS='NEW',ACCESS='SEQUENTIAL',FORM='FORMATTED')

    OPEN(UNIT=5,FILE=OUTFILE1,STATUS='NEW',ACCESS='SEQUENTIAL',FORM='FORMATTED')
C
C  Output fringe order and stress-relief displacements
C
        DO 300 I=1,N1
          IF(ABS(X(I)).GT.6.5.OR.ABS(Y(I)).GT.6.5) GO TO 300
          WRITE(4,290) X(I),Y(I),ND(I)
290       FORMAT(2F10.5,2X,1F20.10)
300     CONTINUE
C
        WRITE(5,400)  (RD(I),I=1,N)
        WRITE(5,400)  (TD(I),I=1,N)
        WRITE(5,400)  (ZD(I),I=1,N)
400     FORMAT(E20.14)
C
        CLOSE(4)
        CLOSE(5)
C
        STOP
        END
```

Program III

```
-----------------------------------------------------------------------
THE INTERPOLATION OF FRINGE ORDERS BY UNIMAP OF UNIRAS FOR THE DATA FROM THE
GROGRAM DISFRI. THE DATA WITH 200 X 200 GRIDS IS OBTAINED AND WILL BE USED FOR
PLOTTING IMAGE OF SYNTHETIC FRINGE PATTERN.
-----------------------------------------------------------------------

    UNIMAP
        select   mcgi;exit
C
C   Enter stress-relief displacements
C
    data
        irregular
    read
        file name f.8m2
C
C   Enter control parameters to avoid interpolating within stress-relief hole
C
    data
        region
    read
        file  name  Cir/cir0.5ex
    plot
C
C   Interpolate
C
    interpolate
        gridcells
            gridcells in x direction 200
            gridcells in y direction 200
    do
-------------------------------------------------------------
C
C   Output the interpolate data
C
    data
        regular
            write
              file name interpolate.1
              start variables 2
              number of z variables 1
    Exit
```

Program IV

```
C     ------------------------------------------------------------------
C
C THIS PROGRAM IS USED FOR PLOTTING THE IMAGE OF A SYNTHETIC FRINGE
C  PATTERN. THE DATA IS FROM THE INTERPOLATED DATA IN UNIMAP.
C
C FILE NAME: FRIIMA
C
C AUGUST 18, 1991
C
C     ------------------------------------------------------------------
C
      PROGRAM FRIIMA
C
        PARAMETER (NI=30,NZ=29)
        REAL  Z1(250,250),ZCL(29),NSIZE
        INTEGER INDEX(30),NCHAR(3)
        CHARACTER*1  LABELS(3)*5
        CHARACTER*20 INFILE
        CHARACTER*50 TITLE,SUBTITLE
C
C  Set colours of fringes
C
        DATA   INDEX/1,11,1,11,1,11,1,11,1,15,1,30,1,0,1,0,
&           1,0,1,0,1,0,1,0,1,0,1,0,1,0/
C
C  Set number of fringe order
C
        DATA   ZCL/  -5.25,-4.75,-4.25,-3.75,-3.25,-2.75,-2.25,
&              -1.75,-1.25,-0.75,-0.25,
&                0.25,0.75,1.25,1.75,2.25,2.75,3.25,3.75,4.25,4.75,
&             5.25,5.75,6.25,6.75,7.25,7.75,8.25,100.25/
C
C  Define title and subtitle
C
        WRITE(*,100)
100     FORMAT('enter  title')
        READ(*,200)  TITLE
200     FORMAT(A40)

        WRITE(*,300)
300     FORMAT('enter  subtitle')
        READ(*,400) SUBTITLE
400     FORMAT(A50)
C
C  Define numbers of image grids and cm net grids in one dimension
C
        WRITE(*,500)
```

```
500     FORMAT('enter image grids NGR/net grids NET/plot size NSIZE')
        READ(*,600) NGR,NET,NSIZE
600     FORMAT(2I5,1F5.1)
C
C  Define file name of the interpolated data
C
        WRITE(*,1000)
1000    FORMAT('enter interpolated file')
        READ(*,1100) INFILE
1100    FORMAT(A20)
C
        OPEN(1,FILE=INFILE)
        READ(1,*)  ((Z1(I,J),I=1,NGR),J=1,NGR)
        CLOSE(1)
C
C  Connect to UNIRAS
C
        CALL GROUTE('SELECT MCGI;EXIT')
        CALL GOPEN
C
C Prepare an image with an expected ratio
C
        CALL GRPSIZ(XSIZE,YSIZE)
C
        SX=XSIZE/100
        SY=YSIZE/100
        ORX=15.0*SX
        ORY=15.0*SY
        DIMENS=MIN(SX,SY)*NSIZE
C
C Set background colour to white
C
        CALL  RRECT(0,0,XSIZE,YSIZE,1,0)
C
C Set size of image grid
C
        CALL GIMGRD(DIMENS/NGR,DIMENS/NGR)
C
C Set scanning direction
C
        CALL GIMSCN(1)
        CALL  GIMDIR(1,1)
C
C Select CMY colours of 10 levels
C
        CALL  RVMODE(1,0,9999,3,NI)
        CALL GGREY
        CALL RSHADE(INDEX,NI)
        CALL RCLASS(ZCL,NZ,0)
C
C  Initialisation
```

```
C
      CALL GIMORI(ORX,ORY)
      CALL GIMAGE(0,NGR,0)
C
C Read data and process image
C
      DO 30 I=1,NGR
30       CALL GIMAGE(Z1(1,I),NGR,1)
C
C Terminate image generation
C
      CALL GIMAGE(0,NGR,9999)
C
C Plot frame
C
      CALL GWICOL(MIN(SX,SY)*0.45,0)
      CALL GVECT(ORX,ORY,0)
      CALL GVECT(ORX+DIMENS,ORY,1)
      CALL GVECT(ORX+DIMENS,ORY+DIMENS,1)
      CALL GVECT(ORX,ORY+DIMENS,1)
      CALL GVECT(ORX,ORY,1)
C
C  Plot cm net in y direction
C
      CALL GWICOL(MIN(SX,SY)*0.15,23)
C
      NF=NET+1
      DO 40 I=1,NF
        CALL GVECT(ORX+0.35*DIMENS/12.7+(I-1)*DIMENS*NET/NET/12.7,ORY,0)
        CALL GVECT(ORX+0.35*DIMENS/12.7+(I-1)*DIMENS/12.7,ORY+DIMENS,1)
40    CONTINUE
C
C  Plot cm net in x direction
C
      DO 50 I=1,NF
        CALL GVECT(ORX,ORY+0.35*DIMENS/12.7+(I-1)*DIMENS/12.7,0)
        CALL GVECT(ORX+DIMENS,ORY+0.35*DIMENS/12.7+(I-1)*DIMENS/12.7,1)
50    CONTINUE
C
C  Plot title
C
      CALL RTXFON('CENB',0)
      CALL RTXCOL(0,0)
      CALL RTXHEI(SY*3.)
      CALL RTXJUS(2,0)
      CALL  RTX(-1,TITLE,92*SX,7*SY)
      CALL RTXCOL(0,0)
      CALL RTXHEI(SY*1.5)
      CALL  RTX(-2,SUBTITLE,52*SX,11*SY)
C
C  Plot colour legend
```

```
C
      CALL RTXCOL(0,0)
      CALL GSCAMM
      CALL RTXFON('SWIM',1)
      CALL  GCLOPT(NCHAR,LABELS,SY*1.5,2,0.0,1)
      CALL  GCOSCL(80*SX,10*SY)
      CALL GCLOSE
C
      STOP
      END
```